CENTRO DE INVESTIGACIONES EN ÓPTICA, A.C.

BIOLOGICAL APPLICATION OF CERAMIC AND METALLIC NANOPARTICLES BY EXCITATION IN THE NEAR INFRA-RED

THESIS SUBMITTED AS PARTIAL FULFILLMENT OF THE REQUIREMENTS FOR THE DEGREE OF DOCTOR IN SCIENCE (OPTICS) AT CENTRO DE INVESTIGACIONES EN ÓPTICA

By:

M. en C. Andrea Ceja Fernández

Advisor:

Dr. Elder De la Rosa Cruz

June 28th, 2016

León, Guanajuato, México

Materials by themselves do nothing; yet without materials man can do nothing. Nature itself is a self-ordered structure which developed through time by the utilization of the same properties of atomic hierarchy that man presides over in his simple constructions.

Materials and Man's Needs: Materials Science and Engineering; Summary Report, 1974

Preface

The use of materials is huge and diverse. The relationship between man and materials has been occurring since the beginning of humanity, such it is so the materials themselves gave their name to the different ages of civilization. For this reason there is a need to understand the materials, resulting also in the development of current technology.

Nanoscience and nanotecnology is a very recent research field, formally taking place since 80´s. Actually, all related to "nano" including nanotechnology, nanomaterials, nanoparticles and nanostructures have now become common words not only in research publications but also in daily life. Nanostructured materials are widely used in different applications in electronic and medicine fields. In specific as biosensors, optical filters, low-threshold laser, controlled drug delivery and imaging.

As well as has been studying, the optical properties of nanostructures are greater than micro- and macrostructures, and this is due to the size, at first because is comparable to Broglie wavelength and then because increases the number of atoms on the surface in relation to the total number of atoms in the crystal, which is that surface/volume ratio increases resulting in a rise in dispersion in crystal systems. Optical phenomena occurring in (nano) materials involve interactions between electromagnetic radiation and atoms, ions and/or electrons. Such as the case of up-conversion emission (UPC) or two-photon imaging (TPI), which permit non-invasive imaging of subcellular components with the ability to penetrate tissues hundreds of microns. Moreover morphological and fluorescence quantification from TPI of endogenous fluorophores could be helpful to compare cancerous and precancerous from normal tissue. Besides TPI has the capability to supervise a variety of biomolecular markers that are strongly indicative of cancer. By the use of this technique there is an extensive research of the use of traditional fluorophores as well as new different luminescent contrast agents such as quantum dots and metallic nanoparticles.

As part of the study of electronic interactions, the surface plasmon resonance takes place as an indispensable tool for the extensive comprehension of nanoparticles optical properties due to it gives information related of size and shape. When size and shape change the interaction between surface and electric field changes, red-shift was produced from the deviations from spherical geometry. For non-spherical particles, the resonance wavelength depends on the orientation of the electric field relative to the particle. The optical properties

of non-spherical particles are highly affected due to size variations of anisotropic shapes and this is because the quite differences in frequencies associated with the various resonance modes.

Besides, surface plasmons are especially useful to chemicals because their oscillating electric field amplifies much some optical phenomena such as Raman scattering. Actually, there are so many studies of different nanomaterials that increment raman signals (SERS technique) to detect molecules at low concentrations, it has been used to detect low concentration of biological samples of some diseases such cancer, Alzheimer (b-amyloid peptide) and Parkinson (dopamine depletion). In the study of SERS processes, it is generally accepted that electromagnetic enhancement and chemical enhancement mechanisms are the principal phenomena involved in the amplification of Raman signals, the success of SERS is highly dependent on the interaction between adsorbed molecules and the surface of plasmonic nanostructures. However, the need to have specific devices, dry substrates or determined nanoparticle arrengements involves time and money, that is why less-expensive and fast methods are in continuous research and development. On the other hand, for biomedical applications, imaging is favored by the nanoparticles scattering and/or the upconverted luminescence of nanocrystals.

In this way, in this thesis is reported the use of conjugated ZrO_2:Yb^{3+}-Er^{3+} nano-powder as cellular biomarker having obtained important results in HeLa-Cells. Resulting in a promisory conjugation protocol for biolabeling that could be an alternative to afford stable colloidal dispersions of nanoparticles in water and efficiently label cancer cells. Moreover gold nanoparticles for imaging of cervical tissue, nowadays one of the principal techniques of analyze cervical tissue damages is by determine modifications in cell structures, observing the growing of nucleus and the distribution in the epithelial membranes. It can also find cervical cancer early, in its most curable stage. By marked cervical tissue with gold nanoparticles we have obtained promising results in two-photon imaging, photothermal ablation and SERS signals of the biological samples in the NIR regions. This is important because in these regions several advantages are present such as avoiding tissues autofluorescence, better contrast, penetrations to several microns and low tissue damages. Finally it is reported the application of gold nanostructures to detect low concentrations of Rhodamine B as starting point for the study at low concentrations because to its distinct Raman features and adsorbability onto nanoparticles and α-glucose in water, which is very important due to the difficulties in glucose detection due to its low Raman scattering cross section, the mesurements of glucose has been interesting as proper monitoring of diabetes mellitus requires effective screening of glucose levels within human blood, besides the samples were measured in liquid which improve the time of results acquisitions. Taking into consideration the following objectives:

General Objective:

Implement a method to obtain metallic and ceramic nanoparticles with controlled size and shape that are highly stable and reproducible, to control their optical properties as well as their interaction with biological samples, as well as the detection of specific analytes at low concentrations in near infrared regions.

- Synthetize doped-zirconia nanocrystals and establish a preliminary protocol to functionalize them by adding cancer biomarkers.
- Establish a preliminary marking protocol to internalize doped-zirconia nanoparticles into HeLa cells.
- Synthetize gold nanoparticles with controlled size and shape.
- Establish a preliminary protocol of tissue staining witn gold nanoparticles and its characterization by Confocal Microscopy and Raman Spectroscopy.
- Depositing and controlling a silica layer on the gold nanoparticles to control the interaction between them.
- Study the effect of gold nanoparticles shape and size in optical properties, LSPR and SERS response for detection of different molecules at low concentrations.

So is that, this work will be divided in an introductory chapter, four chapters to describe the research and results obtained in this project, and the last one for general conclusions and they were presented as follows:

Chapter 1. In this chapter are discussed general concepts of nanomaterials and their bioapplications in addition to the different methods of synthesis and optical and morphological characterization. Besides, the standard method to analyze human tissues will be explained. These concepts are important to the complete understanding of the following chapters.

Chapter 2. Here it will be described the use of doped-zirconium nanocrystals (non- and functionalized) for the internalization in cervical tissue and HeLa cells, besides their confocal characterization. The internalization of the conjugated nanoparticles in HeLa cells was followed by looking at their strong red luminescence using two-photon confocal microscopy. The results show the successful uptake of conjugated ZrO2:Yb3+-Er3+ nanoparticles in HeLa cells giving a promising method for labeling different types of cancer cells for biosensing and bioimaging purposes.

Chapter 3. In this chapter will be described the use of gold nanoparticles as markers for biological samples such as HeLa cells and cervical tissue, this is due to gold nanoparticles

are biocompatible and could present a large two-photon action cross-section that is why these optical properties make gold nanoparticles an attractive contrast agent for biomedical imaging of highly scattered tissue. The use of gold nanoparticles can expand the capabilities of TPI to allow noninvasive imaging of a variety of new molecular signatures.

Chapter 4. In this chapter is shown the synthesis and characterization of Multi-branched gold nanostructures un-covered and covered with a silica shell (MBGNs and MBGNs-silica, respectively) as well as their use as SERS substrates for low-concentration detection of Rhodamine B and α-Glucose. In this thesis were analyzed MBGNs and MBGNs-silica coating to enhance the Raman signal, in this case with the presence of silica coating it is promoted the aggregation and a stronger interaction with RB and α-glucose improving the SERS signal. The successful detection within a clinically relevant concentration range shows the promise of the MBGNs and MBGNs-silica as potential SERS substrates for detecting molecules that strongly interact with silica coating or MBGN surface itself.

Chapter 5 General Conclusions

NOTE: This thesis includes material from three published papers by the author. Chapters 2 and 4 use materials from the articles: Tzarara López-Luke, Jorge Oliva, Juan Vivero-Escoto, Ana Lilia Gonzalez-Yebra, Ruben A. Rodriguez Rojas, Andrea Martínez-Pérez, and Elder De la Rosa [1]. And coauthored with Tzarara López-Luke, Alejandro Torres-Castro, Damon. A. Wheeler, Jin Z. Zhang and Elder De la Rosa [2].

References

1. Ceja-Fdez, A., et al., *Labeling of HeLa cells using ZrO2:Yb3+-Er3+ nanoparticles with upconversion emission.* Journal of Biomedical Optics, 2015. **20**(4): p. 046006-046006.
2. Ceja-Fdez, A., et al., *Glucose detection using SERS with multi-branched gold nanostructures in aqueous medium.* RSC Advances, 2014. **4**(103): p. 59233-59241.

Resumen

En el presente trabajo se sintetizaron nanoparticulas de óxido de zirconio dopadas con yterbio y erbio (2% y 1%, respectivamente) y oro, las cuales presentan propiedades ópticas interesantes para el uso en bio-aplicaciones, como es el caso de *conversión hacia arriba* (*ing.* up-conversion) y luminiscencia por absorción de dos fotones, en las cuales la excitación se da en el cercano infrarrojo. Para el marcaje de células HeLa, las nanoparticulas de ZrO_2:Yb^{3+},Er^{3+} se conjugaron con biotina y anti-Ki67, para posteriormente incubarse en estas células habiendo obtenido resultados prometedores debido a la fuerte emisión roja de estas nanoparticulas además que no se había hecho el marcado de células con éste tipo de material. Por otra parte las nanopartículas de oro, sintetizadas por el método Türkevich, fueron usadas como marcadores del tejido de Cérvix resultando ser una buena opción de marcaje debido su capacidad de presentar luminiscencia de dos fotones resultando en una buena opción para imagen de muestras biológicas, además que se hizo el análisis de los tejidos por espectroscopía raman siendo realzada la señal de estos, pudiendo observar resultados preliminares para el estudio de diferencias entre tejido sano y con presencia de carcinoma. A partir de estas partículas esféricas usándolas como semillas se obtuvieron nanoestructuras multi-picos de oro, sin necesidad de usar surfactante a la cuales posteriormente se les colocó un capa de sílica para mejorar su estabilidad, posteriormente cuando se tuvo controlada la síntesis de estas nanoestructuras, se hicieron pruebas para determinar su efectividad en espectroscopia Raman como substratos para obtener señales realzadas (SERS), para lo cual se pudieron obtener importantes resultados ya que se detectó de Rodamina B y α-Glucosa en líquido a concentraciones de 50 pM y 5 mM (90 mg dL-1) respectivamente excitando con un láser de 785 nm.

Summary

In this thesis, nanoparticle of zirconium oxide doped with ytterbium and erbium (2% and 1%, respectively) and gold, which have interesting optical properties for use in bio-applications, such as up-conversion and luminescence by two-photon absorption, in which excitation occurs in the near infrared. For labeling of HeLa cells, the nanoparticles of ZrO_2: Yb^{3+}, Er^{3+} were conjugated with biotin and anti-Ki67, later incubated in these cells having obtained promising results due to the strong red emission of these nanoparticles in addition that had not made the marking cells with this type of material. Moreover gold nanoparticles, synthesized by the Turkevich method, were used as markers of Cervical tissue out to be a good option for marking due to its ability to present luminescence two-photon resulting in a good choice to image biological samples, as well that the analysis of the tissues was being enhanced raman spectroscopy signal, being able to observe preliminary results for the study of differences between healthy and carcinoma tissue. From these spherical particles by using them as seeds, multi-branched gold nanostructures (MBGNs) were obtained, with non-surfactant to which subsequently were pladded a silica-coating to improve stability, later when had controlled synthesis of nanostructures, MBGNs were proven to determine its effectiveness in Raman spectroscopy as substrates for enhanced signals (SERS), for which we could obtain significant results since it was detected Rhodamine B and α-glucose in liquid at concentrations of 50 pM and 5 mM (90 mg dL-1) respectively with a laser exciting 785 nm.

Aknowledgements

I would like to express my gratitude to CONACYT for gave me the opportunity of doing my PhD by providing a scholarship (support No. 321938). I want to thank immensely to my advisor Dr. Elder De la Rosa Cruz for his constant guidance during the course of this research. I would like to recognize the important contributions from my committee members and thesis reviewers, Dr. Luis Armando Díaz and Dr. Claudio Frausto, Dr. Ramon Carriles, Dr. Pedro Salas and finally to Dr. Tzarara López, as they have been essential part in my formation. I want to thank those who collaborated during research, as was Dr Alejandro Torres, Dr. Juan Vivero, Dr. Ana Lilia Gonzalez, Martín Olmos, Nydia Hernandez, Christian Albor, Octavio Pompa and Carlos Juarez. Obviously I will not forget my coworkers, Omar, Isaac, Jorge, Leonardo, Diego, Elisa, Ale, Andrea Martinez, Dr. Haggeo Desirena, Dr. Alex Martinez and Dr. Lorena Benjume. It was really fun working with all of them.

I would like to thank my parents, sisters Ale and Annel, and my brother Ladis, for being a very important part of my formation. To all of my family members for giving me every day the thrust needed to walk on this path. Special thankfulness to my family-in-law for being always beside us. Thanks to all the people that I met during my PhD process. Last but not least, I am forever indebted with my husband, Luis Adan, for his love and constant support during this process.

Table of Contents

List of figures

CHAPTER 1

NANOSTRUCTURED MATERIALS

1.1 Nanomaterials

As has been widely studied, the use of nanomaterials (accidentaly or not) has been taking place in some historical stages, like The Lycurgus Cup (4^{th} Century, Roman period) in this example of dichroic glass, modern analytic methods have discovered that colloidal gold and silver particles (~70nm) in the glass allow it to look opaque green when lit from outside but translucent red when light shines from the inside [1, 2]. Later, glowing, glittering "luster" ceramic glazes used in the Islamic world (9^{th}-17^{th} Centuries) and subsequently in Europe, contained silver or copper or other metallic nanoparticles [3]. Another example is the "Damascus" saber blades (13^{th}-18^{th} Centuries), that contained carbon nanotubes and cementite nanowires resulting in an ultrahigh-carbon steel formulation that conferred them strength, resilience, the ability to hold a keen edge, and a visible moiré pattern in the steel that give the blades their name, this was corroborated by High-resolution transmission electron microscopy where some images of carbon nanotubes were obtained after dissolution in hydrochloric acid, showing remnants of cementite nanowires encapsulated by carbon nanotubes [4].

In 1959 Richard Feynman of the California Institute of Technology gave what is considered to be the first lecture on technology and engineering at the atomic scale [5], "There's Plenty of Room at the Bottom" at an American Physical Society meeting at Caltech. In that lecture Feynman explored, apparently simple, possibilities of working at the atomic scale which would have amazing results. He mentioned ideas such as writing at small scales, manipulations at atomic level, as well as designing molecules one atom at a time and the challenges involved in developing miniature machines. Although atoms were seen for the firt time in 1955, developments in electron microscopy were taking place even before Feynman's lecture. Remarkable advances have been made on the nanoscale, such as developments in lithography, the discovery of fullerenes and improvements in microscopy that have made it possible to see, name and move atoms at will [6].

The concept of 'nano' refers to $1x10^{-9}$ m, that is to say one billionth of a meter. Having said that, a Nanoparticle is defined as an atomic arrangement with a size range of 1-100 nm [7]; however, there are some particles bigger than 100 nm that show similar behavior as ones of nanometric scales, these nanoparticles demonstrate unusual catalytic, optical and electronic properties in contrast to bulk materials. This is due to the surface/volume ratio resulting in an increase in their interface interacting atoms. These properties vary with the manufacturing technique used for

controlling their size and shape, thus making them interesting building blocks for nanoscale structures, assemblies and devices.

Their optical properties are closely related to the electrical and electronic properties of the material; however, other factors are also involved when dealing with optical properties. For nanometric scale, particles are confined in dimensions that are smaller than the wavelength of light therefore the physics of these systems cannot be explained by classical theories but requires quantum mechanics. That is why the study of these properties is important.

At this time there are many types of nanoparticles, such as those that have different shapes as nanospheres, nanorods, nanocrystals, nanolayers, nanostars, nanocubes, quantum dots, nanofibers, nanoporous, nanobars, and others. Moreover, nanoparticles have potential in different applications as well as end products, like sensors, pharmaceutical drugs and quantum dots, or as part in end products, like carbon black in rubber products. The physical and chemical properties of nanomaterials facilitate interface electronic signal transduction with biological recognition events and to design advanced and innovative bioelectronic devices.

In this work we will present the synthesis and applications of gold and doped zirconium oxide as biomarkers in biological samples, this interest born from the optical properties of these materials, firstly gold nanoparticles have interesting properties like the possibility of changing the surface plasmon resonance (SPR) from visible to near infrared regions and this is caused by varying their size and shape with is useful for medical application, another important property is to present two photon luminescence which is useful for imaging due to the advantages like high cross section and contrast, low damping and biocompatibility, another use of gold nanostructures is the capability of serve as Raman enhancers presenting SERS activity for detection al low concentration of several analytes for different types of diseases, the importance of find better contrast agents for determine disease levels or changes in their molecular composition is crucial for early detections, also the necessity of have faster detection techniques is essential for disease treatments. On the other hand we have interesting properties with ZrO_2:Yb^{3+}-Er^{3+} nanoparticles because their ability to convert low-energy near-infrared (NIR) radiation into higher-energy visible luminescence through a process named upconversion (UPC) and its potential benefits for the use of nanocrystals with UPC emission in biological applications such as no damage of tissues and improving contrast in

biological specimens due to the absence of autofluorescence upon excitation with IR light, that is why this material has potential applications in imaging.

The characterization techniques are crucial to know the specific properties that we were looking for; at the beginning it was necessary to have structural and optical characterization, we used Transmission Electron Microscopy (TEM) and Scanning Electron Microscopy (SEM) for determine the size and shape of our material; for determine the light absorbance level of gold nanoparticles UV-Vis Spectroscopy were used, and for analyze the characteristic spectra of the corresponding functional groups or bindings we use Raman Spectroscopy, for the case of doped zirconium oxide we analyze its crystalline structure by X-Ray Diffraction and during the functionalization the samples were analyzed by Infra-Red (FTIR) to evaluate the presence of different functional groups; to determine the superficial charges it was necessary to use Zeta Potential and the average sizes by Dynamic Light Scattering which gives us a general idea of how the material is incrementing their size by adding specific molecules during the functionalization. The optical characterization involves Confocal Microscopy to analyze the interaction of gold and doped zirconium oxide with biological samples, Two Photon Imaging of gold in cervical tissue as cell structure biomarker and the Photoluminescence of doped zirconium oxide to evaluate the UPC properties of the material.

1.1.1 Bioapplications

Nanomaterials have unique capabilities for a variety of biomedical applications ranging from diagnosis of diseases to novel therapies. In particular, nanotechnology may greatly expand the impact of biophotonics, particularly optical imaging and biosensing, by providing more robust contrast agents, fluorescent probes, and sensing substrates [8].

One of the most important aspects in biomedical applications is the fact that nanoparticle size range are comparable to common biomolecules, which provides the opportunity to have intracellular labeling or antibody targeting. Moreover, nanostructures may be modified to have better integration with biological systems, as well as modify their surface by different coatings to encourage aqueous solubility, biocompatibility, or biorecognition. Nanostructures can also be embedded within other biocompatible materials to provide nanocomposites with unique properties [9].

These versatile behaviors are highly dependent on the physical and chemical properties of nanoparticles such as morphology, size, surface charge, surface modifications, and chemical composition. Generally, nanostructures have optical properties much higher to the molecular species they replace such as higher quantum efficiencies, greater scattering or absorbance cross sections, optical activity over more biocompatible wavelength regimes, and considerably greater chemical stability or stability against photobleaching. Furthermore, some nanostructures provide optical properties that are highly dependent on particle size or dimension. The capacity to systematically change the optical properties through structure modification not only enhances the traditional uses, but can also lead to applications beyond the reach of conventional molecular bioconjugates [9].

The first use of gold nanoparticles takes place in 1971 when the immunogold staining method was invented by Faulk and Taylor; they absorbed anti-salmonella rabbit gamma globulins to gold particles for one step identification and localization of salmonella antigens [10]. Although indirect labelling techniques with gold probes were introduced by Romano et. al. in 1974 [11]; They reported the protein A labeling to detect primary immunoglobulin. Since that time, the labeling of targeting molecules, such as antibodies, with gold nanoparticles has revolutionized the visualization of cellular components by electron microscopy [12]. Such was the case of Roth et. al. in which thin sections of biological samples were analyzed by electron microscopy [13]. Since then, the use of colloidal gold in transmission electron microscopy has grown at an enormous rate and this is due to the high electron density of gold nanoparticles coupled with the ease of use of different particle sizes for examination at various magnifications. The optical and electron beam contrast properties of gold colloid have provided excellent detection capabilities for applications, including immunoblotting, flow cytometry, and hybridization assays. Furthermore, conjugation protocols to attach proteins to gold nanoparticles are robust and simple [14].

On the other hand, among the diverse *in vitro* biodetection methods, luminescent bioassay is at present an important analytical tool because of its convenient optical signal transduction, high sensitivity and fast response [15-18]. As is widely known, when an appropriate wavelength is used, penetration depth may be substantial and light can reach regions of complex molecular edifices which are not accessible to other molecular probes. In addition, the emitted photons are easily detected by highly sensitive devices and techniques, including single-photon detection.

Some of the barriers to overcome are photobleaching because the time-resolved detection needs to be larger than 107-109 s^{-1}, corresponding to excited state lifetimes between 100 and 1 ns. There are some semiconductor materials that have been used as luminescent materials, such as the case of quantum dots, despite they are used due to their high luminescence, their tunability in the entire visible range and good photostability, they have high toxicity, making them of little help for *in vivo* applications [19]. There exist other alternatives such as trivalent lanthanide ions, LnIII, that present singular properties, allowing easy spectral and time discrimination of their emission bands which span both the visible and near infrared (NIR) ranges. At the beginning, biological cells were stained with lanthanides (europium thenoyltrifluoroacetonate) observing bright red spots under mercury lamp illumination [20]; however the experiment takes long time.

Nowadays, there are many semiconductors, as well as research and development of different doped-crystals for biomedical applications, such as the case of ZrO_2 which is widely known due to its hardness and important optical properties like high refractive index, photochemical stability and low phonon energy that improve the probabilities of radiative transitions [21-23]. This material can be modified to obtain different size, shape and crystalline phases [24-27] beside it has been used as support matrix of different lantanides presenting important luminescent properties [28-30]. These developments like the optimization of bioconjugation methods or time-resolved luminescence microscopy resulted in applications in many fields of biology and medicine as in the case of tissue [31, 32] and cell imaging [33, 34] or analyte sensing [35] and drug delivery [36].

1.2 Nanomaterial's synthesis

As we see, nanomaterials involve structures that have at least one dimension in nanometric scale, such as nanoparticles, nanorods, nanowires, thin films or also bulk materials made of nanostructures. Actually there are many technologies to produce nanostructures or nanomaterials, and these techniques are grouped in various ways. One form is to classify them according to the growth media such as vapor phase growth, liquid phase growth, solid phase formation or hybrid growth. On the other hand the techniques can be classified according to the form of products, like nanoparticles (colloidal processing, flame combustion or phase segregation), nanorods or nanowires (template-based electroplating, solution- liquid-solid growth or spontaneous anisotropic growth), thin films (molecular beam epitaxy or atomic layed deposition) and finally nanostructured bulk materials (photonic band-gap crystals by self-assembly of nanoparticles) [37].

In this work, gold nanoparticles were synthetized by chemical processes in which gold nanoparticles were obtained by growing the reduced gold in a liquid medium composed of various reactants. Doped-Zirconia was obtained by a precipitation process and a hydrothermal process. Both methods are low-cost, do not need special or complex devices, all involved parameters are easily controllable and easily reproducible.

1.2.1 Reduction Synthesis

There are different ways of reduction synthesis, resulting in different characteristics of the final product. Not only the strength of the reductant is important, so is the presence of a stabilizer. Different authors have proposed various methods to reduce gold as in the case of the single phase water based reduction of a gold or silver salt by citrate, introduced by Turkevich et al. [38, 39] and the refined by Frens [40] producing almost spherical particles with varying sizes; the method of Brust et al. [41] where gold nanoparticles are produced in organic liquids that are normally not miscible with water (like toluene) involves the reaction of a chlorauric acid solution with tetraoctylammonium bromide (TOAB) solution in toluene and sodium borohydride as an anti-coagulant and a reducing agent, respectively; the Martin Method [42] where gold nanoparticles are generated in water by reducing $HAuCl_4$ with $NaBH_4$, gold nanoparticles are stablilized by using an stabilizer such as citrate, or with HCl and NaOH for long term storage or only for few hours respectively; however one must be careful with the ratios of $NaBH_4$/HCl ions and $NaBH_4$/NaOH ions.

Turkevich method is generally used to produce modestly monodisperse colloidal gold nanospheres of around 10–20 nm in diameter. It involves the reaction of small amounts of boiling chlorauric acid with small amounts of sodium citrate solution. The colloidal gold will form because the citrate ions act as both a reducing agent, and a capping agent. This method was chemically studied by Chow and Zukoski [43] in where the formation of gold colloids produced by the citrate reduction of chloroauric acid is explored as a function of temperature and reagent concentration. As gold ions are reduced, the reaction medium changes from black to purple to blue before turning deep red. These color changes are shown to result from a decrease in particle size over the course of the reaction. Increases in particle surface potential over the course of the reaction are shown to result from competitive adsorption of citrate and gold ions.

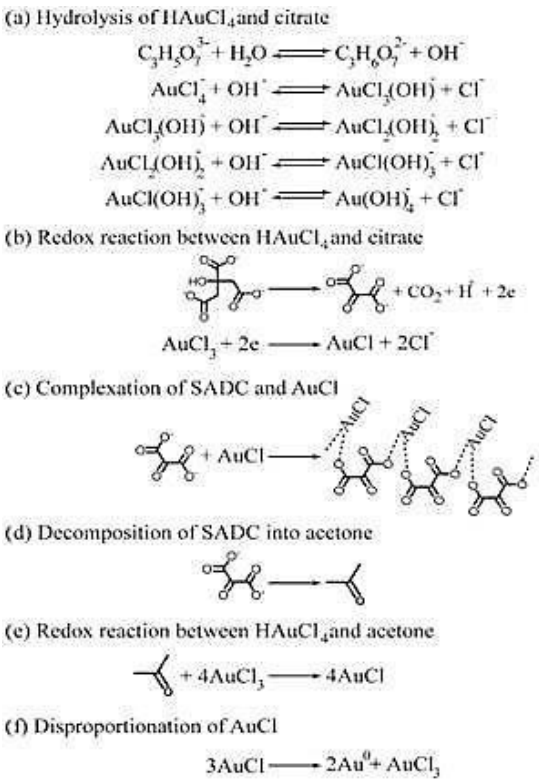

Figure 1.1 Reactions involved during the citrate reduction of chloroauric acid for nucleation and crystal growth of gold nanoparticles. (taken from chem553project)

1.2.2 Seed Mediated Method

A seed-mediated method is that where the nanoparticle synthesis is conducted through successive nucleation and growth steps and also has direct consequence on the basic mechanism being extremely sensitive to physical and chemical parameters [40, 44-53]. In some of the solution-phase metal nanoparticle synthesis procedures, the control of nucleation and growth steps are done by changing the reducing agent or stabilizer concentration so the size and shape can be easily controlled [40, 50, 51, 54-57]. For solution-phase gold nanoparticle synthesis, it has been observed an initial slow nucleation followed by a nucleation surge associated with autocatalytic surface growth [58].

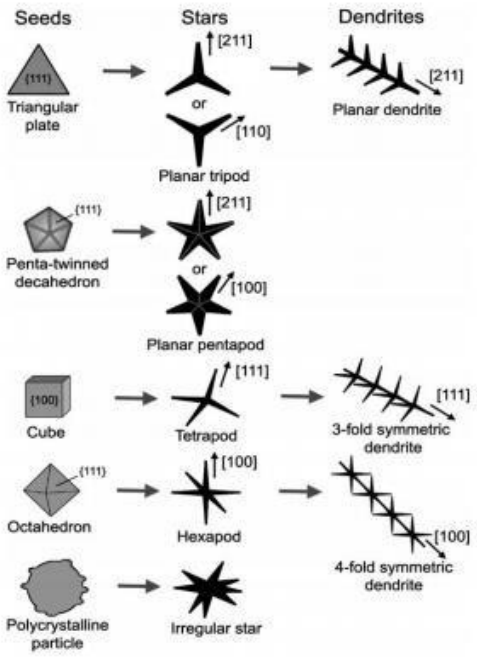

Figure 1.2 Schematic illustration of the possible evolution from fcc metal seeds to stars and dendrites under kinetically controlled synthesis (taken from Junyan Xiao and Limin Qi [59]).

1.2.3 Hidrotermal Synthesis

Hydrothermal synthesis offers many advantages over conventional and non-conventional ceramic synthetic methods. All forms of ceramics can be prepared with hydrothermal synthesis, namely powders, fibers, single crystals, monolithic ceramic bodies, and coatings on metals, polymers, and ceramics.

Hydrothermal process involves H_2O both as a catalyst and occasionally as a component of solid phases in the synthesis at elevated temperature (> 100°C) and pressure (> a few atmospheres) to crystallize ceramic materials directly from solution. However, researchers also use this term to describe processes conducted at ambient conditions. Syntheses are usually conducted at autogeneous pressure, which corresponds to the saturated vapor pressure of the solution at the specified temperature and composition of the hydrothermal solution [60].

1.2.4 Conjugation and functionalization

Bioconjugates are involved in many biomedical applications. The idea of merging biological and nonbiological systems at the nanoscale has been investigated for many years. The implicated

bioconjugation chemistry in based on combining the functionalities of biomolecules and nonbiological ones to obtain molecular species that could be applied as markers in cellular and molecular biology, biosensing and imaging [14]. Specific binding of nanoparticles to cell surfaces, cellular uptake, and nuclear localization have all been demonstrated following conjugation of semiconductor nanocrystals to appropriate targeting proteins, such as transferrin or antibodies [61-66].

For the case of gold nanoparticles there are different ways to bioconjugate them, depending on targeting type, some instances are, for example Xianfeng Zhou and coworkers conjugated low molecular weight chitosan (Chito6) to gold nanoparticles (GNPs), which formed physically stable complexes with DNA and transfected cells more effective than high molecular weight chitosan (Chito102) in vitro [67], or the case of Yokota, S et al. that presented the first preparation of gold nanoparticles that used an ideal solvent for structural carbohydrates such as cellulose, namely hot 80% N-methylmorpholine-N-oxide (NMMO)/H_2O, and the in situ conjugation of the gold nanoparticles with thiolabeled cellulose through spontaneous chemisorption [68]. Kumar et al. showed that the incubation of the plant fungus pathogenic Helminthosporum Solani with an aqueous solution of chloroaurate ions, produces a diverse mixture of extracellular gold nanocrystals with different sizes and shapes. Then the nanoparticles were conjugated to the anti-cancer drug doxorubicin (Dox) and taken up readily into HEK293 cells [69]. Maus and coworkers demonstrated that conjugation of the conantokin G peptide to the solvent exposed interface of the passivation layers results in maximal binding interaction between the peptide functionalized AuNPs and the targeted N methyl D-aspartate receptors on the cell surface Conantokin G coupled AuNP may be used to spatially restrict N methyl D-aspartate receptor blockade on neuronal surfaces [70].

On the other hand the addition of PEG into gold nanoparticles is one of the most effective ways to reduce their cytotoxicity, because it is necessary to avoid nanoparticle recognition by the reticuloendothelial system due to the capitation of nanoparticles in organs such as the liver and spleen, clearing them from circulation and dramatically decreasing target-site delivery of the drug [71, 72]. So is that important as it refers to conjugation.

1.3 Optical and morphological Characterization

It is increasingly recognized that nanomaterials present a range of characterization challenges that have the potential to inhibit or delay the scientific and technological impact of nanoscience and nanotechnology. The behavior of NPs is critically dependent on several particle characteristics, including size, surface area, surface reactivity, electronic properties, chemical composition and reactivity.

1.3.1 UV-Vis Spectroscopy

Electromagnetic radiation can be considered as a combination of coupled alternating electric and magnetic fields that travel through space. When radiation interacts with matter, a number of processes can occur, including reflection, scattering, absorption, fluorescence/phosphorescence (absorption and reemission), and photochemical reaction (absorbance and bond breaking) among others. In general, when measuring UV-visible absorption spectra, we want only absorbance to occur. Because light is a form of energy, absorption of light by matter causes the energy content of the molecules (or atoms) to increase.

Surface plasmons are surface electromagnetic waves that propagate in a parallel direction to the interface between a metal and dielectric or vacuum. Since the wave is on the boundary of the metal and the external medium (air or water for example), these oscillations are very sensitive to any change of this boundary, such as the adsorption of molecules to the metal surface.

Surface plasmon resonance is a spectroscopic characteristic of noble metal nanoparticles, which gives rise to a sharp and intense absorption band in the visible range. The physical origin of the absorption is a collective resonant oscillation of the free electrons of the conduction band of the metal. For a spherical nanoparticle that is much smaller than the wavelength of the incident light, its response to the oscillating electric field can be described by the approximation of Mie theory.

1.3.2 Scanning and Transmission Electron Microscopy

Nowadays Electron Microscopy is widely used for material characterization; this is because it allows resolving nanometric scale features. These equipments provide insight into the morphological nature of the materials, but also information about surface chemical composition.

Scanning Electron Microscopy (SEM) consists in accelerated electrons carrying significant amounts of kinetic energy, and this energy is dissipated as different signals produced by electron-sample interactions when the incident electrons are decelerated in the solid sample. The obtained signals are secondary electrons (for SEM images), backscattered electrons, diffracted backscattered electrons (used to determine crystal structure and orientation), photons (characteristic X-rays used for elemental analysis and continuum X-rays), visible light (cathodoluminescence–CL), and heat.

On the other hand, Transmision Electron Microscopy (TEM) consist in a high energy beam of electrons which passes through a very thin sample, and the interactions between the electrons and the atoms can be used to observe different characteristics such as crystal structure, dislocations and grain boundaries. Chemical analysis can also be performed. TEM can be used to study the growth of layers, their composition and defects in semiconductors. High resolution can be used to analyze the quality, shape, size and density of very small particles.

1.3.3 Zeta Potential and Dynamic Light Scattering (DLS)

To know how is the nanoparticle behavior, as in the case of surface charges for electroctathic interactions with biological samples, techniques as Zeta Potential could be helpful. The development of a net charge at the particle surface, which is attributed of the superficial functional groups, affects the distribution of ions in the surrounding interfacial region, resulting in an increased concentration of opposite charge ions close to the surface. The magnitude of the zeta potential or the electro-kinetic potential between two superficial layers of the colloidal particles, gives an indication of the potential stability of colloidal systems. A colloidal system is when one of the three states of matter: gas, liquid and solid, are finely dispersed in another one.

When all the particles in suspension have a large negative or positive zeta potential then they will tend to repel each other and there is no tendency to aggregation. However, if the particles have low zeta potential values then there is no force to prevent the particles coming from together and flocculating. The general dividing line between stable and unstable suspensions is generally taken at either +30mV or -30mV. Particles with zeta potentials more positive than +30mV or more negative than -30mV are normally considered stable.

Another technique for continuous analyses of colloidal samples Dynamic Light Scattering (DLS) is a technique where the size of particles, typically in the sub-micron region, is measured, this technique gives us a fast general idea of the nanoparticles behavior during a functionalization process; it is also referred to as Photon Correlation Spectroscopy or Quasi-Elastic Light Scattering. It is based on the Brownian motion experienced by particles suspended in a liquid. Larger nanoparticles show slow Brownian motion. DLS monitors the Brownian motion by light scattering; the speed at which the particles are diffusing is measured by recording the rate at which the intensity of the scattered light fluctuates.

1.4 Raman Spectroscopy

Raman spectroscopy is a technique where we can have information about vibrational, rotational and other low frequency transitions in molecules and use it for sample identification and quantification. It uses a laser beam on a sample and detecting scattering light. With this different responses are obtained: a) Rayleigh or elastic scattering, which is the majority of the scattered light and is at the same frequency as the excitation source and b) Inelastic scattering that is when the frequency of photons in monochromatic light changes upon interaction with a sample. Photons of the laser light are absorbed by the sample and then reemitted. The frequency of the reemitted photons is shifted up or down in comparison with original monochromatic frequency, which is called the Raman Effect. Plotting the intensity of this "shifted" light versus frequency results in a Raman spectrum of the sample where the band positions will lie at frequencies that correspond to the energy levels of different functional group vibrations. Raman spectroscopy can be used to study solid, liquid and gaseous samples.

This technique is based on molecular deformations in electric field **E** caused by molecular polarizability **α**. The laser beam can be considered as an oscillating electromagnetic wave with electrical vector **E**. After interaction with the sample it induces electric dipole moment $\mathbf{P} = \alpha\mathbf{E}$ which deforms molecules and due to this periodical deformation, molecules start vibrating with characteristic frequency υ_m (Amplitude of vibration is called nuclear displacement). Monochromatic laser light with frequency υ_0 excites molecules and transforms them into oscillating dipoles emitting light of three different frequencies:

1. **Elastic Rayleigh scattering**. A molecule with no Raman-active modes absorbs a photon with the frequency υ_0. The excited molecule returns back to the same basic vibrational state and emits light with the same frequency υ_0 as the excitation source.

2. **Stokes frequency ("Stokes")**. A photon with frequency υ_0 is absorbed by a Raman-active molecule which at the time of interaction is in the basic vibrational state. Part of the photon's energy is transferred to the Raman-active mode with frequency υ_m and the resulting frequency of scattered light is reduced to $\upsilon_0 - \upsilon_m$.

3. **AntiStokes frequency ("Anti-Stokes")**. A photon with frequency υ_0 is absorbed by a Raman-active molecule, which, at the time of interaction, is already in the excited vibrational state. Excessive energy of excited Raman active mode is released, the molecule returns to the basic vibrational state and the resulting frequency of scattered light goes up to $\upsilon_0 + \upsilon_m$.

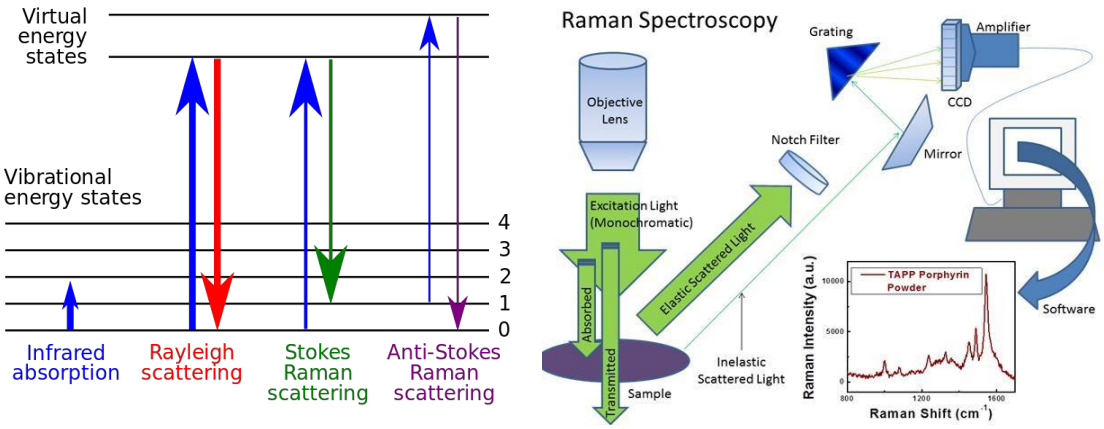

Figure 1.3 Schematic for process involved in collecting Raman spectra. (Right, Taken from Murphy et al., 2011[73])

1.4.1 SERS

Surface-Enhanced Raman Spectroscopy utilizes the Raman effect from molecules that were adsorbed on specific metal surfaces, being able to achieve magnifications stronger than Raman signal from the same molecules in bulk volume. The proposed reason for this is that since the intensity of the Raman signal is proportional to the square of electric dipole moment $\mathbf{P}=\alpha\mathbf{E}$, there are two possible reasons: the enhancement of polarizability α, and the enhancement of electrical field $\mathbf{E}$.

The first enhancement of **polarizability α** or **chemical enhancement** may occur because of a charge-transfer effect or chemical bond formation between metal surface and molecules under observation.

The second one called **electromagnetic enhancement** takes place between the interactions of the laser beam with irregularities on the metal surface. It is probable that laser light excites conduction electrons at the metal surface leading to a surface plasma resonance and strong enhancement of the electric field **E**.

For SERS there are two highlighted parameters, the first one is the molecules that are going to be detected (probe) and the second one is the metallic structure onto which they adsorb (SERS substrate), both are independent however a degree of compatibility is convenient due to there is a certainty that the probe goes onto substrate to finally profit the Raman signal amplifications. In general terms a good SERS substrate is one that provides the largest enhancement or amplification. Moreover, SERS enhancements are generated by resonant responses of the substrate so is that they are commonly wavelength dependent. At the end good enhancements are given by a limited excitation wavelength range, otherwise if the excitation is at the wrong wavelength the SERS substrate will not serve [74].

The most interesting range of excitation for SERS is in the Visible/Near-Infrared region, which is the typical range for molecular Raman scattering experiments, that is why gold and silver structures are the most used for SERS and plasmonics. These structures have the right optical properties to sustain good plasmon resonances in the Visible/Near-Infrared region.

1.5 Tissue Staining with nanoparticles

Tissue staining is an established histological technique that reveals structural patterns that are not clear or sufficiently visible to be observed directly. The first dyes used for staining of tissue structures were colored substances isolated from natural resources—e.g., indigo, saffron, hematoxylin, azocarmine, and orcein. These dyes were commonly used for dyeing textile fibers and later found wide application in histology [75].

In 1971 Faulk and Taylor used colloidal gold for bioapplications having invented the immunogold staining procedure, since then the labeling of targeting molecules with gold nanoparticles has been

an important tool for the visualization of cellular components by electron microscopy [12]. Gold nanoparticles have excellent optical and electron beam contrast properties which has led to detection capabilities for different applications such as immunoblotting, flow cytometry and hybridization assays.

1.6 Imaging

Actually, the advanced techniques of visualizing tissue structures are named as "tissue imaging" and they range from *in vivo* imaging to high resolution for complete organs or cell tracking respectively. Classical histological methods are based on specific chemical staining of tissue sections, specific proteins, peptides, lipids, metabolites or other biomolecules; however these standard techniques provided only limited information about chemical composition or structural specificity, on the other hand antibody-based techniques developed for visualization of fixed structures are generally not compatible with imaging in vivo due to protein degradation or limited penetration into tissues. Nowadays funtionalized nanoparticles are applied in bioimaging technology, due to their effectiveness to migrate to specific sites, interact with the target tissue or deposit in controlled sites [75].

1.6.1 Confocal Microscopy

Confocal microscopy is one of the most significant advances in optical microscopy because it allows visualization deep within both living and fixed cells and tissues and affords the ability to collect sharply defined optical sections from which three-dimensional renderings can be created.

This technique offers several advantages over conventional optical microscopy, including the ability to control depth of field, elimination or reduction of background information away from the focal plane, and the capability to collect serial optical sections from thick samples. The fundamental clue to the confocal approach is the use of spatial filtering techniques to eliminate out-of-focus light or glare in specimens whose thickness exceeds the immediate plane of focus. Confocal microscopy is a widely used technique, due in part to the relative ease with which high-quality images can be obtained from samples prepared for conventional microscopy, and the growing number of applications in biology such for both fixed and living cells and tissues.

1.7 References

1. Barber, D.J. and I.C. Freestone, *An Investigation Of The Origin Of The Color Of The Lycurgus Cup By Analytical Transmission Electron-Microscopy*. Archaeometry, 1990. **32**: p. 33-45.
2. Freestone, I., et al., *The Lycurgus Cup - A Roman nanotechnology.* Gold Bulletin, 2007. **40**(4): p. 270-277.
3. Pradell, T., et al., *Luster decoration of ceramics: mechanisms of metallic luster formation.* Applied Physics a-Materials Science & Processing, 2006. **83**(2): p. 203-208.
4. Reibold, M., et al., *Materials - Carbon nanotubes in an ancient Damascus sabre.* Nature, 2006. **444**(7117): p. 286-286.
5. Feynman, R., *There's Plenty of Room at the Bottom.* Engineering and Science, 1960. **23**(5): p. 22-36.
6. Yadugiri, V.T. and R. Malhotra, *'Plenty of room' - fifty years after the Feynman lecture.* Current Science, 2010. **99**(7): p. 900-907.
7. Köhler, M. and W. Fritzsche, *Nanotechnology*, ed. Wiley-VCH. 2003.
8. Jennifer L. West, Rebekah A. Drezek, and N.J. Halas, *Nanotechnology Provides New Tools For Biomedical Optics*, in *Tissue Engineering and Artificial Organs*, J.D. Bronzino, Editor. 2006. p. 25(1)-25(9).
9. West, J.L. and N.J. Halas, *Engineered nanomaterials for biophotonics applications: Improving sensing, imaging, and therapeutics.* Annual Review of Biomedical Engineering, 2003. **5**: p. 285-292.
10. Page Faulk, W. and G. Malcolm Taylor, *Communication to the editors: An immunocolloid method for the electron microscope.* Immunochemistry, 1971. **8**(11): p. 1081-1083.
11. Romano, E.L., C. Stolinski, and N.C. Hughes-Jones, *An antiglobulin reagent labelled with colloidal gold for use in electron microscopy.* Immunochemistry, 1974. **11**(8): p. 521-522.
12. Hayat, M.A., *Colloidal Gold : Principles, Methods, and Applications*. Vol. 1. 1989: Academic Press, Inc. 536.
13. Roth, J., M. Bendayan, and L. Orci, *FITC-PROTEIN-A-GOLD COMPLEX FOR LIGHT AND ELECTRON-MICROSCOPIC IMMUNOCYTOCHEMISTRY.* Journal of Histochemistry & Cytochemistry, 1980. **28**(1): p. 55-57.
14. Hermanson, G.T., *Bioconjugate Techniques, 3rd Edition*. Bioconjugate Techniques, 3rd Edition. 2013, Amsterdam: Elsevier Science Bv. 1-1146.
15. Borisov, S.M. and O.S. Wolfbeis, *Optical biosensors.* Chemical Reviews, 2008. **108**(2): p. 423-461.
16. Buenzli, J.-C.G., *Lanthanide Luminescence for Biomedical Analyses and Imaging.* Chemical Reviews, 2010. **110**(5): p. 2729-2755.
17. Seydack, M., *Nanoparticle labels in immunosensing using optical detection methods.* Biosensors & Bioelectronics, 2005. **20**(12): p. 2454-2469.
18. Yuan, J.L. and G.L. Wang, *Lanthanide-based luminescence probes and time-resolved luminescence bioassays.* Trac-Trends in Analytical Chemistry, 2006. **25**(5): p. 490-500.
19. Xing, Y. and J. Rao, *Quantum dot bioconjugates for in vitro diagnostics & in vivo imaging.* Cancer Biomarkers, 2008. **4**(6): p. 307-319.
20. Scaff, W.L., D.L. Dyer, and K. Mori, *Fluorescent Europium Chelate Stain.* Journal of Bacteriology, 1969. **98**(1): p. 246-248.
21. Ghosh, P., K.R. Priolkar, and A. Patra, *Understanding the local structures of Eu and Zr in Eu2O3 doped and coated ZrO2 nanocrystals by EXAFS study.* Journal of Physical Chemistry C, 2007. **111**(2): p. 571-578.
22. Lopez-Luke, T., et al., *Solvent and surfactant effect on the self-assembly and luminescence properties of ZrO2:Eu3+ nanoparticles.* Applied Physics B-Lasers and Optics, 2011. **102**(3): p. 641-649.

23. Ye, Z., et al., *Preparation, Characterization and Application of Fluorescent Terbium Complex-Doped Zirconia Nanoparticles.* Journal of Fluorescence, 2005. **15**(4): p. 499-505.
24. French, R.H., et al., *EXPERIMENTAL AND THEORETICAL DETERMINATION OF THE ELECTRONIC-STRUCTURE AND OPTICAL-PROPERTIES OF 3 PHASES OF ZRO2.* Physical Review B, 1994. **49**(8): p. 5133-5141.
25. Freris, I., et al., *Synthesis and optical properties of sub-micron sized rare earth-doped zirconia particles.* Optical Materials, 2011. **33**(11): p. 1745-1752.
26. Liu, Y.K., et al., *Synthesis and characterization of zirconia nanorods.* Journal of the American Ceramic Society, 2002. **85**(12): p. 3120-3122.
27. Widoniak, J., S. Eiden-Assmann, and G. Maret, *Synthesis and characterisation of monodisperse zirconia particles.* European Journal of Inorganic Chemistry, 2005(15): p. 3149-3155.
28. Baez-Rodriguez, A., et al., *Luminescent properties of ZrO2:Dy3+ and ZrO2:Dy3+ +Li+ films synthesized by an ultrasonic spray pyrolysis technique.* Ceramics International, 2015. **41**(5): p. 7197-7206.
29. Raileanu, M., et al., *Sol-gel zirconia-based nanopowders with potential applications for sensors.* Ceramics International, 2015. **41**(3): p. 4381-4390.
30. Wang, M.L., et al., *Preparation and photoluminescence properties of Eu3+-doped ZrO2 nanotube arrays.* Ceramics International, 2015. **41**(7): p. 8444-8450.
31. Hess, B.A., Jr., et al., *Role of the antenna in tissue selective probes built of lanthanide-organic chelates.* Journal of Physical Chemistry A, 2008. **112**(11): p. 2397-2407.
32. Song, B., et al., *Time-resolved lanthanide luminescence for lab-on-a-chip detection of biomarkers on cancerous tissues.* Analyst, 2009. **134**(10): p. 1991-1993.
33. Buenzli, J.-C.G., et al., *Lanthanide bimetallic helicates for in vitro imaging and sensing*, in *Fluorescence Methods and Applications: Spectroscopy, Imaging, and Probes*, O.S. Wolfbeis, Editor. 2008. p. 97-105.
34. Montgomery, C.P., et al., *Cell-Penetrating Metal Complex Optical Probes: Targeted and Responsive Systems Based on Lanthanide Luminescence.* Accounts of Chemical Research, 2009. **42**(7): p. 925-937.
35. Dos Santos, C.M.G., et al., *Recent developments in the field of supramolecular lanthanide luminescent sensors and self-assemblies.* Coordination Chemistry Reviews, 2008. **252**(23-24): p. 2512-2527.
36. Fan, Y., et al., *Luminescent and Mesoporous Europium-Doped Bioactive Glasses (MBG) as a Drug Carrier.* Journal of Physical Chemistry C, 2009. **113**(18): p. 7826-7830.
37. Cao, G. and Y. Wang, *Nanostructures and Nanomaterials: Synthesis, Properties, and Applications*. World scientific series in nanoscience and nanotechnology. 2011: World Scientific.
38. Turkevich, J., G. Garton, and P.C. Stevenson, *The color of colloidal gold.* Journal of Colloid Science, 1954. **9, Supplement 1**(0): p. 26-35.
39. Turkevich, J., P.C. Stevenson, and J. Hillier, *The Formation of Colloidal Gold.* The Journal of Physical Chemistry, 1953. **57**(7): p. 670-673.
40. Frens, G., *Controlled Nucleation for the Regulation of the Particle Size in Monodisperse Gold Suspensions.* Nature Physical Science 1973. **241**: p. 20-22.
41. Brust, M., et al., *SYNTHESIS OF THIOL-DERIVATIZED GOLD NANOPARTICLES IN A 2-PHASE LIQUID-LIQUID SYSTEM.* Journal of the Chemical Society-Chemical Communications, 1994(7): p. 801-802.
42. Martin, M.N., et al., *Charged Gold Nanoparticles in Non-Polar Solvents: 10-min Synthesis and 2D Self-Assembly.* Langmuir, 2010. **26**(10): p. 7410-7417.
43. Chow, M.K. and C.F. Zukoski, *Gold Sol Formation Mechanisms: Role of Colloidal Stability.* Journal of Colloid and Interface Science, 1994. **165**(1): p. 97-109.
44. Busser, G.W., J.G. van Ommen, and J.A. Lercher, *Preparation and characterization of polymer-stabilized rhodium sols. I. Factors affecting particle size.* Journal of Physical Chemistry B, 1999. **103**(10): p. 1651-1659.

45. Duff, D.G., A. Baiker, and P.P. Edwards, *A NEW HYDROSOL OF GOLD CLUSTERS .1. FORMATION AND PARTICLE-SIZE VARIATION.* Langmuir, 1993. **9**(9): p. 2301-2309.
46. Fendler, J.H. and F.C. Meldrum, *THE COLLOID-CHEMICAL APPROACH TO NANOSTRUCTURED MATERIALS.* Advanced Materials, 1995. **7**(7): p. 607-632.
47. Hostetler, M.J., et al., *Alkanethiolate gold cluster molecules with core diameters from 1.5 to 5.2 nm: Core and monolayer properties as a function of core size.* Langmuir, 1998. **14**(1): p. 17-30.
48. Leff, D.V., et al., *THERMODYNAMIC CONTROL OF GOLD NANOCRYSTAL SIZE - EXPERIMENT AND THEORY.* Journal of Physical Chemistry, 1995. **99**(18): p. 7036-7041.
49. Reetz, M.T. and W. Helbig, *SIZE-SELECTIVE SYNTHESIS OF NANOSTRUCTURED TRANSITION-METAL CLUSTERS.* Journal of the American Chemical Society, 1994. **116**(16): p. 7401-7402.
50. Teranishi, T., et al., *Size control of monodispersed Pt nanoparticles and their 2D organization by electrophoretic deposition.* Journal of Physical Chemistry B, 1999. **103**(19): p. 3818-3827.
51. Teranishi, T. and M. Miyake, *Size control of palladium nanoparticles and their crystal structures.* Chemistry of Materials, 1998. **10**(2): p. 594-600.
52. Volokitin, Y., et al., *Quantum-size effects in the thermodynamic properties of metallic nanoparticles.* Nature, 1996. **384**(6610): p. 621-623.
53. Zhao, M.Q., L. Sun, and R.M. Crooks, *Preparation of Cu nanoclusters within dendrimer templates.* Journal of the American Chemical Society, 1998. **120**(19): p. 4877-4878.
54. Ahmadi, T.S., et al., *Shape-controlled synthesis of colloidal platinum nanoparticles.* Science, 1996. **272**(5270): p. 1924-1926.
55. Bradley, J.S., et al., *Surface spectroscopic study of the stabilization mechanism for shape-selectively synthesized nanostructured transition metal colloids.* Journal of the American Chemical Society, 2000. **122**(19): p. 4631-4636.
56. Petroski, J.M., et al., *Kinetically controlled growth and shape formation mechanism of platinum nanoparticles.* Journal of Physical Chemistry B, 1998. **102**(18): p. 3316-3320.
57. Jana, N.R., L. Gearheart, and C.J. Murphy, *Seed-mediated growth approach for shape-controlled synthesis of spheroidal and rod-like gold nanoparticles using a surfactant template.* Advanced Materials, 2001. **13**(18): p. 1389-1393.
58. Jana, N.R., L. Gearheart, and C.J. Murphy, *Evidence for seed-mediated nucleation in the chemical reduction of gold salts to gold nanoparticles.* Chemistry of Materials, 2001. **13**(7): p. 2313-2322.
59. Xiao, J. and L. Qi, *Surfactant-assisted, shape-controlled synthesis of gold nanocrystals.* Nanoscale, 2011. **3**(4): p. 1383-1396.
60. Wojciech L. Suchanek and R.E. Riman, *Hydrothermal Synthesis of Advanced Ceramic Powders.* Advances in Science and Technology, 2006. **45**: p. 184-193.
61. Chan, W.C.W., et al., *One-step conjugation of biomolecules to luminescent nanocrystals*, in *Molecular Imaging: Reporters, Dyes, Markers, and Instrumentation*, D.J. Bornhop and K. Licha, Editors. 2000. p. 2-9.
62. Cho, S., et al., *Facile fabrication of two-dimensional inorganic nanostructures and their conjugation to nanocrystals.* Journal of Materials Chemistry C, 2013. **1**(29): p. 4497-4504.
63. Guo, W.Z., et al., *Conjugation chemistry and bioapplications of semiconductor box nanocrystals prepared via dendrimer bridging.* Chemistry of Materials, 2003. **15**(16): p. 3125-3133.
64. Iafisco, M., et al., *Conjugation of hydroxyapatite nanocrystals with human immunoglobulin G for nanomedical applications.* Colloids and Surfaces B-Biointerfaces, 2012. **90**: p. 1-7.
65. Liu, J.Q., et al., *Crosslinking and conjugation of water-soluble semiconductor nanocrystals (quantum dots) and their biological applications.* Abstracts of Papers of the American Chemical Society, 2002. **224**: p. U421-U421.
66. Sarkar, R., et al., *Direct conjugation of semiconductor nanocrystals to a globular protein to study protein-folding intermediates.* Journal of Physical Chemistry B, 2007. **111**(42): p. 12294-12298.
67. Zhou, X., et al., *The effect of conjugation to gold nanoparticles on the ability of low molecular weight chitosan to transfer DNA vaccine.* Biomaterials, 2008. **29**(1): p. 111-117.

68. Yokota, S., et al., *Synthesis of Gold Nanoparticles for In Situ Conjugation with Structural Carbohydrates.* Angewandte Chemie-International Edition, 2008. **47**(51): p. 9866-9869.
69. Kumar, S.A., Y.A. Peter, and J.L. Nadeau, *Facile biosynthesis, separation and conjugation of gold nanoparticles to doxorubicin.* Nanotechnology, 2008. **19**(49): p. 10.
70. Maus, L., et al., *Conjugation of Peptides to the Passivation Shell of Gold Nanoparticles for Targeting of Cell-Surface Receptors.* Acs Nano, 2010. **4**(11): p. 6617-6628.
71. Liu, K., et al., *Biocompatible Gold Nanorods: One-Step Surface Functionalization, Highly Colloidal Stability, and Low Cytotoxicity.* Langmuir, 2015. **31**(17): p. 4973-4980.
72. Smith, M.C., et al., *Quantitative analysis of PEG-functionalized colloidal gold nanoparticles using charged aerosol detection.* Analytical and Bioanalytical Chemistry, 2015. **407**(13): p. 3705-3716.
73. Murphy, S., L. Huang, and P.V. Kamat, *Charge-Transfer Complexation and Excited-State Interactions in Porphyrin-Silver Nanoparticle Hybrid Structures.* Journal of Physical Chemistry C, 2011. **115**(46): p. 22761-22769.
74. Ru, E.L. and P. Etchegoin, *Principles of Surface-Enhanced Raman Spectroscopy: and related plasmonic effects*. 2008: Elsevier Science.
75. Lenka Kolářová, et al., *Tissue Visualization Mediated by Nanoparticles: From Tissue Staining to Mass Spectrometry Tissue Profiling and Imaging*, in *Nanomedicine*, A.d.M. Alexander Seifalian, Deepak M. Kalaskar, Editor. 2014: Manchester (UK). p. 467-488.

CHAPTER 2

ZrO_2:Yb^{3+}-Er^{3+} NANOPARTICLES WITH UPCONVERSION EMISSION FOR LABELING HELA CELLS

2.1 Introduction

2.2 Experimental

2.3 Structural characterization (XRD, RAMAN, HRTEM, SEM, FT- IR)

2.4 Optical characterization

2.5 Zeta Potential and Dynamic Light Scattering Measurements (DLS)

2.6 Results and Discussion

2.7 Conclusions

2.8 References

2.1 Introduction

Lanthanide-doped nanomaterials are promising platforms for bio-applications due to their ability to convert low-energy near-infrared (NIR) radiation into higher-energy visible luminescence through a process named upconversion (UPC) [76, 77]. There are several potential benefits for the use of nanocrystals with UPC emission in biological applications such as: no damage of tissues; anti-Stokes emission; long lifetimes; photo-stability; increased contrast in biological specimens due to the absence of autofluorescence upon excitation with IR light; and simultaneous detection of multiple targeted analytes [78-81]. Other advantages of the up-conversion emission are the reduction of photobleaching and scattering in tissues, which avoid the use of complicated and high-cost femtosecond lasers and photomultiplier tubes [82-85]**.**

For biomedical applications such as cancer detection, biolabeling and bioimaging; luminescent nanoparticles preferably have to form a stable colloidal solution under physiological conditions. However, common nanomaterials with strong upconversion emission such as Yb^{3+}-Er^{3+} co-doped Y_2O_2S, Yb^{3+}-Ho^{3+} co-doped Y_2O_3, Yb^{3+}-Er^{3+}-Tm^{3+} doped $NaYF_4$ are hydrophobic [86-88]. Some efforts have been made to convert hydrophobic upconversion nanoparticles into hydrophilic ones using techniques such as polymer capping, surface silanization, and surface ligand oxidation [88-93]. Recent methods also include ligand exchange in $NaGdF_4$: Ho^{3+}-Yb^{3+} and $NaYF_4$:Yb^{3+}-Er^{3+} phosphors [94].

Cancer detection in early stages is a priority for many medical groups around the world. In 2012, according to World Health Organization (WHO), cervical cancer was one of the most prevalent cancer types in the world. To detect and diagnose cancer, there are several biomarkers [95-98]; for example, Ki-67 protein is expressed in all phases of the cell division cycle, but its expression level is strongly down regulated in the resting G0 phase. This characteristic makes Ki67 protein an excellent biomarker for cell proliferation [99-101]. This biomolecule can be used as a prognostic marker in many types of cancers [102-106]. Moreover, it has been demonstrated that cervical human cancer (HeLa) cells can be labeled using doped or undoped nanomaterials such as, $NaYF_4$:Yb^{3+}-Er^{3+}, $NaYF_4$:Yb^{3+}-Er^{3+}@CaF_2 core@shell, $NaGdF_4$:Yb^{3+}-Er^{3+}/Silica/Au, CaF_2 and carbon nanoparticles. These nanomaterials were internalized in HeLa cells observing visible light from the nanoparticles under infrared excitation [107-111]. Despite these platforms are efficient to label HeLa cells, they still show several problems related to the complexity of their

fabrication. For example, the synthesis of $NaGdF_4:Yb^{3+},Er^{3+}$ nanoparticles have some drawbacks for biomedical applications; therefore, gold or silica need to be used to render them biocompatible properties [112-114]. In addition, one of the problems with carbon nanoparticles is the fact that they need to be excited with near UV light, which can damage tissues around the cancer cells [109].

Rare earth doped zirconia (ZrO_2) nanophosphors present efficient emission in the visible region when they are under infrared excitation [115-117]. The ZrO_2 low phonon energy (470 cm^{-1}) increases the number and the probability of radiative transitions in rare earth doped ZrO_2 [118]. Strong upconversion emission has been obtained doping ZrO_2 with different pairs of rare earths such as Yb^{3+}–Tm^{3+}, Yb–Ho^{3+}, Er^{3+} and Yb^{3+}–Er^{3+} [119]. Furthermore, ZrO_2 nanophosphors can be synthesized by low cost methods such as sol–gel [120, 121], sol–emulsion–gel [122, 123], spray pyrolysis [124, 125] and precipitation [126]. Interestingly, ZrO_2 is a non-toxic material, it has been used as biocompatible dental material to make pigments [127-130]. Due to all those reasons, ZrO_2 is an excellent candidate for developing novel biolabeling and bioimaging platforms. In this work, $ZrO_2:Yb^{3+}$–Er^{3+} nanocrystals were chemically conjugated with antiKi-67 protein by a novel method using (3-aminopropyl)triethoxysilane (APTES) and conjugated Biotin molecules as ligands. To the best of our knowledge, there are no reports about the use of luminescent $ZrO_2:Yb^{3+},Er^{3+}$ nanocrystals to label HeLa cells. Furthermore, the effect of the ligands on the luminescent properties of these nanoparticles was studied. In addition, the internalization of the conjugated nanoparticles in HeLa cells was followed by looking at their strong red luminescence using two-photon confocal microscopy. The results show the successful uptake of conjugated $ZrO_2:Yb^{3+}$-Er^{3+} nanoparticles in HeLa cells. We envision that this is a promising method for labeling different types of cancer cells for biosensing and bioimaging purposes.

2.2 Experimental

2.2.1 Preparation of $ZrO_2:Yb^{3+}$-Er^{3+} Nanoparticles

$ZrO_2:Yb^{3+}$-Er^{3+} nanoparticles were prepared following a precipitation process previously reported with some modifications [131]. $ZrOCl_2 \cdot 8H_2O$ and $YbCl_3 \cdot 6H_2O$ (99.9%) were purchased from Aldrich, and $ErCl_3 \cdot 6H_2O$ (99.99%) was acquired from RE Acton. The ammonium hydroxide

(NH_4OH) at 30 vol% was supplied by Karal. In a typical experiment, Yb^{3+}-Er^{3+} co-doped ZrO_2 with a molar ratio of 2:1 for Yb^{3+}:Er^{3+} was prepared by dissolving 2.6333 g of $ZrOCl_2$, 0.2362 g of $YbCl_3 \cdot 6H_2O$ (2 mol % of Yb_2O_3) and 0.1351 g of $ErCl_3 \cdot 6H_2O$ (1 mol % of Er_2O_3) in 50 ml of a mixture of H_2O/EtOH (1:1 wt%). After 15 minutes under stirring, the non-ionic surfactant Pluronic F127 was introduced in the mixture at molar ratio of $F127/ZrO_2 = 0.0082$. Afterwards, 30 ml of NH_4OH was added to precipitate the salts. The resulted suspensions were transferred into a sealed autoclave and a hydrothermal treatment was carried out at 80º C for 12 hours. After this, the autoclave was allowed to cool down for 30 minutes and the solutions were washed twice with absolute ethanol and water in a centrifuge at 4000 rpm for 10 minutes. Subsequently, the powders were put in a ceramic crucible and dried at 80º C for 12 hours. Finally, all samples were annealed at 1000º C using a heating rate of 5 ºC/min.

2.2.2 Conjugation and Functionalization of ZrO2:Yb3+-Er3+ nanoparticles

The conjugation of ZrO_2:Yb^{3+}-Er^{3+} nanoparticles with Ki67 protein was carried out by following a previously reported method with some modifications [90]. This process was performed as follows: 0.1 g of Yb^{3+}-Er^{3+} doped ZrO_2 nanoparticles were stirred with 490 µl of APTES for 24 hours. This bifunctional compound has amine- and alkoxysilane groups. The alkoxysilane reacts with the OH moieties on the ZrO_2:Yb^{3+}-Er^{3+} nanoparticles surface, leaving the amino groups exposed for further functionalization. The samples were washed once with ethanol and water to eliminate the excess of residues, and centrifuged at 6000 rpm for 10 min. The samples were dried at 40 ºC for 12 hours. The Yb^{3+}-Er^{3+} co-doped ZrO_2 nanoparticles coated with APTES were dispersed in 670 µl of PBS 1X (Phosphate Buffered Saline, pH = 7.4) and then 200 µl of 1:500 Biotin-anti-rabbit (mouse IgG) from BIOCARE was added to the suspension to bind the carboxyl groups of the IgG with the amino groups exposed in the nanoparticles, this suspension were kept at 4 °C for 12 hours. After that, the nanoparticles were washed with distilled water and centrifuged at 6000 rpm for 10 min to remove the supernatant. The conjugated material was kept at 37 °C for 12 hours. Subsequently, 300 µl of PBS 1X and 10 µl of antigen Ki-67- rabbit antibody from BIOCARE were added to the nanoparticles and stored for another 12 hours at 4 °C. Finally, the conjugated ZrO_2:Yb^{3+}-Er^{3+} nanoparticles were washed with distilled water and centrifuged at 6000 rpm for 10 min. The final material was dispersed and stored in distilled water.

2.3 Structural Characterization (XRD, Raman, HRTEM, SEM, FT-IR)

X-ray diffraction (XRD) patterns were obtained using a SIEMENS D-5005 equipment using a Cu tube with Kα radiation at 1.5405 Å, scanning in the 20–80° 2θ range with increments of 0.02° and a sweep time of 2 s. RAMAN patterns were obtained using a Renishaw Raman System (inVia Raman Microscope), which uses a 785 nm laser and a 50x objective. The nanoparticles were suspended in isopropyl alcohol at room temperature and dispersed with ultra-sonication. Afterwards, the solution of nanoparticles was dropped on 3 mm diameter lacey carbon copper grids to obtain the HRTEM images in a FEI Titan 80-300 with accelerating voltage set to 300 kV. In addition, the nanoparticles micrographs were obtained by a SEM Hitachi SU8010 at 30.0 kV. The Fourier transform infrared (FTIR) spectra were obtained using a Perkin-Elmer spectrophotometer with a DTGS detector and a spectral resolution of 4 cm^{-1}. The samples were prepared using the KBr pellet method and the spectra were obtained in the range of 1000 to 4000 cm^{-1}.

2.4 Optical Characterization

2.4.1 Photoluminescence Characterization

Photoluminescence (PL) characterization was performed using a CW semiconductor laser diode with an excitation power of 350 mW and centered at 970 nm. The luminescence emission was analyzed with a Spectrograph Spectra Pro 2300i and a R955 photomultiplier tube from Hamamatsu. The system was PC controlled with Spectra Sense software. The samples were supported in 1 mm capillary tubes in order to guarantee the same quantity of excited material. Special care was taken to maintain the alignment of the setup in order to compare the intensities between different characterized samples. All measurements were performed at room temperature.

2.4.2 Incubation and Confocal Microscopy

HeLa cells were grown at a density of 5 x 10^4 cells/mL in a six-well culture plates with coverslips at the bottom of them and incubated in 3 mL of RPMI-1640 cell media for 24 hr at 37 °C under 5% CO_2. After this, the cell media was replaced by 3 ml of ZrO_2:Yb^{3+}-Er^{3+} nanoparticles,

ZrO_2:Yb^{3+}-Er^{3+}-APTES, and ZrO_2:Yb^{3+}-Er^{3+}-APTES-Biotin-Anti-rabbit/rabbitAntibody-antiKi67 with a concentration of 100 μg/mL and incubated for 6h. Finally, the cell-plated coverslips corresponding to each sample were washed twice with PBS buffer (1mM, pH 7.4) and stained with nuclei-staining NucBlue® Live solution for 15 min. All the cell-plated coverslips were fixed with a solution of 4% formaldehyde. The fixed and stained coverslips were placed in microscope slides and analyzed under a two-photon Olympus FV1000 MPE SIM Laser Scanning Confocal Microscope.

2.5 Zeta Potential and Dynamic Light Scattering Measurements (DLS)

Dynamic light scattering (DLS) and zeta potential measurements were carried out using a Malvern Instrument Zetasizer Nano (red laser 633 nm). The samples were dispersed in PBS (1 mM, pH = 7.4) with a concentration of 1 mg/mL. The DLS and Zeta-potential were analyzed at 25 °C.

2.6 Results and Discussion

2.6.1 Crystalline Structure and Morphology

The XRD pattern of the ZrO_2:Yb^{3+}-Er^{3+} nanopowder is shown in Figure 2.1(a). This plot shows peaks corresponding to (1,0,1), (0,1,1), (2,1,1) and (1,1,2) planes, respectively. All the peaks are associated to the tetragonal phase of zirconia, according to JCPDS 37-1413 card [132]. The ZrO_2:Yb^{3+}-Er^{3+} nanopowder obtained by precipitation method was analyzed by Raman spectroscopy, see Figure 2.1(b). The peaks at 626, 552, 525, 445, 336, 260, 238 and 185 cm^{-1} represent the spectrum. The peaks located at 445 cm^{-1} and 626 cm^{-1} as well as the shoulders located at 185 cm^{-1} and 260 cm^{-1} are in agreement with the tetragonal phase of zirconia [133].

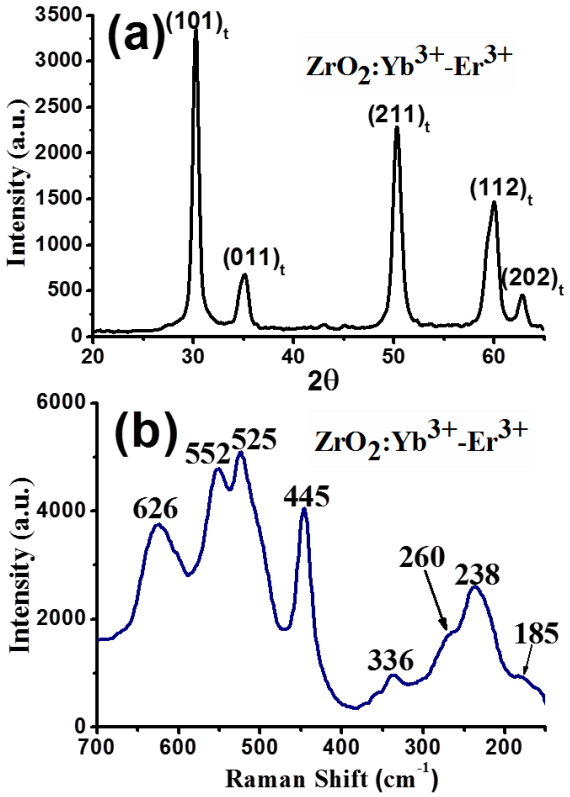

Figure 2.1 Structural characterization of ZrO2:Yb3+-Er3+ nanocrystals: (a) X-Ray diffraction (b) Raman spectroscopy, using a laser of 785 nm.

The nanocrystals sizes were determined by TEM and a representative micrograph is presented in Figure 2.2(a). The nanocrystals have an average size of 20 nm and spherical shape. Besides, Figure 2.2(b) is a SEM image which shows well-dispersed nanocrystals and this was caused by the introduction of PF127 during the synthesis process [134]. The size and dispersion of the co-doped ZrO_2:Yb^{3+}-Er^{3+} nanocrystals was controlled from the nucleation process due to the presence of ammonia, water/ethanol and surfactant Pluronic PF127 [131]. To promote the efficient internalization in HeLa cells, it is important to have particles in the nanoscale size regime. In addition, the colloidal stability of the nanoparticles is also significant to avoid the formation of aggregates, which may prevent the effective interaction between the nanoparticles and the cell surface.

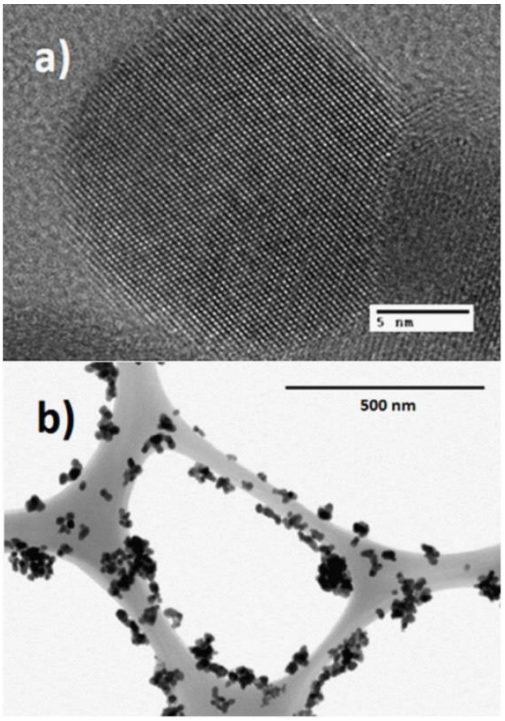

Figure 2.2 (a) TEM image and (b) SEM image of ZrO2:Yb3+-Er3+ nanoparticles.

2.6.2 FT-IR, Zeta Potential and DLS

Figure 2.3 shows the FTIR spectra of ZrO_2:Yb^{3+}-Er^{3+} nanocrystals and ZrO_2:Yb^{3+}-Er^{3+} prepared with APTES, Biotin-Anti-rabbit(Mouse IgG) and RabbitAntibody-AntiKi-67, respectively. These spectra provide information regarding functional groups and impurities on the surface of nanoparticles. They also corroborated that the process of functionalization and conjugation was successfully achieved. Figure 2.3(a) shows the FTIR spectra of non-functionalized nanoparticles ZrO_2:Yb^{3+}-Er^{3+}. It depicts small peaks associated to OH groups in the range of 3200 cm^{-1} to 3600 cm^{-1}. Moreover, a peak is also observed at 450 cm^{-1}, which is related with Zr-O stretching vibrations [135]. The spectrum in Figure 2.3(b) shows a broadening of the bands centered at 3600 and 564 cm^{-1} due to the presence of Si-OH and Si-O-Si bonds respectively [136, 137]. Other peaks at about 2923cm^{-1} and 2351 cm^{-1} are related with C-H bonds and CO_2 impurities, respectively. The band located in the range of 3000 cm^{-1}-3400 cm^{-1} is associated with amine groups [138, 139]. The CO_2 impurities adsorbed in the surface of the nanoparticles can come from the synthesis and/or the environment during the measurement process, which was probably caused

by the granular characteristic of the nanopowder. The OH groups were introduced during the hydrolysis and condensation process where the M-OH (M=Zr, Er, and Yb) bond was formed due to the excess of hydroxyls in solution. According to the FTIR spectra in Figures 2.3(a) and 2.3(b) the contamination produced by those hydroxyl groups is very low. Biotin-Anti-rabbit (Mouse IgG) protein is conjugated to the nanoparticles containing APTES by forming an amide bond between the free amino groups located at the surface of ZrO_2:Yb^{3+}-Er^{3+}/APTES and the carboxyl groups exposed in the IgG protein. The ZrO_2:Yb^{3+}-Er^{3+}/APTES/Biotin FTIR spectrum is shown in Figure 2.3(c), the spectrum illustrates a new band associated to the amide bon at 1770 cm^{-1}. Moreover, a peak centered at 658 cm^{-1} is also associated to Biotin according to literature [140, 141]. These data further comfirms the functionalization of nanoparticles. The next step is to analyze the process of conjugation with the antigen Ki-67-rabbit Antibody (ZrO_2:Yb^{3+}-Er^{3+}/APTES/Biotin/AntiKi-67), see Figure 2.3(d). The bands related with Biotin are still observed and there is a general decrease of the peaks related with impurities such as CO_2 and OH radicals. However, it is observed that there is a widening of the 658 cm^{-1} band when AntiKi-67 is adding. Based on this information, it is expected that AntiKi-67 is readily available to interact with HeLa cells.

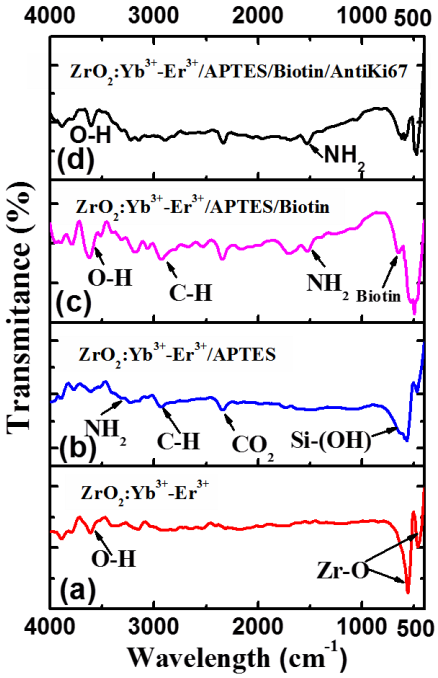

Figure 2.3 FTIR spectra of ZrO2:Yb3+-Er3+, ZrO2:Yb3+-Er3+/APTES, ZrO2:Yb3+-Er3+/APTES/ Biotin and ZrO2:Yb3+-Er3+/APTES/Biotin/AntiKi67.

The conjugation of the nanoparticles was also analyzed by Zeta-potential and DLS measurements see Table 2.1. Zeta-potential changed from negative to positive when the ZrO_2:Yb^{3+}-Er^{3+} nanoparticles surface is modified with APTES, as an indication that the amino groups are covering the nanoparticles surface. Moreover, the Zeta-potential was shifted from positive to negative after Biotin and Antigen Ki-67 proteins were chemically attached to the surface of the material, suggesting the presence of carboxylate groups [142, 143]. The value of -36 mV obtained in ZrO_2:Yb^{3+}-$Er^{3+/}$APTES/Biotin/AntiKi67 also indicates that nanoparticles can be stable in PBS due to their high electrostatic repulsion, which is suitable for bioapplications. A high negative value also suggests a high adsorption of nanoparticles on the nucleus of HeLa Cells [144]. Moreover, DLS measurements showed that the hydrodynamic diameter of the nanoparticles increased when the different molecules were added, the average sizes for ZrO_2:Yb^{3+}-Er^{3+}, ZrO_2:Yb^{3+}-Er^{3+}/APTES and ZrO_2:Yb^{3+}-Er^{3+}/APTES/ Biotin/AntiKi-67 were 748 nm, 1232 nm and 4694 nm, see Table 2.1. The size of the nanoparticles in ZrO_2:Yb^{3+}-Er^{3+} does not coincide with that one measured with TEM, probably due to the agglomeration of nanoparticles that were dispersed in PBS.

Table 2.1 Nanoparticle characterization using DLS and Zeta Potential for ZrO_2:Yb^{3+}-Er^{3+}, ZrO_2:Yb^{3+}-Er^{3+}-APTES and ZrO_2:Yb^{3+}-Er^{3+}-APTES-Biotin-AntiKi67 nanocrystals.

	ZrO_2:Yb^{3+}-Er^{3+}	**ZrO_2:Yb^{3+}-Er^{3+}-APTES**	**ZrO_2:Yb^{3+}-Er^{3+}-APTES-Biot-AntiKi67**
DLS (d, nm)	**748**	**1232**	**4694**
Zeta potential (mV)	**-36.8**	**+10.8**	**-36.0**

Figure 2.4 shows a schematic representation for the functionalization and conjugation of the nanoparticles. The OH moieties produced after ZrO_2:Yb^{3+}-Er^{3+} synthesis react with the alkoxysilane groups of APTES to afford a silica shell on the nanoparticles leaving the amine

groups exposed onto the surface of the material. In the next step of the reaction, the Biotin-Anti-rabbit (mouse IgG) molecule is conjugated to the amino groups by using the COOH moieties of the IgG. At this point, the Anti-rabbit can interact with the biomolecule AntiKi67-Rabbit Antibody.

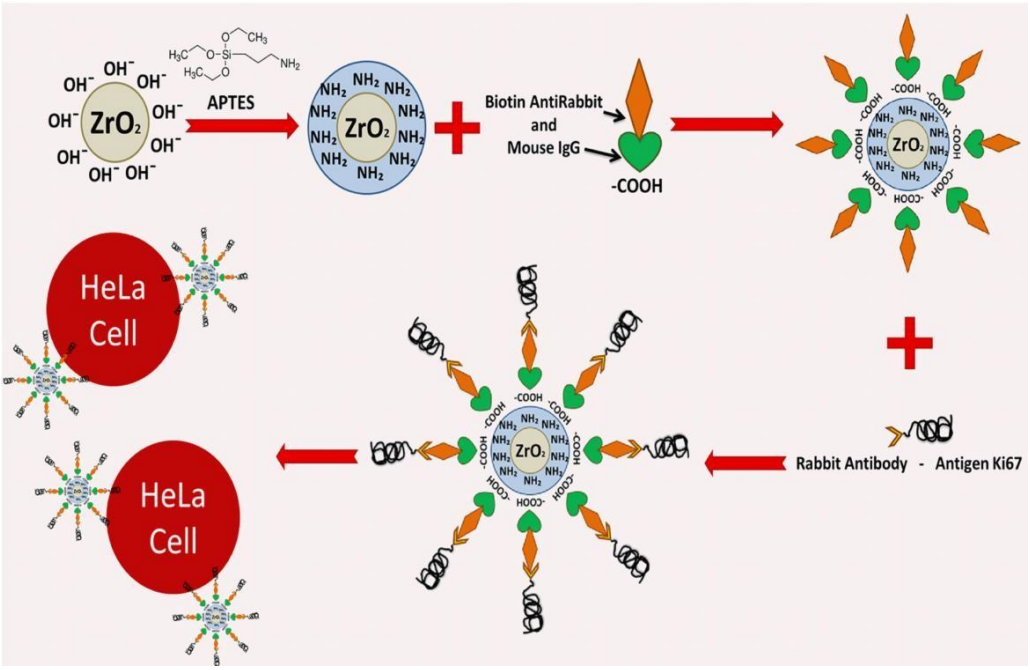

Figure 2.4 Schematic representation of the functionalization and conjugation of ZrO_2:Yb^{3+}-Er^{3+} nanoparticles.

2.6.3 Luminescent Properties

The mechanism of up-conversion emission in Er^{3+}–Yb^{3+} co-doped ZrO_2 is well established in the literature [145]. Figure 2.5 shows a strong red emission band with peaks at 653 nm and 657 nm as well as a weak green band after excitation at 970 nm. Green and red emission bands are assigned to $^2H_{11/2}+^4S_{3/2}\rightarrow{}^4I_{15/2}$ and $^4F_{9/2}\rightarrow{}^4I_{15/2}$ transitions of the Er^{3+} ion and they are caused by the successive absorption of two photons after energy transfer from Yb^{3+} ions [134]. According to previous works, the emission is predominantly red because OH groups have a vibrational energy (3000 cm^{-1}-4000 cm^{-1}) which produces non-radiative relaxations from the mixed level $^2H_{11/2}+^4S_{3/2}$ toward the $^4F_{9/2}$ level [146]. In our case, the presence of OH moieties in all samples is corroborated by the FTIR spectra in Figure 2.3. The inset in Figure 2.5 shows that the integrated

emission corresponds to the red band. Moreover, it is observed that the red emission of the samples ZrO_2:Yb^{3+}-Er^{3+}/APTES (Z-A) and ZrO_2:Yb^{3+}-Er^{3+}/APTES/Biotin (Z-A-B) decreases progressively respect to the sample of reference without conjugated (ZrO_2:Yb^{3+}-Er^{3+}) (Z). Nevertheless the emission is improved when the nanoparticles were conjugated with AntiKi67 (APTES-Biotin-AntiKi-67) (Z-A-B-K). The integrated red emission diminished with the addition of APTES and Biotin molecules because other contaminants such as CO_2, C-H and amine groups appeared and the presence of hydroxyls increased. These elements may act as quenching centers of luminescence and also create defects which behave as traps for luminescence [146, 147]. It is important to point out that the sample with APTES-Biotin had the highest levels of impurities (see figure 2.3(c)), therefore it showed the lowest luminescence. In contrast, the sample with APTES-Biotin-AntiKi67 had the lowest amount of contaminants (OH, CO_2 and C-H) (see Figure 2.3(d)); and therefore, it presented the highest red emission, see Figure 2.5.

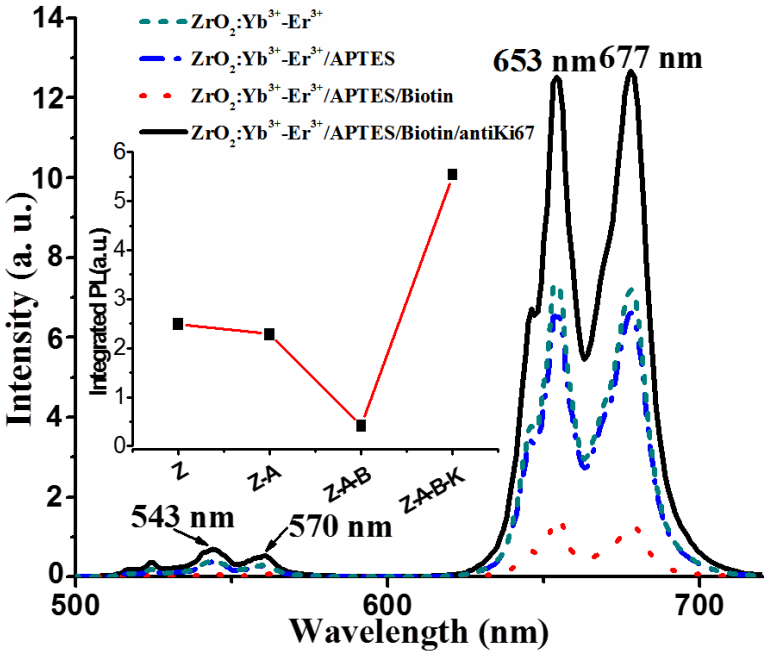

Figure 2.5 Photoluminescence spectra of ZrO2:Yb3+-Er3+, ZrO2:Yb3+-Er3+/APTES, ZrO2:Yb3+-Er3+/APTES/Biotin and ZrO2:Yb3+-Er3+/APTES/Biotin/AntiKi67. Inset shows the integrated emission of the samples.

2.6.4 Imaging of ZrO_2:Yb^{3+}-Er^{3+} Nanocrystals incubated in HeLa Cells

Figure 2.6 shows the images obtained by the two-photon confocal microscope after HeLa cells were incubated with the different materials synthesized in this work. Figure 2.6(a) shows that the ZrO_2:Yb^{3+}-Er^{3+} nanoparticles are situated out of the cell, probably due of to the negative charge on the surface of the nanoparticles, which limits the internalization in HeLa cells. Figure 2.6(b) depicts ZrO_2:Yb^{3+}-Er^{3+} /APTES nanoparticles located on the cytoplasm of HeLa cells, these nanoparticles have no antiKi67, but they have APTES on their surface, this indicates that the positive charge on the surface of the nanoparticles enhance the internalization in HeLa cells. Figures 2.6(c) is an image of HeLa cells with nanoparticles conjugated with antiKi-67, it is observed that 6 hours of incubation is sufficient to reach the cytoplasm of HeLa cells. It is observed that there are a greater number of particles within the cell and near the nucleus. The most accepted theory is that nanoparticles are internalized via endosome-mediated transport or through ribosome exchanges [108]. In general the red emission from nanoparticles is strong in all images, which demonstrates the efficient luminescence generated by the nanoparticles synthesized in this work. It is worthy to notice that there was no auto-fluorescence from the cells after exciting the UPC nanoparticles with 970 nm. Furthermore, these images denote different sizes of emission points this is probably induced by the nanoparticles conglomerations.

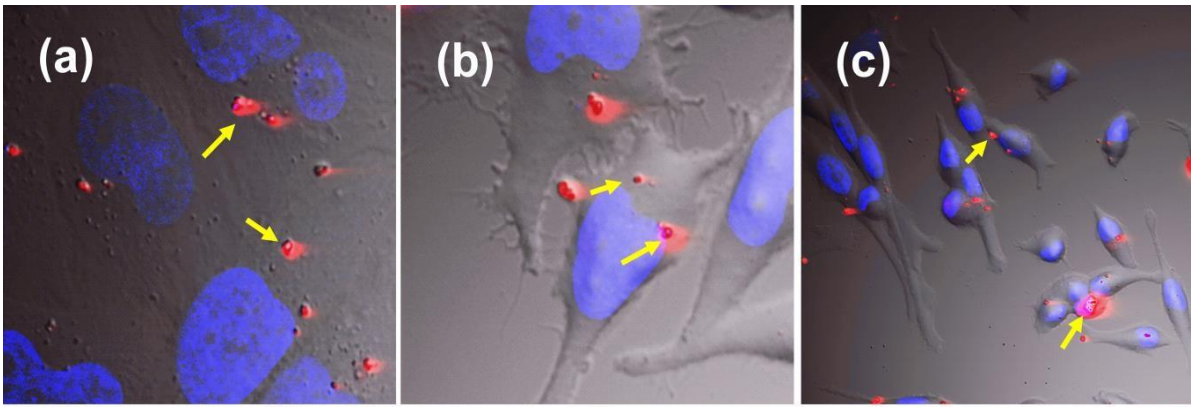

Figure 2.6 Confocal microscopy images of (a) ZrO2:Yb3+-Er3+, (b) ZrO2:Yb3+-Er3+/APTES, (c) ZrO2:Yb3+-Er3+/APTES/Biotin/AntiKi67 nanoparticles after 6 hours of incubation in HeLa cells.

Compared to other methods for conjugation of nanoparticles, our technique avoids the use of other elements such as carbon and citrate, which are relatively toxic [107, 109]. Moreover, it uses biomolecules (antigen and antibody) to lead our nanoparticle toward a targeted organelle; to the best of our knowledge, this kind of molecules has not been used on luminescent nanoparticles. Finally, further research is needed not only to improve the distribution and internalization of nanoparticles, but also to label specific organelles inside the HeLa cells. Those studies are in progress and they will be presented in a subsequent work.

2.7 Conclusions

In summary, we sconjugated Yb^{3+}-Er^{3+} co-doped ZrO_2 nanoparticles using Biotin-AntiRabbit(mouse IgG) and RabbitAntibody-AntiKi67 biomolecules. The successful conjugation was confirmed by FT-IR, Zeta-potential and DLS. The nanoparticles internalized in HeLa cells demonstrated a strong red luminescence and were observed using a two-photon confocal microscope. The photoluminescence spectra indicated that the up-conversion red emission of Er^{3+} ions is affected by the molecules located on the nanocrystals surface. An enhancement of the red emission was obtained in the nanoparticles with the conjugation with AntiKi-67. This was mainly caused by an enormous reduction of impurities compared to the rest of samples. Our results indicate that the method of conjugation depicted in this work can be a promising alternative to afford stable colloidal dispersions of nanoparticles in water and efficiently label cancer cells.

2.8 References

1. Li, X.M., F. Zhang, and D.Y. Zhao, *Highly efficient lanthanide upconverting nanomaterials: Progresses and challenges.* Nano Today, 2013. **8**(6): p. 643-676.
2. Wang, F. and X.G. Liu, *Multicolor Tuning of Lanthanide-Doped Nanoparticles by Single Wavelength Excitation.* Accounts of Chemical Research, 2014. **47**(4): p. 1378-1385.
3. Ong, L.C., et al., *Bacterial imaging with photostable upconversion fluorescent nanoparticles.* Biomaterials, 2014. **35**(9): p. 2987-2998.
4. Chen, F., et al., *Functionalized Upconversion Nanoparticles: Versatile Nanoplatforms for Translational Research.* Current Molecular Medicine, 2013. **13**(10): p. 1613-1632.
5. Chien, Y.H., et al., *Near-Infrared Light Photocontrolled Targeting, Bioimaging, and Chemotherapy with Caged Upconversion Nanoparticles in Vitro and in Vivo.* Acs Nano, 2013. **7**(10): p. 8516-8528.
6. Yust, B.G., F.J. Pedraza, and D.K. Sardar, *Ultrasmall lanthanide-doped nanoparticles as multimodal platforms*, in *Reporters, Markers, Dyes, Nanoparticles, and Molecular Probes for Biomedical Applications Vi*, S. Achilefu and R. Raghavachari, Editors. 2014, Spie-Int Soc Optical Engineering: Bellingham.
7. Li, D.Y., et al., *Multifunctional Y(2)0(3):Yb3+/Tm3+/Li+ Nanocrystals with Enhanced Near-infrared to Near-infrared Upconversion Photoluminescence*, in *New and Advanced Materials, Pts 1 and 2*, H.Y. Zhou, et al., Editors. 2011, Trans Tech Publications Ltd: Stafa-Zurich. p. 168-173.
8. Liu, Z., et al., *Near-Infrared Lanthanide Luminescence for Functional Materials.* Progress in Chemistry, 2011. **23**(1): p. 153-164.
9. Liu, T., et al., *Rare-Earth Upconversion Nanophosphors.* Progress in Chemistry, 2012. **24**(2-3): p. 304-317.
10. Gainer, C.F. and M. Romanowski, *A review of synthetic methods for the production of upconverting lanthanide nanoparticles.* Journal of Innovative Optical Health Sciences, 2014. **7**(2): p. 11.
11. Hwang, B.C., et al., *Cooperative upconversion and energy transfer of new high Er3+- and Yb3+-Er3+-doped phosphate glasses.* Journal of the Optical Society of America B-Optical Physics, 2000. **17**(5): p. 833-839.
12. Meltzer, R.S., et al., *Effect of the matrix on the radiative lifetimes of rare earth doped nanoparticles embedded in matrices.* Journal of Luminescence, 2001. **94**: p. 217-220.
13. Zako, T., et al., *Development of Near Infrared-Fluorescent Nanophosphors and Applications for Cancer Diagnosis and Therapy.* Journal of Nanomaterials, 2010.
14. Aldana, J., Y.A. Wang, and X.G. Peng, *Photochemical instability of CdSe nanocrystals coated by hydrophilic thiols.* Journal of the American Chemical Society, 2001. **123**(36): p. 8844-8850.
15. Corstjens, P.L.A.M., et al., *Infrared up-converting phosphors for bioassays* IEE Proc.-Nanobiotechnol, 2005. **152**(2): p. 64-72.
16. Kwon, H., et al., *Synthesis and Characterization of Poly(vinylpyrrolidone)-Capped Silicon-Nanoparticles.* Journal of Nanoscience and Nanotechnology, 2014. **14**(8): p. 5983-5987.
17. Wade, C.R., et al., *Postsynthetic tuning of hydrophilicity in pyrazolate MOFs to modulate water adsorption properties.* Energy & Environmental Science, 2013. **6**(7): p. 2172-2177.
18. Wei, K., X.M. Peng, and F. Zou, *Folate-decorated PEG-PLGA nanoparticles with silica shells for capecitabine controlled and targeted delivery.* International Journal of Pharmaceutics, 2014. **464**(1-2): p. 225-233.
19. Zhang, Q.B., et al., *NaYF4 : Yb3+, Er3+ Upconverting Nanoparticles Surface Ligand Exchange in Ternary Mixture Solvent and Optical Properties.* Chemical Journal of Chinese Universities-Chinese, 2014. **35**(2): p. 224-229.

20. Amaral, C.M.M., et al., *MDM2 polymorphism associated with the development of cervical lesions in women infected with Human papillomavirus and using of oral contraceptives.* Infectious Agents and Cancer, 2014. **9**: p. 8.
21. Bin Park, G., et al., *Antibody ligation of CM1 on cisplatin-exposed HeLa cells induces apoptosis through reactive oxygen species-dependent Fas ligand expression.* International Journal of Oncology, 2014. **44**(6): p. 2016-2024.
22. Guerra, F., et al., *Argentophilic nucleolus organizer region as a proliferation marker in cervical intraepithelial neoplasia grade 1 of the uterine cervix.* Journal of Obstetrics and Gynaecology Research, 2014. **40**(6): p. 1717-1724.
23. Samaga, K.K.L., et al., *Synthetic racemates of abyssinone I and II induces apoptosis through mitochondrial pathway in human cervix carcinoma cells.* Bioorganic Chemistry, 2014. **56**: p. 54-61.
24. Bullwinkel, J., et al., *Ki-67 protein is associated with ribosomal RNA transcription in quiescent and proliferating cells.* Journal of Cellular Physiology, 2006. **206**(3): p. 624-635.
25. Gerdes, J., et al., *CELL-CYCLE ANALYSIS OF A CELL PROLIFERATION-ASSOCIATED HUMAN NUCLEAR ANTIGEN DEFINED BY THE MONOCLONAL-ANTIBODY KI-67.* Journal of Immunology, 1984. **133**(4): p. 1710-1715.
26. Gerdes, J., et al., *PRODUCTION OF A MOUSE MONOCLONAL-ANTIBODY REACTIVE WITH A HUMAN NUCLEAR ANTIGEN ASSOCIATED WITH CELL-PROLIFERATION.* International Journal of Cancer, 1983. **31**(1): p. 13-20.
27. Bulten, J., et al., *MIB1, a promising marker for the classification of cervical intraepithelial neoplasia.* Journal of Pathology, 1996. **178**(3): p. 268-273.
28. Chan, D.W., et al., *Over-expression of FOXM1 transcription factor is associated with cervical cancer progression and pathogenesis.* Journal of Pathology, 2008. **215**(3): p. 245-252.
29. Kruse, A.J., et al., *Ki-67 immunoquantitation in cervical intraepithelial neoplasia (CIN): a sensitive marker for grading.* Journal of Pathology, 2001. **193**(1): p. 48-54.
30. Lobato, S., et al., *Minichromosome maintenance 7 protein is a reliable biological marker for human cervical progressive disease.* Journal of Gynecologic Oncology, 2012. **23**(1): p. 11-15.
31. Takagi, M., et al., *Ki67 Antigen Contributes to the Timely Accumulation of Protein Phosphatase 1 gamma on Anaphase Chromosomes.* Journal of Biological Chemistry, 2014. **289**(33): p. 22877-22887.
32. Cao, T.Y., et al., *Water-soluble NaYF4:Yb/Er upconversion nanophosphors: Synthesis, characteristics and application in bioimaging.* Inorganic Chemistry Communications, 2010. **13**(3): p. 392-394.
33. Sikora, B., et al., *Transport of NaYF4:Er3+, Yb3+ up-converting nanoparticles into HeLa cells.* Nanotechnology, 2013. **24**(23): p. 11.
34. Bhunia, S.K., et al., *Carbon nanoparticle-based fluorescent bioimaging probes.* Scientific Report 3, 2013(2045-2322 (Electronic)): p. 1473.
35. Ye-Fu Wang, L.-D.S., Jia-Wen Xiao, Wei Feng, Jia-Cai Zhou, Jie Shen and Chun-Hua Yan*, *Rare-Earth Nanoparticles with Enhanced Upconversion Emission and Suppressed Rare-Earth-Ion Leakage.* Chemistry - A European Journal, 2012. **18**(18): p. 5564.
36. Yin W, T.G., Ren W, Yan L, Jin S, Gu Z, Zhou L, Li J, Zhao Y, *Design of multifunctional alkali ion doped CaF2 upconversion nanoparticles for simultaneous bioimaging and therapy.* Dalton Transactions, 2014. **43**(10): p. 3870.
37. Zhou, J.C., et al., *Bioimaging and toxicity assessments of near-infrared upconversion luminescent NaYF4:Yb,Tm nanocrystals.* Biomaterials, 2011. **32**(34): p. 9059-9067.
38. Wang, X., et al., *One-Step Solvothermal Synthesis of Targetable Optomagnetic Upconversion Nanoparticles for in Vivo Bimodal Imaging.* Analytical Chemistry, 2013. **85**(21): p. 10225-10231.
39. Shan, S., et al., *Preparation and Biological Application of Rare Earth Upconversion Fluorescent Nanomaterials.* Progress in Biochemistry and Biophysics, 2013. **40**(10): p. 925-934.

40. Patra, A., et al., *Upconversion in Er3+: ZrO2 nanocrystals.* Journal of Physical Chemistry B, 2002. **106**(8): p. 1909-1912.
41. Patra, A., et al., *Blue upconversion emission of Tm3+-Yb3+ in ZrO2 nanocrystals: Role of Yb3+ ions.* Chemical Physics Letters, 2005. **407**(4-6): p. 477-481.
42. Speghini, A., et al., *Preparation, structural characterization, and luminescence properties of Eu3+-doped nanocrystalline ZrO2.* Journal of Materials Research, 2005. **20**(10): p. 2780-2791.
43. Gu, F., et al., *Effect of Dy3+ doping and calcination on the luminescence of ZrO2 nanoparticles.* Chemical Physics Letters, 2003. **380**(1-2): p. 185-189.
44. Chen, G.Y., et al., *Upconversion mechanism for two-color emission in rare-earth-ion-doped ZrO2 nanocrystals.* Physical Review B, 2007. **75**(19).
45. Salas, P., et al., *High temperature thermoluminescence induced on UV-irradiated tetragonal ZrO2 prepared by sol-gel.* Materials Letters, 2000. **45**(5): p. 241-245.
46. Stoia, M., P. Barvinschi, and F. Barvinschi, *Structural and morphologic characterization of zirconia-silica nanocomposites prepared by a modified sol-gel method.* Journal of Crystal Growth, 2014. **401**: p. 462-468.
47. Ghosh, P. and A. Patra, *Role of surface coating in ZrO2/Eu3+ nanocrystals.* Langmuir, 2006. **22**(14): p. 6321-6327.
48. Gomez, L.A., et al., *Upconversion in Er3+-doped ZrO2 nanocrystals pumped at 1.426 mu m.* Journal of Applied Physics, 2008. **103**(5): p. 4.
49. Martinez-Hernandez, A., et al., *Synthesis and cathodoluminescence characterization of ZrO2:Er3+ films.* Journal of Luminescence, 2014. **153**: p. 140-143.
50. Torabmostaedi, H., et al., *Process control for the synthesis of ZrO2 nanoparticles using FSP at high production rate.* Powder Technology, 2013. **246**: p. 419-433.
51. Romero, V.H., et al., *Brilliant blue, green and orange-red emission band on Tm(3+-), Tb(3+)- and Eu(3+)- doped ZrO(2) nanocrystals.* Journal of Physics D-Applied Physics, 2010. **43**(46).
52. Brunner, T.J., et al., *In Vitro Cytotoxicity of Oxide Nanoparticles: Comparison to Asbestos, Silica, and the Effect of Particle Solubility.* Environ. Sci. Technol., 2006. **40**(14): p. 4381.
53. Karunakaran, G., et al., *Impact of Nano and Bulk ZrO2, TiO2 Particles on Soil Nutrient Contents and PGPR.* Journal of Nanoscience and Nanotechnology, 2013. **- 13**(- 1): p. - 685.
54. S. Kanchana, D.S.H., *Zirconia a Bio-inert Implant Material.* IOSR Journal of Dental and Medical Sciences 2013. **12**(6): p. 66-67.
55. S. P. Chandini Sam, V.S.P.a.K.S.K., *Novel nontoxic nanopigments based on zirconia and rare earth mixed oxides.* Crystal Research and Technology, 2010. **45**(11): p. 1203.
56. Lopez-Luke, T., et al., *Solvent and surfactant effect on the self-assembly and luminescence properties of ZrO(2):Eu(3+) nanoparticles.* Applied Physics B-Lasers and Optics, 2011. **102**(3): p. 641-649.
57. Cordova-Martinez, W., et al., *Nanocrystalline tetragonal zirconium oxide stabilization at low temperatures by using rare earth ions: Sm3+ and Tb3+.* Optical Materials, 2002. **20**(4): p. 263-271.
58. Kim, B.-K., J.-W. Hahn, and K. Han, *Quantitative phase analysis in tetragonal-rich tetragonal/monoclinic two phase zirconia by Raman spectroscopy.* 1997. **- 16**(- 8).
59. Lopez-Luke, T., et al., *Enhancing the up-conversion emission of ZrO2 : Er3+ nanocrystals prepared by a micelle process.* Journal of Physical Chemistry C, 2007. **111**(45): p. 17110-17117.
60. Iko Hyppänen, J.H., Jouko Kankare, Mika Lastusaari, and Laura Pihlgren, *Upconversion Properties of Nanocrystalline ZrO2:Yb3+, Er3+ Phosphors.* Journal of Nanomaterials, 2007. **2007**: p. 8.
61. Deepak Rajput, L.C., Alexander Terekhov, Kathleen Lansford and William Hofmeister, *Silica coating of polymer nanowires produced via nanoimprint lithography from femtosecond laser machined templates* Nanotechnology 2012. **23**(10).

62. Qiang Zhang, J.L.a.Y.W., *A silica gel supported dual acidic ionic liquid: an efficient and recyclable heterogeneous catalyst for the one-pot synthesis of amidoalkyl naphthols.* Green Chemistry 2010. **12**(12): p. 2254.
63. Pu, J., et al., *Fabrication of novel graphene-fullerene hybrid lubricating films based on self-assembly for MEMS applications.* Chemical comunications, 2013. **50**(4): p. 469-71.
64. Xu, Y., et al., *A Fluorescent Sensor for Zinc Detection and Removal Based on Core-Shell Functionalized Fe3O4@SiO2 Nanoparticles.* Journal of Nanomaterials, 2013. **2013**: p. 7.
65. Bunaciu, A.A.B., Elena Aboul-Enein, Hassan Y. Elena Udristioiu, Gabriela Fleschin, Serban, *FT-IR Spectrophotometric Analysis of Ascorbic Acid and Biotin and their Pharmaceutical Formulations.* Analytical Letters, 2009. **42**(10): p. 1327.
66. G. A. Mahmud, O.S., R. A. Chapman, H. J. Stiegler, E. M. Vogel, and Y. J. Chabal, *A Comparative Study of Aminosilanes for the Application of Reproducible, Ultralow Detection of Biomolecules.* The Electrochemical Society, 2012. **MA2012-01**(45): p. 1630.
67. Li, Z., et al., *Modification of NaYF4:Yb,Er@SiO2 Nanoparticles with Gold Nanocrystals for Tunable Green-to-Red Upconversion Emissions.* J. Phys. Chem C, 2011. **115**(8): p. 3296.
68. Pan, B.F., et al., *Effects of carbon nanotubes on photoluminescence properties of quantum dots.* Journal of Physical Chemistry C, 2008. **112**(4): p. 939-944.
69. Lina, W., et al., *Surface Passivation of Carbon Nanoparticles with Branched Macromolecules Influences Near Infrared Bioimaging.* Theranostics, 2013. **3**(9): p. 677-686.
70. Solis, D., et al., *Surfactant effect on the upconversion emission and decay time of ZrO2:Yb-Er nanocrystals.* Journal of Luminescence, 2009. **129**(5): p. 449-455.
71. Lopez-Luke, T., et al., *Improving pure red upconversion emission of Co-doped Y2O3:Yb3+-Er3+ nanocrystals with a combination of sodium sulfide and surfactant Pluronic-F127.* Journal of Luminescence, 2014. **145**: p. 292-298.
72. Landes, C., et al., *Photoluminescence of CdSe Nanoparticles in the Presence of a Hole Acceptor: n-Butylamine.* J. Phys. Chem B, 2001. **105**(15): p. 2986.

CHAPTER 3

SYNTHESIS AND CHARACTERIZATION OF GOLD NANOPARTICLES AND THEIR BIOAPPLICATIONS

3.1 Introduction

It was in 1857 when Michael Faraday was fascinated by the colloidal gold, this was reported from the famous Bakerian Lecture to the Royal Society in London by the paper named "Experimental relations of gold (and other metals) to light" [148] and whose investigations was focused in examine the interaction of light with metal particles, besides the formation, nature and properties of this ruby gold. About 100 years later Turkevich et al [38, 39] used electron microscopy to disclose that the Faraday´s preparation methods to obtain colloidal gold produce particles with average sizes of approximately 6 nm. Nowadays Gold nanoparticles are widely used in many fields for their unique optical and physical properties, such as surface plasmon oscillations for labeling, imaging, and sensing.

Certainly, surface plasmon absorption is the most bewitching property of gold nanoparticles, which mainly is based on collective oscillation of a large number of free electrons in a continuous band structure and can be tuned by changing parameters such as particle size [149]. For example, for gold particles with sizes larger than the wavelength of the light, the frequency and bandwidth of surface plasmons can be quantitatively described with Mie theory [150] although particle size approaches the electron mean free path (~50 nm for gold), they can still be described with a modified Mie theory [149, 150]. Other structural parameters such as shape, aggregation, composition and roughness also significantly influence surface plasmons and related properties such as surface enhanced Raman scattering (SERS) and photo-thermal conversion [151-154]. There are many people that have studied these plasmonic properties of gold nanoparticles [155-158].

Gold nanoparticles (AuNPs) could be categorized by shape, size, and physical properties. The first achievement in the field of AuNPs was Au nanospheres, and then many other forms were obtained, such as nanorods, nanoshells, and nanocages. Other types of AuNPs were also produced with great surface enhanced Raman scattering properties, as SERS nanoparticles. The synthesis methods were continuously developed for many years. As result, the many simple synthetic protocols became available, and their sizes and shapes could be well controlled.

In colloidal gold or gold nanospheres the diameters could range from 2 nm to 100 nm, which could be synthesized by reducing aqueous $HAuCl_4$ solution with addition of various reducing agents under different parameters and conditions. Sodium citrate or sodium borohydride, are two of the most commonly used reducing agents, producing monodisperse Au nanospheres [39-42]. The size of nanospheres could also be controlled by changing the ratio of reducing agents and Au.

A powerful technique for early diagnosis of epithelial cancer is the Two-photon imaging (TPI), because it permits non-invasive imaging of subcellular components with the ability to penetrate tissues hundreds of microns [159-161]. Moreover morphological and fluorescence quantification from TPI of endogenous fluorophores could be helpful to compare cancerous and precancerous from normal tissue. Besides TPI has the capability to supervise a variety of biomolecular markers that are strongly indicative of cancer. By the use of this technique there is an extensive research of the use of traditional fluorophores [162] as well as new different luminescent contrast agents such as quantum dots [163] and metallic nanoparticles [164-167]. Although quantum dots have much larger two photon action cross section than organic fluorophores (>10 000 GM compared to 1-300 GM for organic fluorophores), they are highly toxic reducing their possible in vivo applications. However gold nanoparticles are biocompatible and could present a large two-photon action cross-section [168].

According to the first investigations of TPI, it was found that two-photon induced luminescence, which depends on excitation intensity, also could be seen from roughened surfaces [169] due to the resonant coupling of specific frequencies of light to surface plasmons. The serial process of two-photon luminescence implicate a sequential absorption of photons and emission from the recombination of electrons in the sp-band and holes in the d-band [170]. Nevertheless this process is different from two-photon excitation in fluorophores in which near simultaneous absorption of two coherent photons is needed. It has been reported that gold nanostructures present efficient single and two-photon induced luminescence [171, 172] and this is due to their ability to support surface plasmon resonances with low cushioning [166] besides their longitudinal plasmonic resonance tunable to near-infrared wavelengths that is helpful because biological tissues exhibit small extinction coefficients. These optical properties make gold nanoparticles an attractive contrast agent for biomedical imaging of highly scattered tissue. The use of gold nanoparticles can

expand the capabilities of TPI to allow noninvasive imaging of a variety of new molecular signatures. In this work gold nanoparticles were used as tissue stain,

In this work, we have used gold to stain HeLa cells and cervical tissue. The AuNPs have the property of two photon luminescence (TPL) and it could be obtained by exciting in NIR regions which is very important for *in vivo* applications due to the deep penetration and low damages that this wavelength present. When gold nanoparticles interact with biological samples the can be internalize or add to specific cell components by electrostatical charges or their functional groups that induce aggregation and then affords strong interaction with them. The amount of fluorophores that have visible emission by being excited in NIR wavelengths is low, besides of their problems of photo-bleaching and blinking REF. Having obtained the TPL emission of gold nanoparticles we found that they could be a well candidate for imaging because by using them we realize that the cell structure in cervical tissue can be well defined.

3.2 Experimental, Synthesis of Gold Nanoparticles

First the precursor solutions were prepared as follows: 0.1 M $HAuCl_4$ solution was prepared by adding 0.5 g of $HAuCl_4$ (Gold III Chloride Hydrate, 99.999% from sigma-aldrich) to 14.715 ml of deonized water from Quimicurt, this solution is protected from light and kept at room temperature. A sodium citrate solution was prepared by dissolving 0.0375 g of sodium citrate (from sigma-aldrich) in 3.75 ml of deonized water. 0.1 M $NaBH_4$ solution was prepared by adding 0.01135 g of $NaBH_4$ (from sigma-aldrich) to cold deonized water (at 4° C). Finally to prepare 0.04 M sodium citrate solution, 0.047 g of sodium citrate was added to 4 ml of deonized water at room temperature.

To obtain gold nanospheres (**AuNS**) the Turkevich Method was used, by mixing aqueous $HAuCl_4$ solution and sodium citrate as reducing agent, as follows. In 25 ml of boiling water, 250 µl of 0.1 M $HAuCl_4$ solution and 3.75 ml of 1%wt. sodium citrate solution were added respectively, under stirring (400 rpm). After a few minutes the solution turned ruby red, when this happened the solution was cooled down to room temperature. Finally colloid was filtered and kept in storage at 4° C, see figure 3.1. Moreover, to obtain gold nanostructures, not necessarily spheres, gold was

reduced with $NaBH_4$, this type of nanostructures were obtained by adding 200 of $HAuCl_4$ to the previously prepared 0.1 M $NaBH_4$ solution and then storage at 48 hrs and stabilized with the 0.04 M Sodium citrate solution, this type of nanoparticles were only used for Raman spectroscopy.

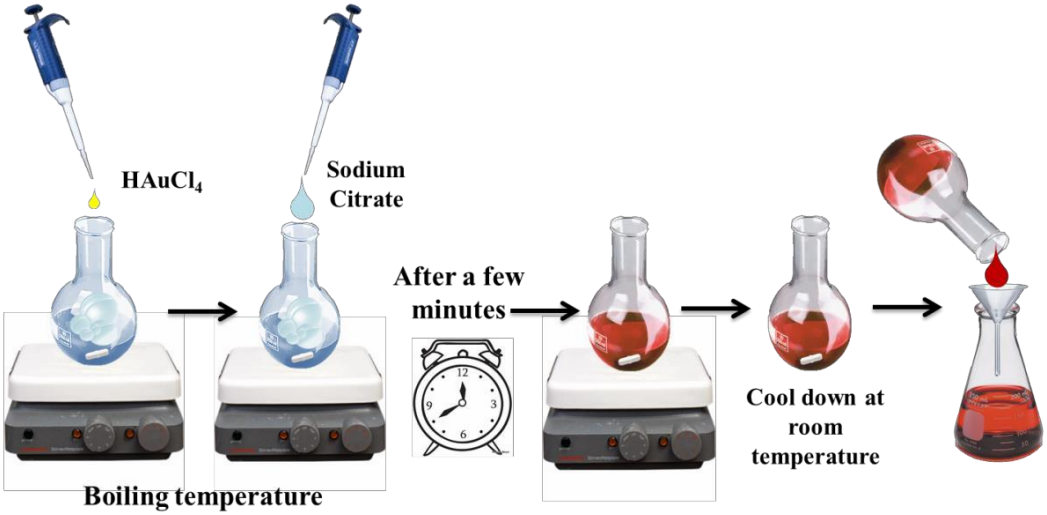

Figure 3.1 Diagram of gold nanospheres synthesis by following Turkevich method.

3.3 Preliminary work on gold nanoparticles and HeLa Cells

Gold Nanoparticles were prepared by following the previously mentioned Turkevich method, after that the colloidal gold was washed twice in a centrifuge at 13000 rpm for 20 min, the resulting colloidal gold was analized by DLS and Zeta Potential to have an estimation of size and superficial charge, resulting in the values of table 4.1 that shows the gold nanoparticles in water and table 4.2 for gold nanoparticles in two different quantities of Phosphate Buffer Solution (PBS).

Table 3.1 DLS and Zeta Potential of gold nanoparticles in water

Water	DLS (d/nm)	Zeta Potential (mV)
AuNP Soln 100%	63	-27.1
AuNP Soln 70%	29	-33.9
AuNP Soln 50%	31.42	-29.9
AuNP Soln 30%	38.58	-29.9
AuNP Soln 10%	40.06	-27.2

Table 3.2 DLS and Zeta Potential of gold nanoparticles in PBS

PBS	DLS (d/nm)	Zeta Potential (mV)
50%	650	-26
50%	1036	-24.7
50%	1427	-24.7
30%	640	-27
30%	724.6	-25.1
30%	733.6	-25

As it is observed when gold nanoparticles are in PBS are apparently more aggregated, probably due to the affinity of functional groups such as hydroxyls that are present in this buffere solution, after that the gold nanoparticles were incubated by different times with a molecule that has thiol and hydroxyl groups (SH-OH) and subsequently with amino-Poliethilenglycol (amino-PEG) this is because of the high affinity firstly between gold and thiol groups and secondly between hydroxyl and amino groups, three incubation times were tried (marked as Rx1, Rx2 and Rx3 respectively), having the following DLS and Zeta potential results, see table 4.3.

Table 3.3 Gold Nanoparticles incubated with a SH-OH molecule and amino-PEG

AuNP´s	**DLS (d/nm)**	**Zeta Potential (mV)**
AuNP-SH (Rx1) 30 hrs	33.31	-44.6
AuNP-SH (Rx1) 48 hrs	30.53	-34.5
AuNP-SH-PEG (Rx1) 15 hrs	31.69	-22.5
AuNP-SH-PEG (Rx1) 40 hrs	36.03	-23.1
AuNP-SH-PEG (Rx1) 48 hrs	40.25	-28.9
AuNP-New (Rx2)	55.66	-37.8
AuNP-SH (Rx2) 1 hrs	22.98	-42
AuNP-SH (Rx2) 24 hrs	28.21	-39.2
AuNP-SH (Rx2) 72 hrs	32.67	-21.1
AuNP-SH-PEG (Rx2) 15 hrs	56.45	-14.4
AuNP-SH-PEG (Rx2) 40 hrs	48.94	-17.9
AuNP-SH (Rx3) 20 hrs	72.92	-39.6
AuNP-SH-PEG (Rx3) 24 hrs	46.94	-25.8

Finally these gold nanoparticles were incubated and functionalized with Folic Acid for 48 hrs, and three different tests were conducted by using gold nanoparticles in different steps of functionalization. The first group consisted of single gold nanoparticles incubated for 12 hrs in HeLa Cells and with cell nucleus stained with NucBlue®; the second group were gold nanoparticles with SH-groups incubated for 12 hrs in HeLa cells and finally gold nanoparticles functionalzed with folic Acid were incubated by 12 hrs in HeLa cells, having the following results, see figure 3.3-3.4 respectively.

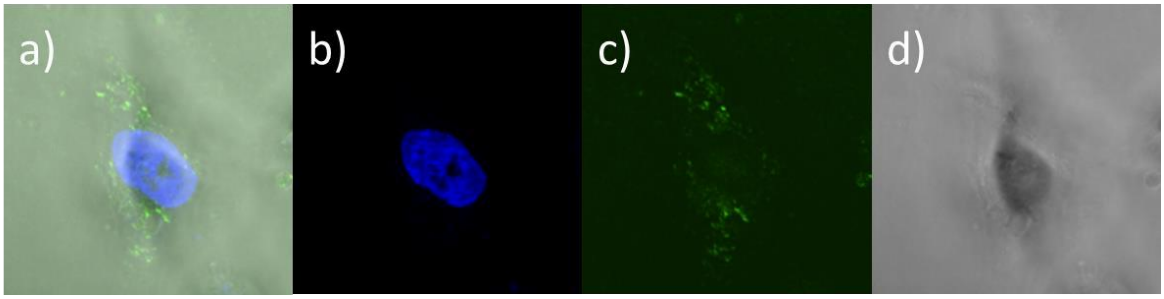

Figure 3.2 Single Gold nanoparticles incubated in HeLa cells for 12 hrs. The cell nucleus was stained with NucBlue®.

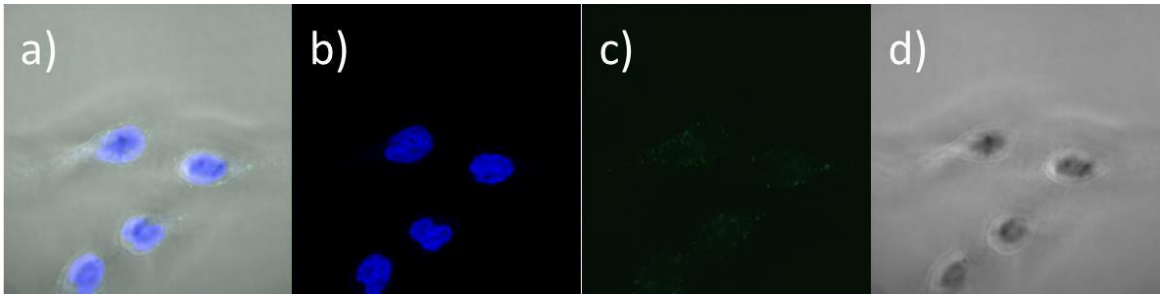

Figure 3.3 Gold nanoparticles funtionalized with SH-groups incubated in HeLa cells for 12 hrs. The cell nucleous was stained with NucBlue®.

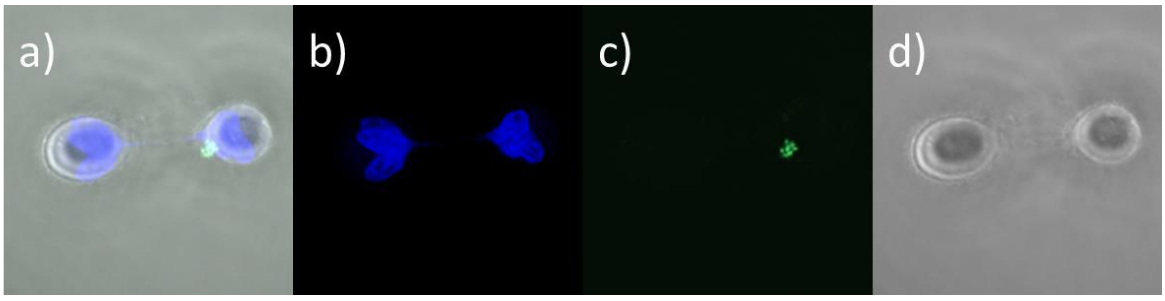

Figure 3.4 Gold nanoparticles funcionalized with Folic Acid incubated in HeLa cells for 12 hrs. The cell nucleous was stained with NucBlue®.

3.4 Gold Nanoparticles in Cervix Tissue

To prepare cervix tissue impregnated with gold nanoparticles, the histologic specimen embedded in paraffin, mounted on a glass microscope slide, is heated at 60° C during 1 hour. Then to deparaffinize, the mounted tissue was immersed in Xylene twice (15 minutes each) after that the tissue was rehydrated by using different concentrations of absolute EtOH as follows: EtOH 100% (10 minutes), EtOH 90% (10 minutes), EtOH 70% (10minutes) and EtOH 30% (10 minutes) followed by immersion in PBS 1X (5 minutes). Finally the sample was rinsed in distilled water (5 minutes).

To incubate the tissue the water excess was removed and the outline of the specimen marked (avoid making contact with the tissue) with and hydrophobic ink (Pap-pen®) before placing the histologic specimen in a Hot-bar and covering with the gold nanoparticles solution. The sample was incubated for 2 hours at 37° C being careful that the tissue was not dry; if it was required, more gold solution was added. At the end the tissue was carefully rinsed with distilled water, few drops of DABCO* were added, and covered with a coverslip making sure that no bubbles formed, see figure 3.5.

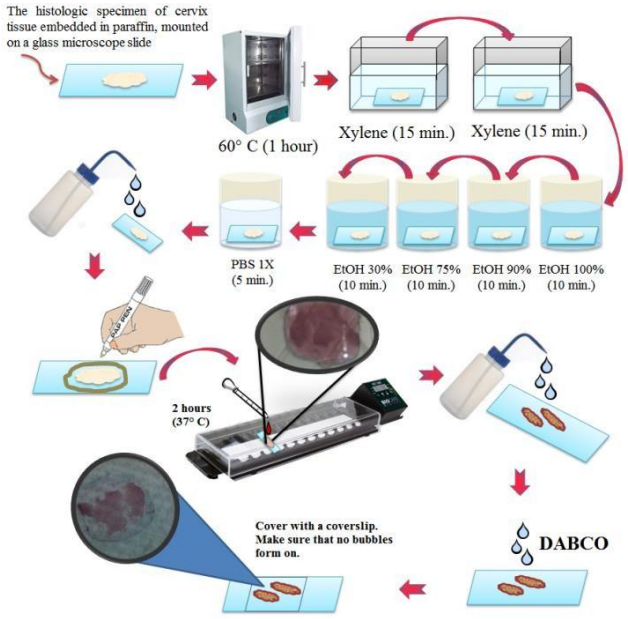

Figure 3.5 Schematic process of gold nanoparticles tissue marking.

3.5 Gold Nanoparticles and Cervix Tissue Characterization

The morphology and size of the AuNPs were analyzed by transmission electron microscopy (TEM) using a FEI Titan 800-300 with accelerating voltage set to 300 kV. UV-Vis absorption measurements were carried out using a Perkin Elmer Lamda 900 spectrometer with a spectral resolution of 2 nm. The optical characterization of cervix tissue was obtained by using a Confocal-Microscope Carl-Zeiss Model LSM-710-NLO at 543 nm and Two Photon Imaging (TPI) at 900 nm at 0.15 and 0.7 % of power. Raman mapping spectra were collected using a Renishaw Raman System (inVia Raman Microscope) with a 20× objective lens and the excitation laser was operated at 785 nm. The integration time for each Raman measurement was 20 s and the mapped area was 100x100 microns. For the Raman signal detection, the laser excitation light was directly focused onto the surface of the sample solution (250 µl) with a laser power of ~5mW and the aforementioned integration time.

3.6 Results and discussion

The size and morphological characterizations were performed by TEM images, and are shown in Figure 3.6(a), where it was confirmed that AuNPs were obtained with an overall outer diameter of ∼15 nm. Figure 3.6(b) shows the UV-Vis Spectrum of AuNP dispersed in aqueous solution. For AuNP, the Surface Plasmon Resonance (SPR) is centered at 520 nm which is consistent with the particle size and the color of AuNPs solution obtained with the Turkevich method [38].

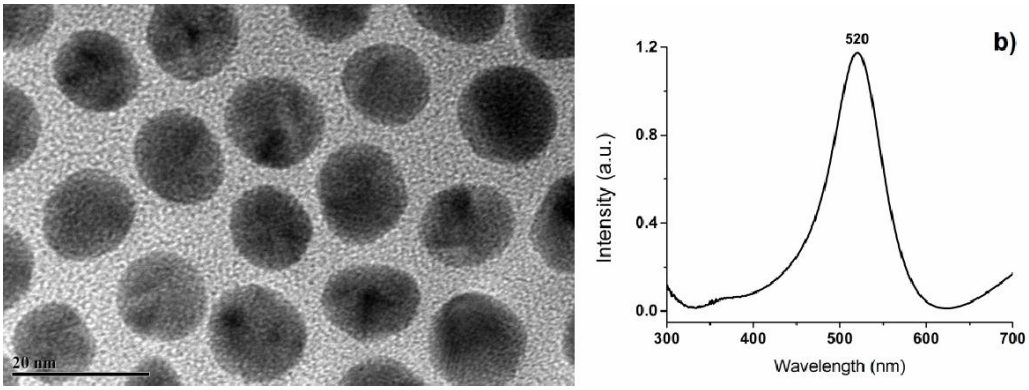

Figure 3.6 (a)TEM micrographs of gold nanoparticles (left). (b) UV-Vis spectra of spherical gold nanoparticles where SPR is situated at 520 nm (right).

Figure 3.7 shows the scanning electron microscopy images (SEM) of carcinogenic cervix cells incubated with gold nanoparticles, as we can corroborate gold nanoparticles are situated mostly in the nucleus of the cell, we propose that this is due to electrostatic charges, gold nanoparticles have negative charge in their surface and the nucleus has positively charged aminoacids, although the UV-Vis spectra shows a red-shifted band this is because of the nanoparticles agglomeration.

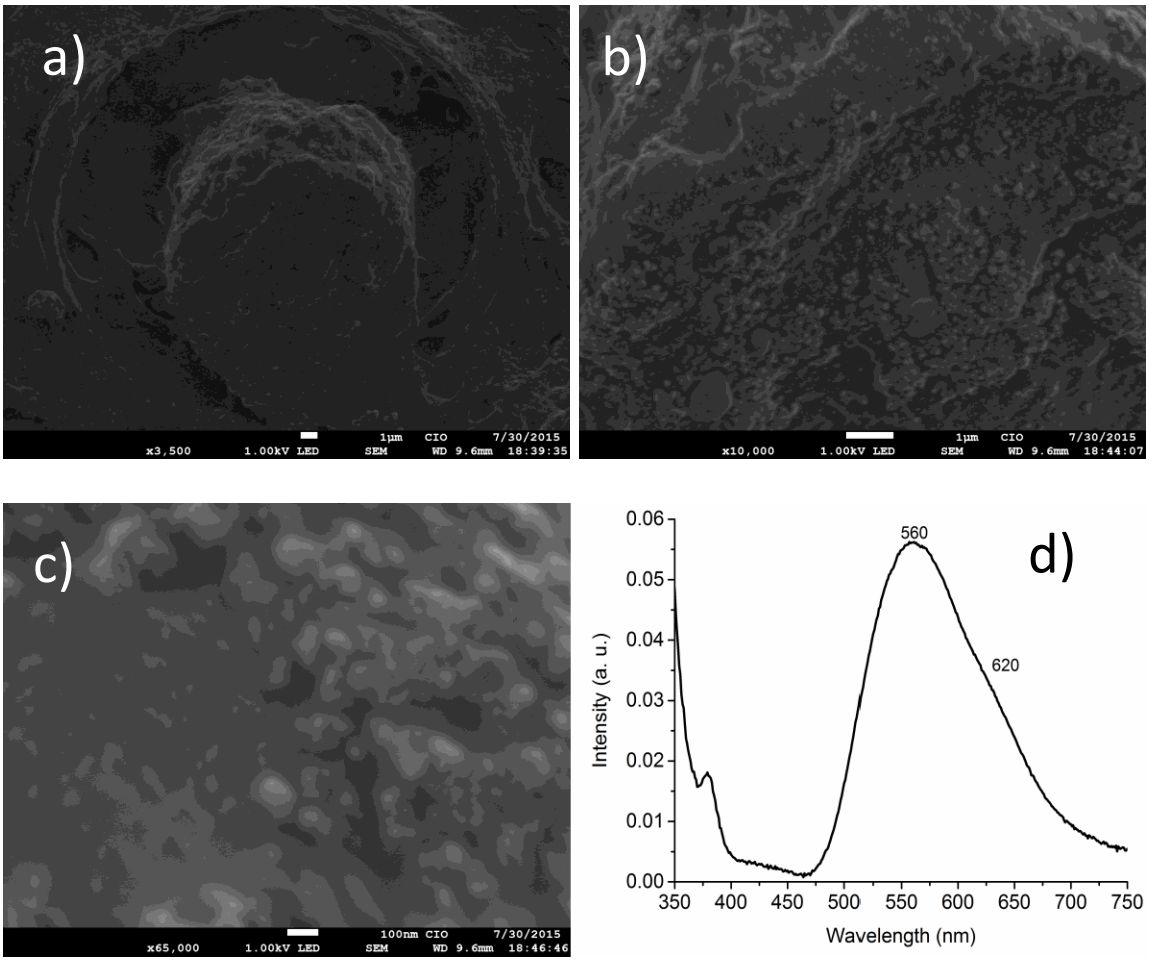

Figure 3.7 (a-c) SEM micrographs of a cell in a carcinogenic cervix tissue incubated with gold nanoparticles. (d) UV-Vis spectra of carcinogenic cervix tissue with gold nanoparticles.

In Figure 3.8 there is observed there are images of Dispersive X-ray Spectroscopy (EDS) mapping of the cells shown above, where it is corroborated that gold nanoparticles are situated in the nucleus surface. Moreover, the Energy of these cells displayed the elements that are present in the cells, see figure 3.9.

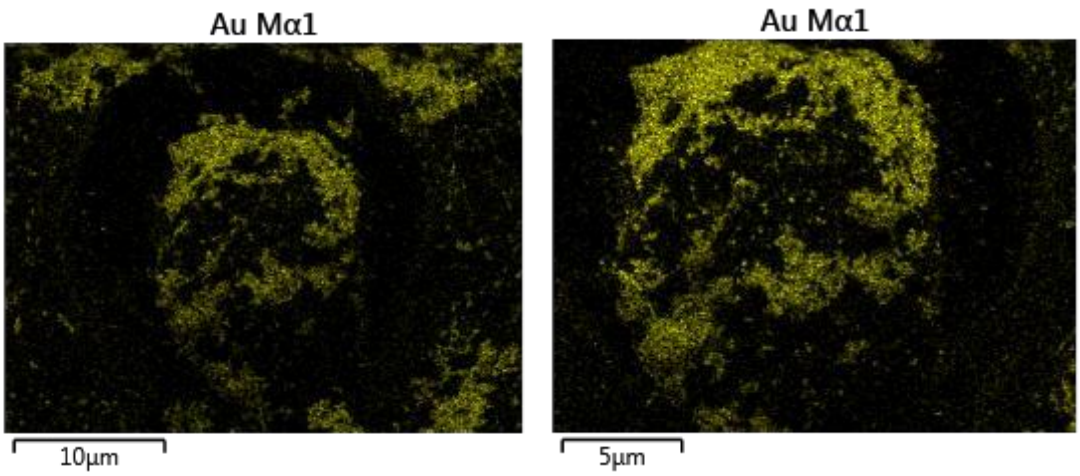

Figure 3.8 EDS map of a cell in a carcinogenic cérvix tissue with gold nanoparticles.

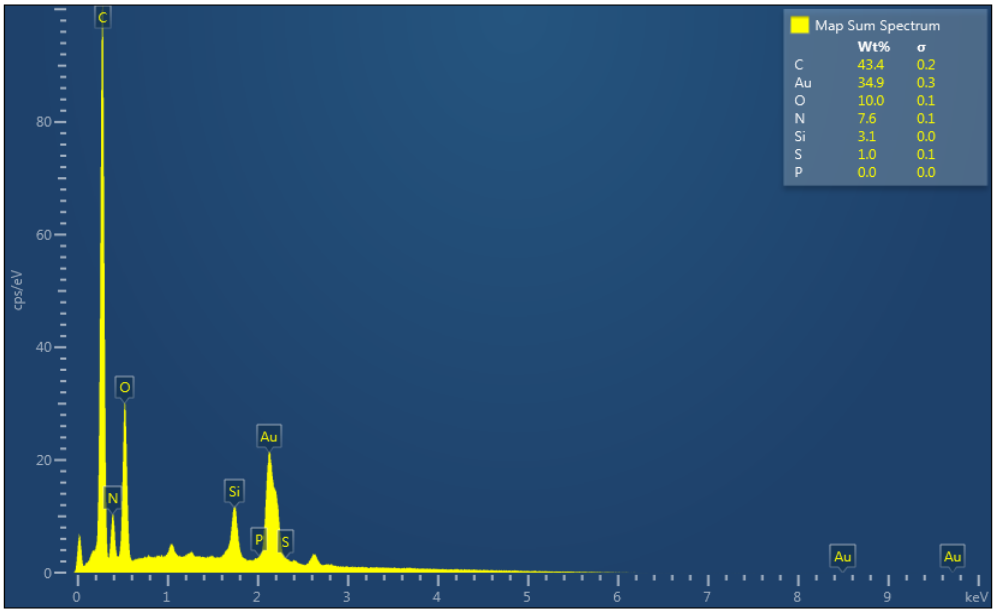

Figure 3.9 EDS spectra of a cell in a carcinogenic cérvix tissue with gold nanoparticles.

In figure 3.10 the SEM of cervix cells that have the presence of papilloma virus incubated with gold nanoparticles is observed, gold nanoparticles are situated principally on the nucleous surface of the cell, and again considering the fact that this is due to the surface charges, gold nanoparticles have negative charge in their surface and the nucleous that has aminoacids positively charged. In addition, in Figure 3.11 the mapping of the cells shown above is displayed, where it is corroborated that gold nanoparticles are situated on the nucleus. Moreover, the EDS of these cells displayed the elements that are present in there, see figure 3.12.

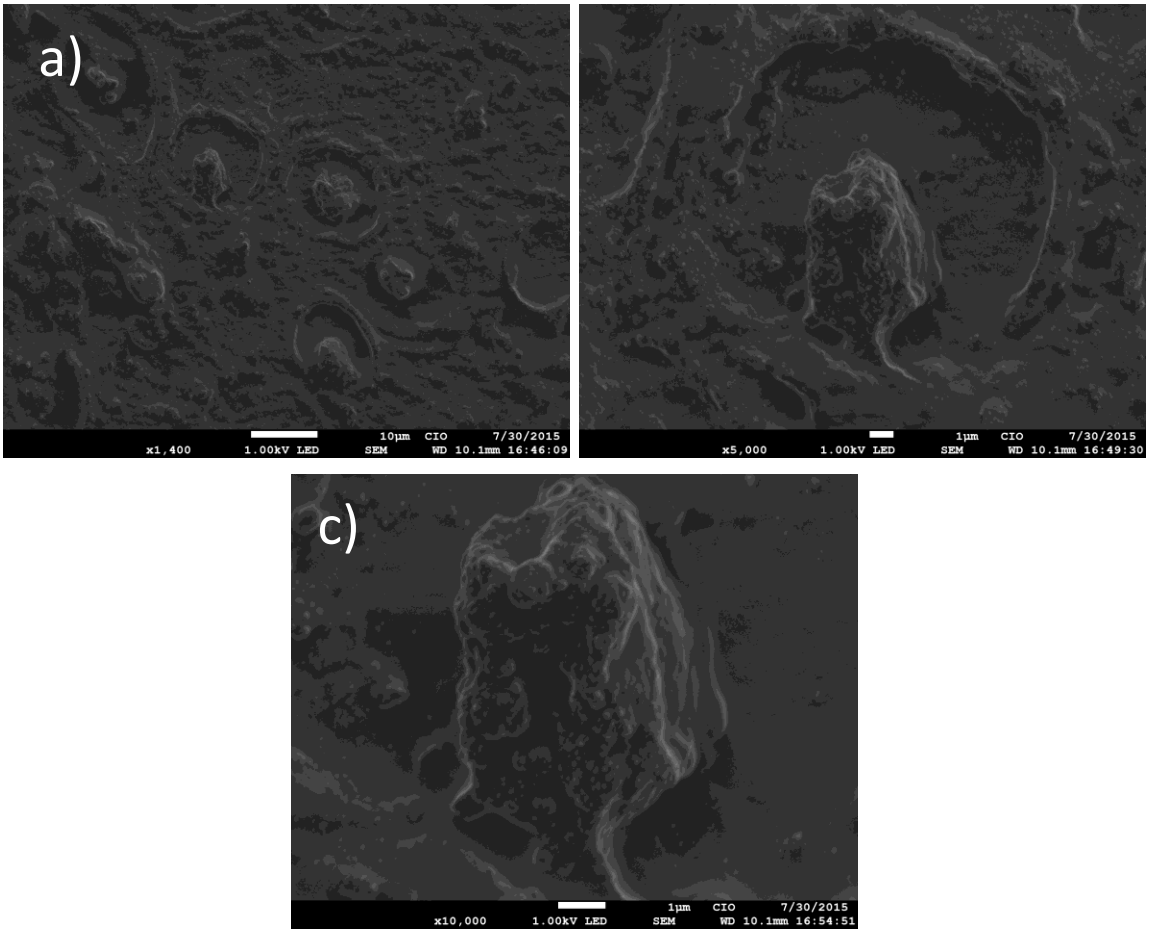

Figure 3.10 SEM micrographs of a cell in cervix tissue infected with papilloma virus and incubated with gold nanoparticles (a-c).

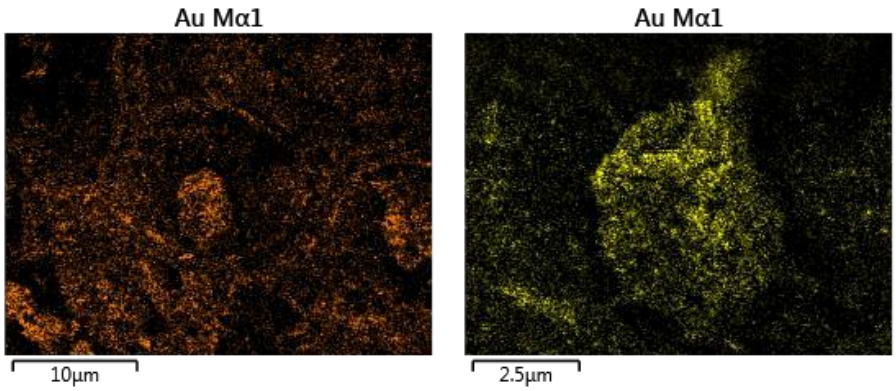

Figure 3.11 EDS maps of a cell in cervix tissue infected with papilloma virus and incubated with gold nanoparticles.

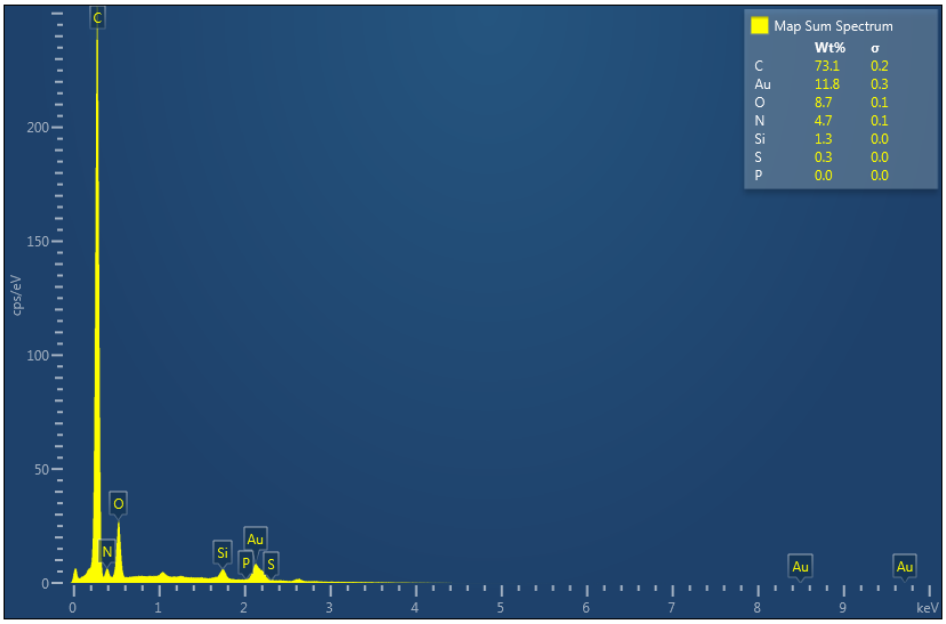

Figure 3.12 EDS spectra of a cell in cervix tissue infected with papilloma virus and incubated with gold nanoparticles.

Figure 3.13 presents confocal and two-photon images of cervix tissue incubated with gold nanoparticles using the 543 and 900 nm as excitation wavelengths, respectively. The images show successful structural marking, well images of cellular distribution, and brightness after being incubated with gold nanoparticles. The unlabeled cells show a relatively uniform distribution of two photon fluorescence signal throughout the nucleous. No signal is associated with the cytoplasm, which does not have significant concentration of gold nanoparticles that can be excited in the NIR region. The discrete bright spots in the nucleous of nanoparticle-labeled cells are indicative of uptake aminoacid labeled with nanoparticles inside cells. Two Photon Luminescence (TPL) images of cells treated with nonspecifically conjugated nanoparticles (Figure 3.13) show agglomeration of contrast agent and little attachment to the cytoplasm.

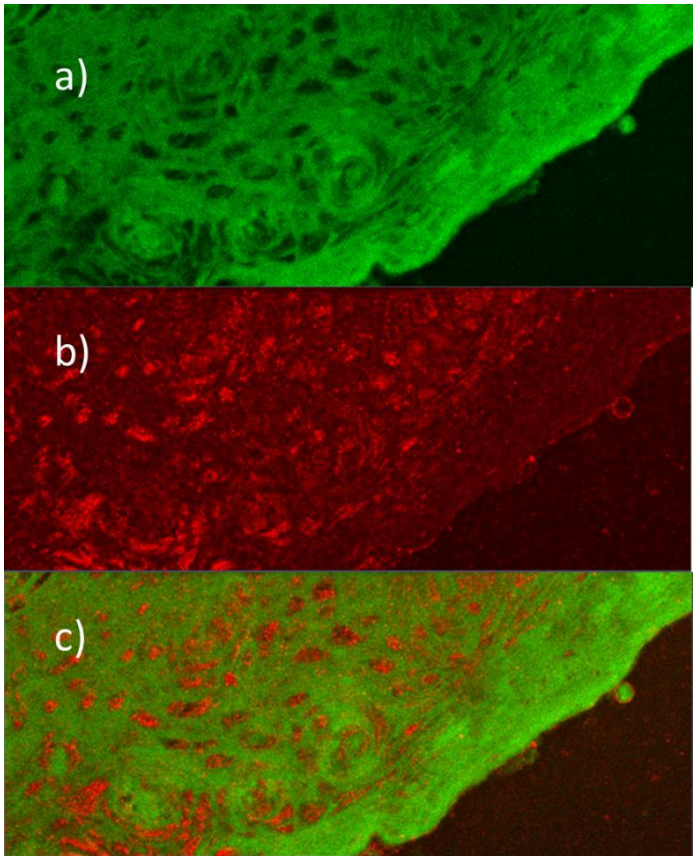

Figure 3.13 Micrographs of cervical tissue, a) auto-fluorescence with excitation at 543 nm, b) two-photon fluorescence excited at 900 nm. c) Overlapping of the (a) and (b) figures

By tuning the excitation wavelength from 800 to 1100 nm, it was found that 900 nm yielded the brightest TPL signal from the nanoparticles as well as the brightest signal from the cancer cells. This wavelength corresponds to the longitudinal plasmon resonance frequency of the nanoparticles.

Two-photon-induced luminescence from the gold nanoparticles was verified by measuring the dependence of the emission intensity on the excitation power. The deposited gold nanoparticles in cervical tissue at different emission regions were examined. A linear dependence of the incident power was observed for increasing excitation powers from 0.5 to 0.7 %, indicating that the excitation is a two-photon process (Figure 3.14 and figure 3.15)

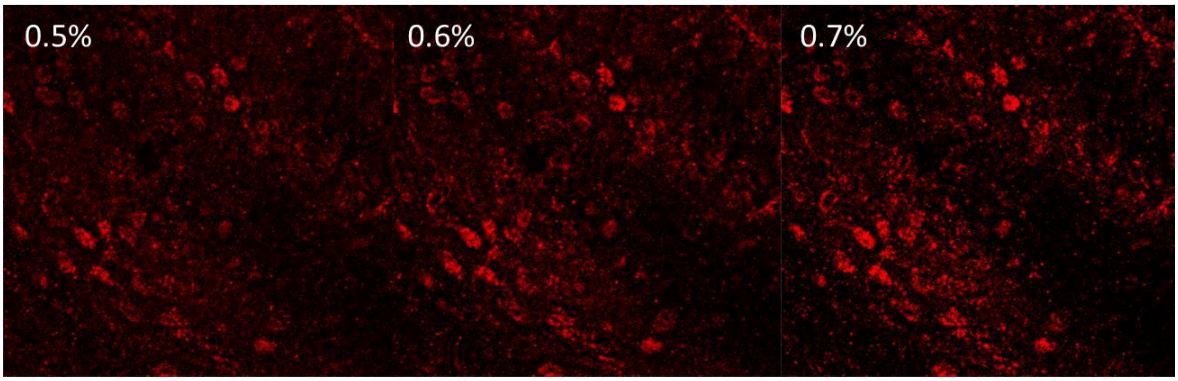

Figure 3.14 Emission intensity dependence of gold nanoparticles on different excitation power at 900 nm varying the power percent from 0.5 to 0.7 respectively.

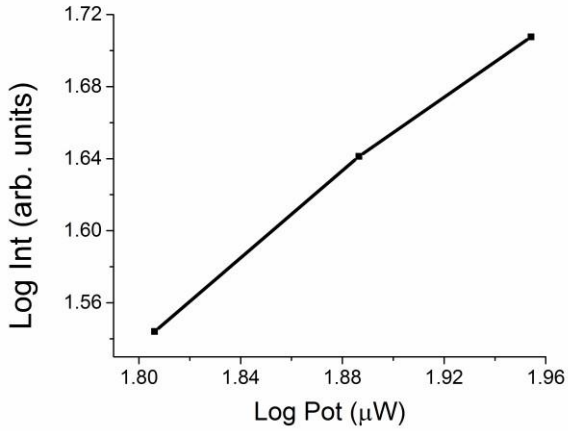

Figure 3.15 Linear dependence of incident power and intensity.

Figure 3.16 shows two different SERS spectra of cervical tissue, one of them only presents Human Papiloma Virus (HPV) and the other one present carcinoma, here it is observed the differences between the main peaks that are characteristic of this type of samples are observed the bands at 967, 1089, 1228, 1253, 1340 and 1456 cm^{-1} are typical of cervical tissue as it has been reported The ratio of intensities at 1454 to 1656 cm^{-1} was greater for squamous dysplasia than all other tissue types, while the ratio of intensities at 1330 to 1454 cm^{-1} was lower for samples with squamous dysplasia than all other tissue types [173].

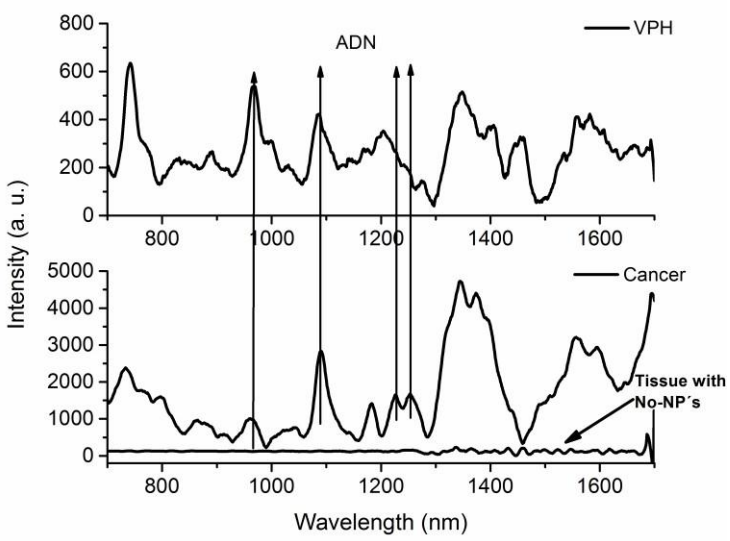

Figure 3.16 SERS spectra of two different cervical tissue with gold nanoparticles, one with HPV damage and the other one with carcinoma, analized at 789 nm. In this figure it is also observed the Raman spectra when the tissue is analized without the presence of gold nanoparticles and no-peaks are present.

Moreover, when the tissue samples were analized by Raman spectroscopy it was observed that a laser ablation was presented and as it is well known AuNPs have been shown to be an ideal agent for enhancing laser-based ablation therapies mostly because of their tunable optical properties and surface plasmon resonance (SPR) effect [174-176]. In figure 2.13 we can observe damage caused due to the presence of gold nanoparticles, when cervical tissue was analized by Raman spectroscopy at 785 nm, and as we can assume that the presence of gold favor the photothermal effect causing burning of the tissue. As we know the characteristic resonant frequency for SPR strongly depends on AuNPs size, shape, interparticle interactions, dielectric properties, and local environment [177]. As examples, an increase of the particle size induces a redshift in the SPR, while it has been calculated that clustered aggregates of several nanoparticles can manifest wide broadening of the peaks in the absorption spectrum [178, 179]. Finally photothermal therapy is a promising method for the localized ablation of malignant tissues that are difficult to remove by surgery [175, 176, 180, 181]. Distinct energy sources have been used to provoke the thermal ablation of biological samples including laser-based techniques [175] for instance, laser induced thermal therapies are used for treating cardiac arrhythmias, prostate cancer and varicose veins [182].

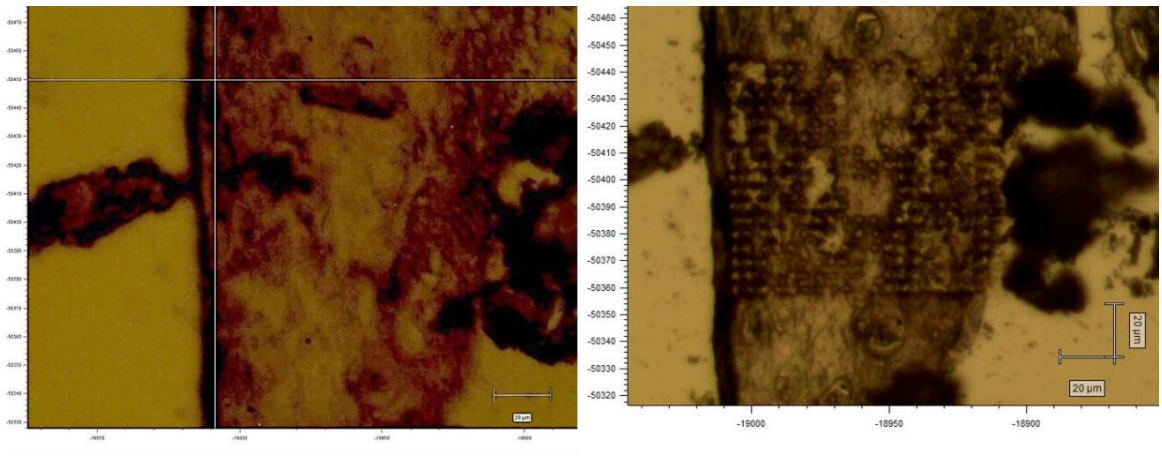

Figure 3.17 Micrographs of cervix tissue with gold nanoparticles before and after mapping with a laser of 785 nm.

3.7 Conclusion

We have demonstrated the effective use of gold nanoparticles as bright contrast agents for TPL imaging. Two-photon-induced luminescence from the gold nanoparticles was verified by measuring the dependence of the emission intensity on the excitation power. Gold nanoparticles were deposited on a cervix tissue. We have demonstrated the effective use of gold nanoparticles as bright contrast agents for TPL imaging. By staining cervical tissue the cell nucleus imaging could be carried out with very high signal-to-noise ratios. In cases where imaging depths will be limited by the maximum available power that can be delivered to the imaging plane without causing damage to tissue, gold nanoparticles might provide sufficient brightness to extend the maximum depth of imaging. Additionally, we have shown that the use of gold nanoparticles can expand the capabilities of TPI to allow noninvasive imaging of biological samples.

3.8 References

1. Faraday, M., *The Bakerian Lecture: Experimental Relations of Gold (and Other Metals) to Light.* The Royal Society, 1857. **Vol. 147** p. 145-181.
2. Turkevich, J., G. Garton, and P.C. Stevenson, *The color of colloidal gold.* Journal of Colloid Science, 1954. **9, Supplement 1**(0): p. 26-35.
3. Turkevich, J., P.C. Stevenson, and J. Hillier, *The Formation of Colloidal Gold.* The Journal of Physical Chemistry, 1953. **57**(7): p. 670-673.
4. Ashcroft, N.W. and N.D. Mermin, *Solid State Physics*. HRW international editions. 1976: Holt, Rinehart and Winston.
5. Kreibig, U. and M. Vollmer, *Optical properties of metal clusters*. Springer series in materials science. 1995: Springer.
6. Caruso, F., R.A. Caruso, and H. Mohwald, *Nanoengineering of inorganic and hybrid hollow spheres by colloidal templating.* Science, 1998. **282**(5391): p. 1111-1114.
7. Jain, P.K., et al., *Noble Metals on the Nanoscale: Optical and Photothermal Properties and Some Applications in Imaging, Sensing, Biology, and Medicine.* Accounts of Chemical Research, 2008. **41**(12): p. 1578-1586.
8. Scher, E.C., L. Manna, and A.P. Alivisatos, *Shape control and applications of nanocrystals.* Philosophical Transactions of the Royal Society of London Series a-Mathematical Physical and Engineering Sciences, 2003. **361**(1803): p. 241-255.
9. Sun, Y.G. and Y.N. Xia, *Shape-controlled synthesis of gold and silver nanoparticles.* Science, 2002. **298**(5601): p. 2176-2179.
10. Grzelczak, M., et al., *Shape control in gold nanoparticle synthesis.* Chemical Society Reviews, 2008. **37**(9): p. 1783-1791.
11. Hu, M., et al., *Gold nanostructures: engineering their plasmonic properties for biomedical applications.* Chemical Society Reviews, 2006. **35**(11): p. 1084-1094.
12. Huang, X., et al., *Gold nanoparticles: interesting optical properties and recent applications in cancer diagnostic and therapy.* Nanomedicine, 2007. **2**(5): p. 681-693.
13. Jain, P.K., et al., *Review of some interesting surface plasmon resonance-enhanced properties of noble metal nanoparticles and their applications to biosystems.* Plasmonics, 2007. **2**(3): p. 107-118.
14. Frens, G., *Controlled Nucleation for the Regulation of the Particle Size in Monodisperse Gold Suspensions.* Nature Physical Science 1973. **241**: p. 20-22.
15. Brust, M., et al., *SYNTHESIS OF THIOL-DERIVATIZED GOLD NANOPARTICLES IN A 2-PHASE LIQUID-LIQUID SYSTEM.* Journal of the Chemical Society-Chemical Communications, 1994(7): p. 801-802.
16. Martin, M.N., et al., *Charged Gold Nanoparticles in Non-Polar Solvents: 10-min Synthesis and 2D Self-Assembly.* Langmuir, 2010. **26**(10): p. 7410-7417.
17. Konig, K. and I. Riemann, *High-resolution multiphoton tomography of human skin with subcellular spatial resolution and picosecond time resolution.* Journal of Biomedical Optics, 2003. **8**(3): p. 432-439.
18. Masters, B.R., P.T.C. So, and E. Gratton, *Multiphoton excitation microscopy of in vivo human skin - Functional and morphological optical biopsy based on three-dimensional imaging, lifetime measurements and fluorescence spectroscopy,* in *Advances in Optical Biopsy and Optical Mammography*, R.R. Alfano, Editor. 1998. p. 58-67.
19. Zipfel, W.R., et al., *Live tissue intrinsic emission microscopy using multiphoton-excited native fluorescence and second harmonic generation.* Proceedings of the National Academy of Sciences of the United States of America, 2003. **100**(12): p. 7075-7080.
20. Albota, M., et al., *Design of organic molecules with large two-photon absorption cross sections.* Science, 1998. **281**(5383): p. 1653-1656.

21. Larson, D.R., et al., *Water-soluble quantum dots for multiphoton fluorescence imaging in vivo.* Science, 2003. **300**(5624): p. 1434-1436.
22. Farrer, R.A., et al., *Highly efficient multiphoton-absorption-induced luminescence from gold nanoparticles.* Nano Letters, 2005. **5**(6): p. 1139-1142.
23. Huang, X.H., et al., *Cancer cell imaging and photothermal therapy in the near-infrared region by using gold nanorods.* Journal of the American Chemical Society, 2006. **128**(6): p. 2115-2120.
24. Sonnichsen, C. and A.P. Alivisatos, *Gold nanorods as novel nonbleaching plasmon-based orientation sensors for polarized single-particle microscopy.* Nano Letters, 2005. **5**(2): p. 301-304.
25. Yelin, D., et al., *Multiphoton plasmon-resonance microscopy.* Optics Express, 2003. **11**(12): p. 1385-1391.
26. *Light-Responsive Nanostructured Systems for Applications in Nanomedicine*, in *Light-Responsive Nanostructured Systems for Applications in Nanomedicine*, S. Sortino, Editor. 2016, Springer Int Publishing Ag: Cham. p. 1-263.
27. Boyd, G.T., Z.H. Yu, and Y.R. Shen, *PHOTOINDUCED LUMINESCENCE FROM THE NOBLE-METALS AND ITS ENHANCEMENT ON ROUGHENED SURFACES.* Physical Review B, 1986. **33**(12): p. 7923-7936.
28. Imura, K., T. Nagahara, and H. Okamoto, *Near-field two-photon-induced photoluminescence from single gold nanorods and imaging of plasmon modes.* Journal of Physical Chemistry B, 2005. **109**(27): p. 13214-13220.
29. Mohamed, M.B., et al., *The 'lightning' gold nanorods: fluorescence enhancement of over a million compared to the gold metal.* Chemical Physics Letters, 2000. **317**(6): p. 517-523.
30. Wang, H.F., et al., *In vitro and in vivo two-photon luminescence imaging of single gold nanorods.* Proceedings of the National Academy of Sciences of the United States of America, 2005. **102**(44): p. 15752-15756.
31. Movasaghi, Z., S. Rehman, and I.U. Rehman, *Raman spectroscopy of biological tissues.* Applied Spectroscopy Reviews, 2007. **42**(5): p. 493-541.
32. Almeida, J.P.M., E.R. Figueroa, and R.A. Drezek, *Gold nanoparticle mediated cancer immunotherapy.* Nanomedicine-Nanotechnology Biology and Medicine, 2014. **10**(3): p. 503-514.
33. Hirsch, L.R., et al., *Metal nanoshells.* Annals of Biomedical Engineering, 2006. **34**(1): p. 15-22.
34. Hirsch, L.R., et al., *Nanoshell-mediated near-infrared thermal therapy of tumors under magnetic resonance guidance.* Proceedings of the National Academy of Sciences of the United States of America, 2003. **100**(23): p. 13549-13554.
35. Kennedy, L.C., et al., *A New Era for Cancer Treatment: Gold-Nanoparticle-Mediated Thermal Therapies.* Small, 2011. **7**(2): p. 169-183.
36. Khlebtsov, B., et al., *Optical amplification of photothermal therapy with gold nanoparticles and nanoclusters.* Nanotechnology, 2006. **17**(20): p. 5167-5179.
37. Iodice, C., et al., *Enhancing photothermal cancer therapy by clustering gold nanoparticles into spherical polymeric nanoconstructs.* Optics and Lasers in Engineering, 2016. **76**: p. 74-81.
38. Choi, W.I., et al., *Photothermal Cancer Therapy and Imaging Based on Gold Nanorods.* Annals of Biomedical Engineering, 2012. **40**(2): p. 534-546.
39. Young, J.K., E.R. Figueroa, and R.A. Drezek, *Tunable Nanostructures as Photothermal Theranostic Agents.* Annals of Biomedical Engineering, 2012. **40**(2): p. 438-459.
40. Wenger, H., et al., *Laser ablation as focal therapy for prostate cancer.* Current Opinion in Urology, 2014. **24**(3): p. 236-240.

CHAPTER 4

MULTI-BRANCHED GOLD NANOSTRUCTURES CHARACTERIZATION AND THEIR USE FOR SERS DETECTION

4.1 Introduction

4.2 Synthesis of Multi-branched Gold Nanostructures

4.3 Characterization

4.4 SERS properties by using Rhodamine B and α-Glucose as selected probes

4.5 Results

4.6 Discussion

4.7 Conclusion

4.8 References

4.1 Introduction

The detection of molecules at low concentration in solution with high sensitivity and specificity has been of great interest in fields such as biomedical research and diagnosis [183-186]. In particular, surface-enhanced Raman scattering (SERS) is a powerful, ultrasensitive, and non-destructive spectroscopic technique that can detect analytes down to the single molecule level while simultaneously providing molecular specific information [187-189]. Many studies have demonstrated enhancement factors of 10^5 or higher, leading to Raman signals that are comparable to or even higher than those of the fluorescent organic dyes [190-192]. SERS is a technique resulting in strongly increased Raman signals of molecules at or near metal nanostructures, typically noble metals such as gold and silver. In particular, SERS has been exploited to detect low concentration of biological samples such as different types of cancers [193-198], Alzheimer's disease (β-amyloid peptide) [199, 200], the hepatitis C virus [201], and Parkinson's disease (dopamine depletion) [202, 203]. In the study of SERS processes, it is generally accepted that electromagnetic enhancement [204] and chemical enhancement [205] mechanisms are the principal phenomena involved in the amplification of Raman signals. Effective SERS depends on absorption of incident light by the metal nanostructures based on their surface plasmon resonance (SPR) [204] where the excitation wavelength is resonant with the metal-molecule charge transfer electronic states [205]. The success of SERS is highly dependent on the interaction between adsorbed molecules and the surface of plasmonic nanostructures. In the last years, many studies have strived to optimize substrate structure and configuration to maximize enhancement factors such as new plasmonic materials [206-208] with different shapes and sizes [209, 210] that support increased SERS enhancement. The SPR of a metal nanoparticle may be tuned throughout visible and near-infrared (NIR) wavelengths by varying the size and shape or the aspect ratio [211-214]. Particularly, the plasmons of metallic nanostars, nanoshells, and nanorods can be used to tune the SPR into the NIR region [215-221], which is desired for *in vivo* biomedical applications due to deeper tissue penetration [222-224].

Gold nanoparticles have been widely studied for bio detection applications due to their unique optoelectronic properties. Various types of AuNPs [225-228], both in aqueous [229-231] and organic solutions [41, 232], have been developed to serve as excellent SERS substrates. Moreover, the silanization of various metal nanoparticle systems has shown great success in protecting their

surface characteristics and facilitating bioconjugation [233, 234]. The SERS activity of gold and silver nanostructures has been experimentally verified using Rhodamine B as an analyte due to its distinct Raman features and adsorbability onto nanoparticles [235, 236].

One of the important applications of SERS is detection of glucose. Glucose in particular is interesting as proper monitoring of diabetes mellitus requires effective screening of glucose levels within human blood. Several studies have been reported previously [237-240]. Van Duyne and coworkers have done extensive work on SERS detection of glucose [241-243] in which they observed that SERS was successful in the detection of glucose at physiological concentrations using *in vitro* and *in vivo* sensing techniques. Yang and coworkers proposed the use of a photonic crystal fiber as a container of a different concentration solutions of D-glucose, and obtained a low concentration detection *via* Raman spectroscopy [244]. Dinish *et al*. implemented a nanogap SERS substrate with a deep-UV lithography technique for glucose sensing [245]. Very recently, Al-Ogaidi worked with gold nanostar@silica core–shell nanoparticles conjugated with glucose oxidase (GOx) enzyme molecules developed as the SERS biosensor for label-free detection of glucose, by examining SERS peak of H_2O_2 [246]. However, it is still challenging to achieve high reproducibility, good uniformity, and long-term stability of SERS substrates. As mentioned, glucose is extremely difficult to detect through conventional SERS methodologies because of its small Raman cross-section and weak absorption to bare metal surfaces.

In the present work, we have carried out a systematic study of the SERS signals of Rhodamine B (RB) and α-glucose adsorbed on colloidal multi-branched gold nanostructures (MBGNs) and MBGNs with a silica coating. The MBGNs demonstrated their ability to detect these two molecules at low concentrations, compared to AuNPs where no Raman signal was observed. While MBGNs serve to enhance the Raman signal, the MBGNs-silica coating induce aggregation and then affords strong interaction with RB and α-glucose resulting in an increase of hot spot density that improve the SERS signal. Since SERS detection of α-glucose in water is generally challenging, the successful detection within a clinically relevant concentration range shows the promise of the MBGNs and MBGNs-silica as potential SERS substrates for detecting molecules that strongly interact with silica coating or MBGN surface itself.

4.2 Synthesis of Multi-branched Gold Nanostructures

4.2.1 Materials

All chemicals were reagent grade. $HAuCl_4$, sodium citrate, silver nitrate, ascorbic acid, 3-aminopropyltriethoxysilane (APTES), Rhodamine B and α-glucose were purchased from Sigma-Aldrich. HCl was purchased from Karal, (~38% in H_2O), deionized water was purchased from Quimicurt, and ethanol was purchased from Jalmek.

4.2.2 Preparation of MBGNs and MBGNs-silica

Multi-branched gold nanostructure were prepared by a seed-mediated growth method following previously reported protocols with some modifications [247] where a gold seed solution was synthesized using the Turkevich method [231]. Briefly, the addition of a 1% citrate solution to a boiling solution of 1 mM $HAuCl_4$ under stirring yielded a red color characteristic of gold nanospheres (AuNP). The stable particles were filtered by Whatman filter papers of 110 nm, and then kept at 4 °C for long-term storage. To synthesize MBGNs, the solutions that are involve are a 0.5 mM $HAuCl_4$ solution, a 1M HCl solution, the gold seed solution prepared by the Turkevich method, a 0.01M silver nitrate solution and a 0.1 M ascorbic acid solution. At first there was an extended study to optimize the amount of reactants to obtain the best results in nanostructure morphologies resulting in a SPR red shifting, at the beginning the Silver nitrate was varied, as is indicated in table 4.1. It is believed that the major role of Ag^+ is to assist the anisotropic growth of Au branches on certain crystallographic facets on multi-twinned citrate seeds [248-251].

Table 4.1 Quantities of reactants, varying the amount of $AgNO_3$ solution to obtain multi-branched nanostructures

Sample	$HAuCl_4$ (µl)	HCl (µl)	Gold seeds (µl)	$AgNO_3$ (µl)	Ascorbic Acid (µl)
1_Ag5	25	10	100	5	63
2_Ag10	25	10	100	10	63
3_Ag15	25	10	100	15	63
4_Ag20	25	10	100	20	63
5_Ag30	25	10	100	30	63

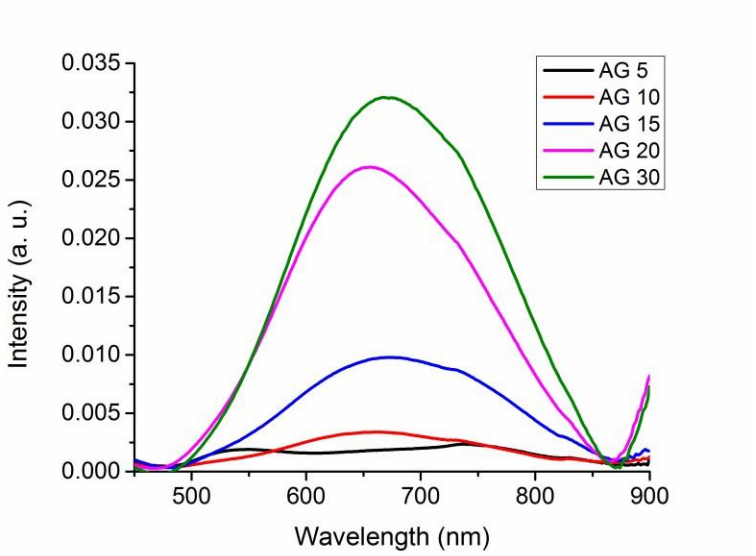

Figure 4.1 UV-Vis spectra of multi-branched gold nanostructures obtained by varying the amount of Silver Nitrate.

After that, the best results, using the red shifting in SPR as criterion, were given by the samples prepared with 15 and 30 µl of silver nitrate solution. After this, then the amount of HCl was varied as indicated in table 4.2.

Table 4.2 Quantities of reactants, varying the amount of HCl solution for the obtain of multi-branched nanostructures

Sample	$HAuCl_4$ (µl)	HCl (µl)	Gold seeds (µl)	$AgNO_3$ (µl)	Ascorbic Acid (µl)
1_HCl_15	25	15	100	30	63
2_HCl_20	25	20	100	30	63
3_HCl_30	25	30	100	30	63
4_HCl_40	25	40	100	30	63

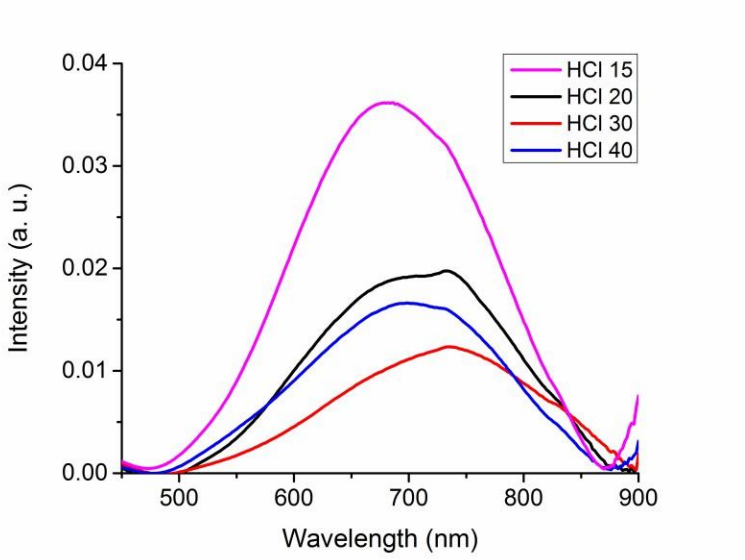

Figure 4.2 UV-Vis spectra of Multibrached Gold nanostructures obtained by varying the amount of HCl.

Our best result, by the SPR red shifting, was by using 20 µl of HCl solution. Finally the amount of $HAuCl_4$ solution was varied as shown in table 4.3.

Table 4.3 Quantities of reactants, varying the amount of $HAuCl_4$ solution for obtain multi-branched nanostructures

Sample	$HAuCl_4$ (µl)	HCl (µl)	Gold seeds (µl)	$AgNO_3$ (µl)	Ascorbic Acid (µl)
Au35Ag20	35	20	100	20	63
Au40Ag20	40	20	100	20	63
Au45Ag20	45	20	100	20	63
Au35Ag30	35	20	100	30	63
Au35Ag30	40	20	100	30	63
Au35Ag30	45	20	100	30	63

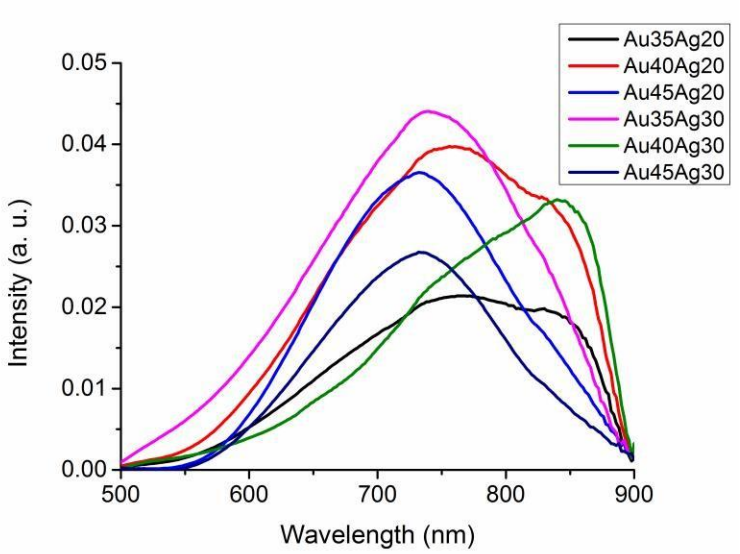

Figure 4.3 UV-Vis spectra of Multibrached Gold nanostructures obtained by varying the amount of $HAuCl_4$.

With all of these results we obtained the optimized amount of reactants to obtain the shapes that we were looking for, being the sample that was prepared by adding 40 µl of $HAuCl_4$, 30 µl of $AgNO_3$ and 20 µl of HCl. However, different samples were analized by transmission electron microscopy and the results that we choose for have the best shape were the samples that were prepared by using 40 µl of $HAuCl_4$, 20 µl of $AgNO_3$ and 20 µl of HCl as it is shown in figure 4.4.

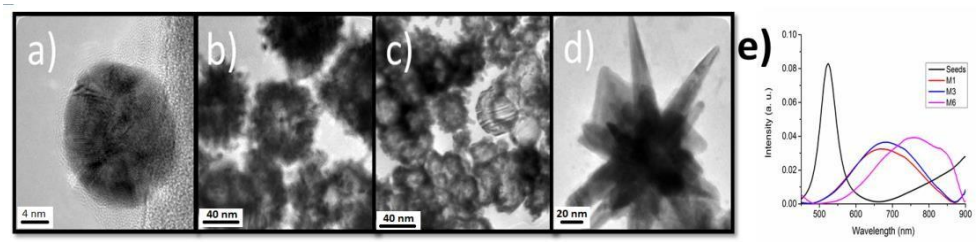

Figure 4.4 TEM images of Gold nanostructures obtained by varying the amounts of reactants. a) Gold seeds. b) Gold nanostructures obtained with 25 µl of gold salt solution, 10 µl of HCL solution and 30 µl of Ag solution (M1). c) Multibrached Gold nanostructures obtained with 25 µl of gold salt solution, 15 µl of HCL solution and 30 µl of Ag solution (M3). d) Multibrached Gold nanostructures obtained with 40 µl of gold salt solution, 20 µl of HCL solution and 20 µl of Ag solution (M6). e) UV-Vis Spectra of gold seeds and M1, M3 and M6 samples.

It was important to check the SERS activity of these nanostructures to determine which one shows greater increase in Raman signal; Rhodamine B at two concentrations ($1x10^{-3}$ M and $1x10^{-7}$ M) was tested in aqueous media. The results are shown in figure 4.5.

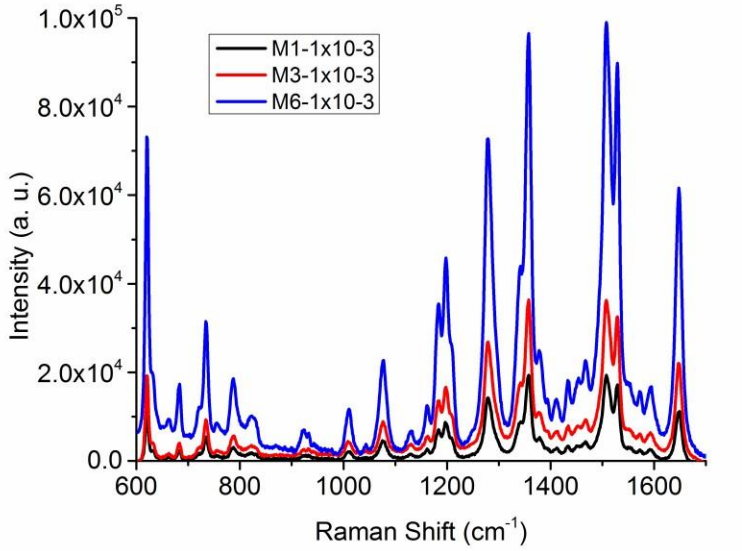

Figure 4.5 Raman spectra of $1x10^{-3}$ M Rhodamine B solution and multi-brached gold nanostructures (M1, M3 and M6).

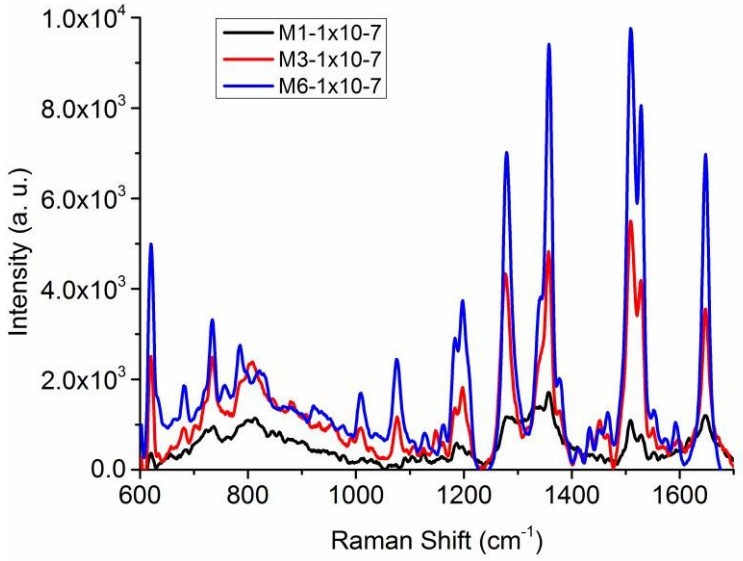

Figure 4.6 Raman spectra of $1x10^{-7}$ M Rhodamine B solution and multibrached gold nanostructures (M1, M3 and M6).

The most efficient nanostructure for SERS applications was the sample "M6". Knowing that, 200 µl of the previously prepared seed solution was added to 10 ml of 0.5 mM $HAuCl_4$ solution with

40 µl of 1M HCl at room temperature under moderate stirring. Quickly, 40 µl of 0.01M silver nitrate and 126 µl of 0.1 M ascorbic acid were added simultaneously under 700 rpm stirring, figure 4.7. The color rapidly turned from light red to greenish-black, indicating the formation of MBGNs. MBGNs-silica were prepared by adding 10 µl of 10% vol. APTES water solution to the MBGNs solution that had been previously prepared.

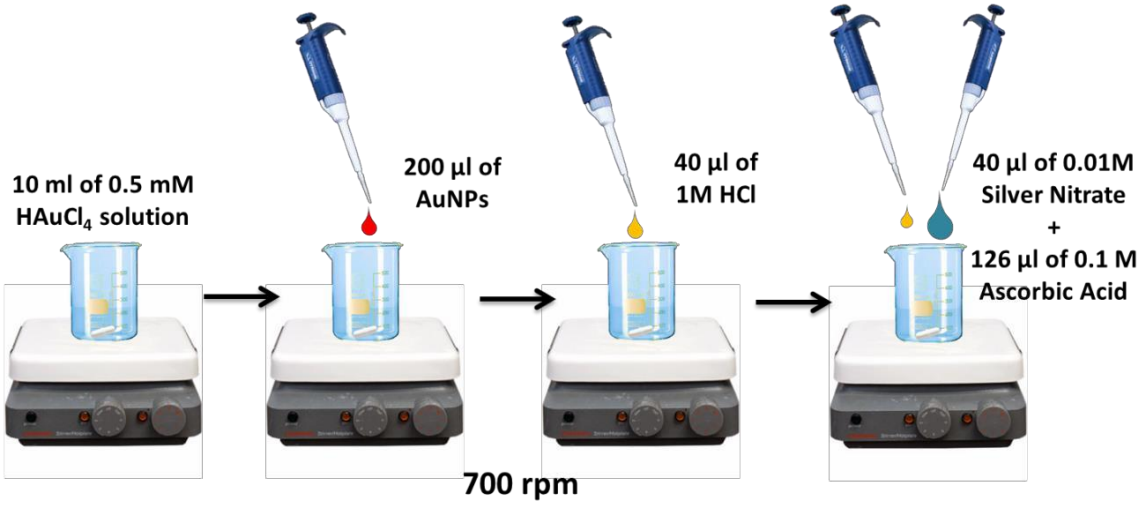

Figure 4.7 Diagram of MBGNs preparation

4.2.3 AuNPs and MBGNs linked with Rhodamine B and α-Glucose

A high concentration of RB aqueous solution (1x10-2M) was prepared to obtain the characteristic Raman spectra of concentrated RB. RB-MBGNs solutions were prepared by dissolving solid RB in distilled water and three different concentrations were obtained (1x10-7 M, 1x10-8 M and 1x10-10 M), then 500 µl of these RB solutions were mixed with 500 µl of colloidal MBGNs having RB-MBGNs final concentrations of 0.5x10-7 M, 0.5x10-8 M and 0.5x10-10 M respectively. Furthermore, RB-MBGNs-Silica was prepared as follows: first RB-APTES solution was prepared adding 10 µl of 10 %vol. APTES solution to three concentrations of RB solutions (1x10-7 M, 1x10-8 M and 1x10-10 M). Subsequently 500 µl of colloidal MBGNs-silica, were added to 500 µl of each one of the RB-APTES concentrations. And finally 500 µl of colloidal AuNPs and AuNPs-APTES were added to a 500 µl of the highest concentrated simple (1x10-7M) RB and RB-APTES solutions, to obtain RB-AuNPs and RB-AuNPs-silica respectively.

A sample of high concentration of α-glucose was prepared by dissolving 50 wt% of α-glucose in water. Additionally, α-glucose-MBGNs solutions were prepared by dissolving solid α-glucose in 100 µl of distilled water and mixing with 900 µl of colloidal MBGNs obtaining final concentrations of 5 mM, 10 mM and 20 mM (90, 180 and 360 mg/dL) respectively. The α-glucose-MBGNs-silica was prepared by dissolving solid α-glucose in 100 µl of distilled water and adding 10 µl of 10%vol. APTES solution and mixing with 900 µl of colloidal MBGNs-silica (5 mM, 10 mM and 20 mM respectively). α-glucose-AuNPs-silica was prepared adding 900 µl of colloidal AuNPs (with and without APTES) to a 100 µl of α-glucose and α-glucose-APTES solutions obtaining a 20mM concentration, respectively.

4.3 Characterization

4.3.1 Morphology and Optical Characterization

The morphology and size of the AuNPs and MGBNs-silica were analyzed by transmission electron microscopy (TEM) using a FEI Titan 800-300 with accelerating voltage set to 300 kV. UV-Vis absorption measurements were carried out using a Perkin Elmer Lamda 900 spectrometer with a spectral resolution of 2 nm. Raman spectra were collected using a Renishaw Raman System (inVia Raman Microscope) with a 20× objective lens and the excitation laser was operated at 785 nm. The integration time for each Raman measurement was 20 s. For the Raman signal detection, the laser excitation light was directly focused onto the surface of the sample solution (250 µl) with a laser power of ~5mW and the aforementioned integration time.

4.3.2 Zeta Potential

Zeta potential measurements were carried out using a Malvern Instrument Zetasizer Nano (red laser 633 nm) to the following samples, α-glucose in water (100 mM), α-glucose-APTES (100 mM), colloidal MBGNSs and colloidal MBGNs-silica. The samples were dispersed in distilled water (1 mM, pH = 7.4) with a concentration of 1 mg/ml.

4.4 Results

The size and morphological characterizations were performed by TEM images, and are shown in Figure 4.8 (a)-(d), where it was confirmed that AuNPs were obtained with an overall outer diameter of ~20 nm, see Figure 4.8(a)-(b). These AuNPs were mixed with silver nitrate at a 2:1 volume ratio and used as seeds to synthetize the MBGNs with an average size of 200 nm, as is shown in Figure 4.8(c)-(d). It is observed that the MBGNs are surrounded by a cloud of silica that promotes the agglomeration, having MBGNs- silica clusters of ~ 1000 nm, see Figure 4.8 (d).

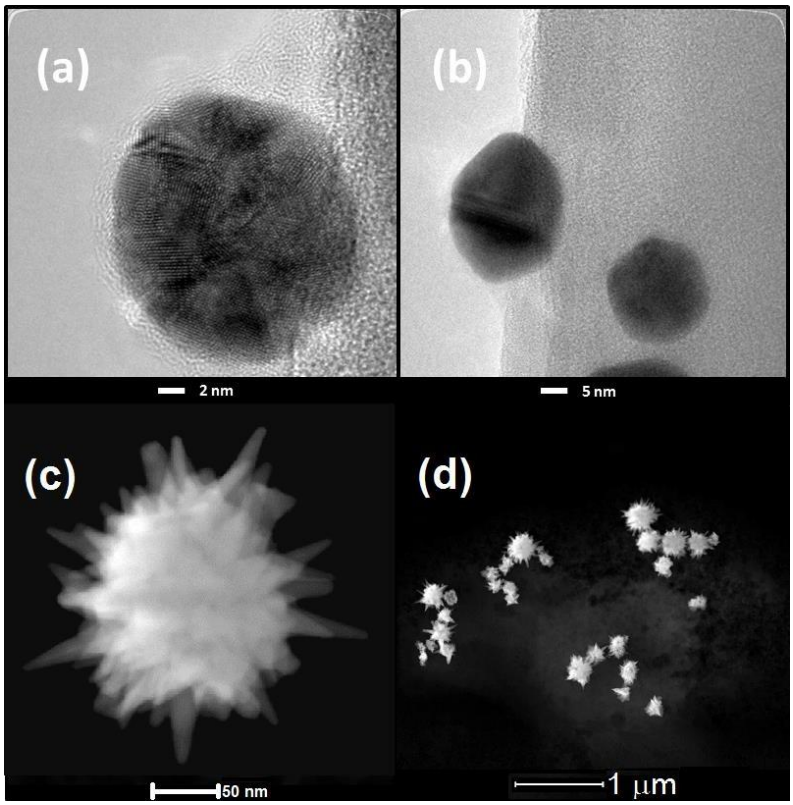

Figure 4.8 TEM images of AuNPs (a and b) with average size of ~20 nm, which were used to prepare MBGNs (c) with average diameter 200 nm. Aggregates of MBGNs-silica (d) resulting in an average size of 1000 nm.

Figure 4.9 shows the UV-Vis Spectrum of (a) AuNP, (b) MBGNs and (c) MBGNs-silica, dispersed in aqueous solution. For AuNP, the SPR is centered at 522 nm, as is shown in Figure 4.9(a) and for the MBGNs and MBGNs-silica the SPR was red-shifted to 850 nm, see Figure 4.9(b)-(c). The absorption spectrum of the MBGNs-silica sample shows a wide band, which is consistent with the agglomeration of the particles, due to the interplay between the silica coating

and the underlying MBGNs resonances, about which more will be discussed later. This is consistent with the dimensional results gleaned from the TEM images of Figure 4.8(a)-(d). These large spectral shifts from the nanospheres are manifested as color changes in the colloidal solutions of the nanoparticles, as is shown in Figure 4.4. In the image, AuNP are represented by the red solution and the MBGNs-silica solution is the greenish black solution, as seen in Figure 4.10 (a) and (b), respectively. The color changes are not significant between MBGNs and MBGNs-silica solutions.

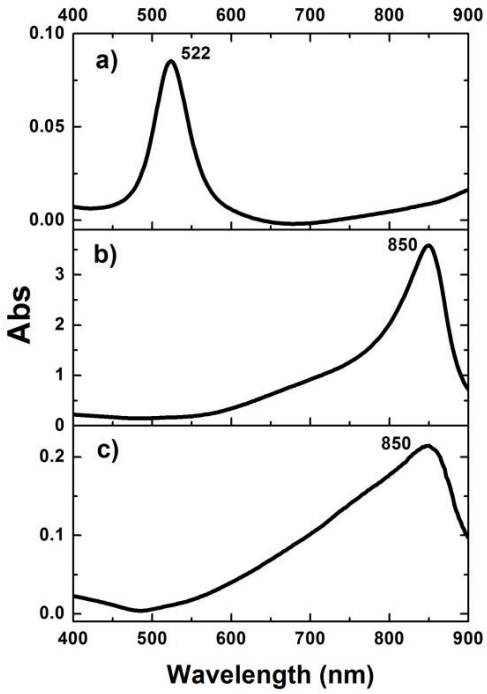

Figure 4.9 UV-Vis absorption spectra of (a) AuNPs, (b) MBGNs and (c) MBGNs-silica, dispersed in aqueous solution

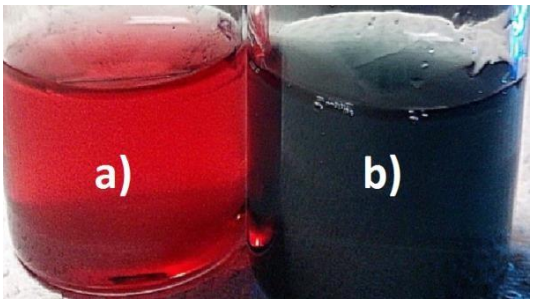

Figure 4.10 Color Comparison of the solutions. (a) AuNPs (red solution), used as a seed for the synthesis of (b) MBGNs-silica (green-black).

SERS activity of the AuNPs, MBGNs and MBGNs-Silica was examined using RB as Raman marker. The comparative SERS spectra of varying the concentration of RB, and the effect of APTES addition in AuNP and MBGNs is displayed in Figure 4.11. The Characteristic Raman signals obtained from a RB high concentrated solution (0.01 M) that yields peaks at 620, 1195, 1275, 1358, 1431, 1506, 1527, 1591 and 1647 cm^{-1} are displayed in Figure 4.11(A) and is in agreement with results reported recently [69]. The Raman signal of three concentrations of RB (10^{-10}, 10^{-8} and 10^{-7} M) adsorbed on MBGNs and MBGNs-silica are displayed in Figure 4.11(B)(b-d) and (e-g), respectively. The Raman signal of RB adsorbed on MBGNs show peaks at 628, 1284, 1364, 1516, 1534 and 1655 cm^{-1}, see Figure 4.11(B)(b-d) and RB adsorbed on MBGNs-silica at 620, 1196, 1268, 1349, 1452 and 1503 cm^{-1}, see figure 4.11(B)(e-g). It is observed that band positions present small changes with the presence of the silica coating about which more will be discussed later.

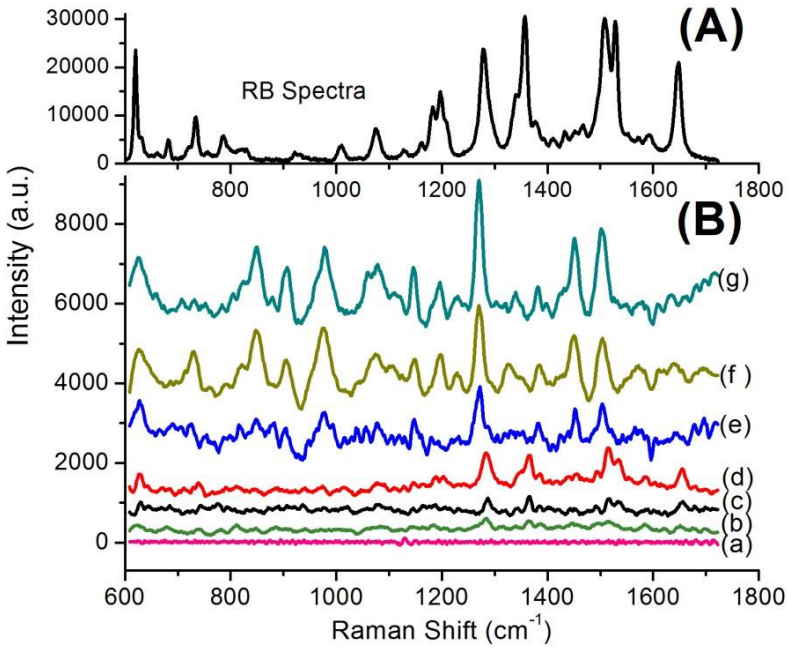

Figure 4.11(A) Raman spectra obtained from a concentrated solution (0.01 M) of Rhodamine B in distilled water. (B) Representative SERS spectra following 785 nm excitation obtained from: (a) Target MBGNs-silica, and RB at different concentration, 0.5x10-10, x10-8 and x10-7 M on MBGNs (b), (c) and (d), and (e-g) for silica coated MBGNs.

In Figure 4.12 are shown the resulting Raman spectra of using AuNPs with and without silica in RB detection and compared with the AuNP 0M spectra, where the characteristic peaks were not observed even at relative high concentration (1×10^{-7} M), however for AuNPs-silica an small peak at 850 cm^{-1} is observed. Figure 4.13 shows the increase of the Raman signal by using MBGNs and MBGNs-silica with different concentration of RB (10^{-10}, 10^{-8} and 10^{-7} M), each data point represents the average value from three SERS spectra and error bars show the standard deviations. There is a linear relationship between the intensity of the 628, 1284 and 1516 cm^{-1} bands and RB concentration. The silica coating enhanced the Raman signal by ~ 3 times in comparison when using samples without silica coating.

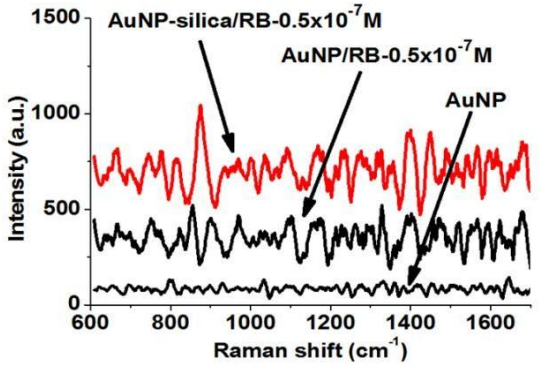

Figure 4.12 Raman signal of AuNP 0M and AuNP and AuNP-silica with RB solution at 1x10-7 M.

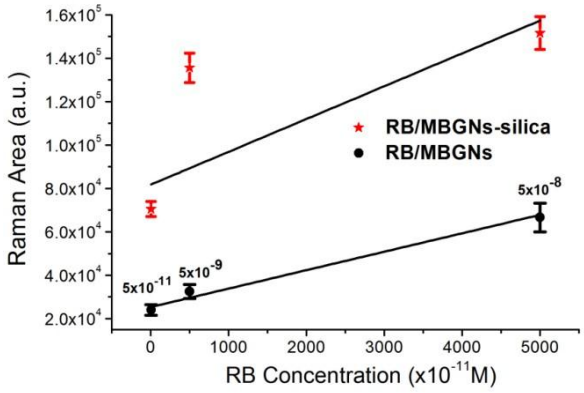

Figure 4.13 A plot of the integrated Raman signal for three peaks, (628, 1284 and 1516 cm-1) vs. the RB concentration as RB on MBGNs (RB/MBGNs) and RB-APTES solution on MBGNs-silica (RB/MBGNs-silica). Each point represents the average value from three SERS spectra and error bars show the standard deviations.

Figure 4.14 and 4.15 show SERS spectra of the α-glucose using colloidal AuNPs, AuNPs-silica, MBGNs and MBGNs-silica as the SERS substrates. In Figure 4.14(A) is presented the spectrum of a high concentration α-glucose in water (50 % wt) and several vibrational peaks were seen at 512, 845, 912, 1033, 1114 and 1365 cm^{-1}. These are the typical bands of α-glucose/water [252]. Figure 4.15 shows the Raman results of testing the detection of α-glucose (20 mM) using AuNPs and AuNPs-silica and compared with the AuNP 0M spectra, where the characteristic Raman signal is not observed, however for AuNPs-silica only an small peak at 850 cm^{-1} is observed. Figure 4.14(B) displays several SERS spectra taken at varying α-glucose concentrations (0, 5, 10 and 20 mM), showing the potential limit of detection using the MBGNs and MBGNs-silica, see Figure 4.14(B)(a-d) and (e-g) respectively, where 4.14(B)(a) corresponds to 0 mM. It is interesting the small yet consistent and reproducible blue-shift of the 512 and 1114 cm^{-1} vibrational bands observed in samples of α-glucose adsorbed in MBGNs-silica. The reason for this small shift will be discussed later. As expected, they increase in intensity with increasing the α-glucose concentration. This relationship is shown clearly in Figure 4.16, which shows a plot of the integrated signal of the 512, 1033 and 1114 cm^{-1} vibrational bands. A linear relationship between the intensity of the signal and α-glucose concentration was observed. Each data point represents the average value from three SERS spectra and error bars show the standard deviations. It is observed a ~2 times increment of the Raman signal for samples using MBGNs with silica coating compared to uncoated nanoparticles.

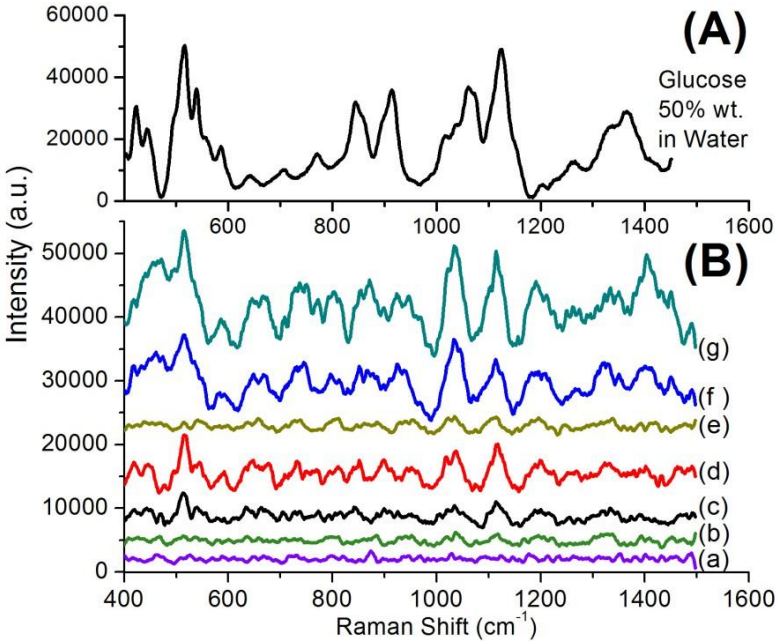

Figure 4.14 (A) Raman spectra obtained from a concentrated solution of α-glucose in distilled water (50% wt.). (B) Representative SERS spectra following 785 nm excitation obtained from: (a) Target MBGNs-silica, and α-glucose at different concentrations (5, 10 and 20 mM) on MBGNs (b-d), and (e-g) for silica coated MBGNs. In this last case, α-glucose was functionalized with APTES.

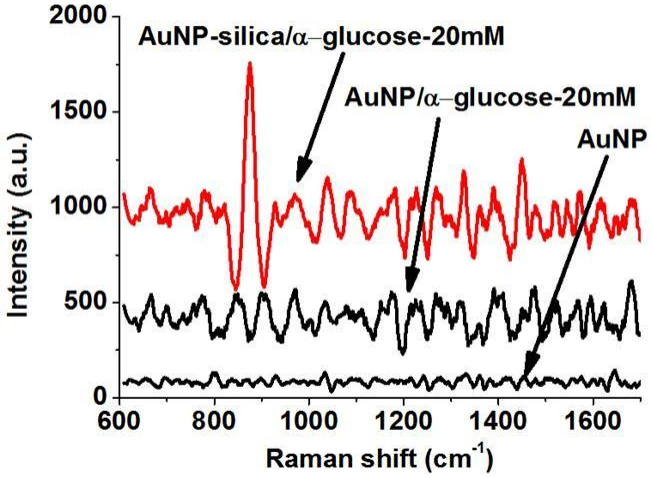

Figure 4.15 Raman signal of AuNP 0M and AuNPs and AuNP-silica with α-glucose in water at 20 mM.

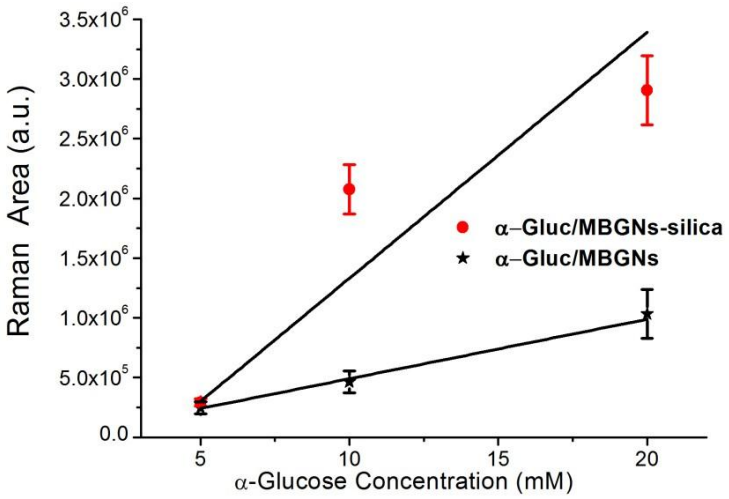

Figure 4.16 A plot of the integrated Raman signal (512, 1033 and 1114 cm-1) vs. α-glucose concentration as α-glucose on MBGNs (α-glucose/MBGNs) and α-glucose/APTES solution on MBGNs-silica (α-glucose/MBGNs-silica). Each point represents the average value from three SERS spectra and error bars show the standard deviations.

Figure 4.17 shows a schematic diagram for the preparation of α-glucose bonded to silica coated MBGNs. It is schematized the preparation of MBGNs-silica bonded to α-glucose-APTES. First AuNPs were prepared to be used as a seed to obtain the MBGNs with a positive surface charge of +34 mV, the process is explained in the experimental section. After that, APTES was added to the colloidal MBGNs binding through amines groups, obtaining MBGNs-silica (+25 mV), having the OH- groups exposed. On the other hand, α-glucose-APTES was prepared as mentioned in the experimental section. The α-glucose surface charge is -18 mV, increasing negatively for α-glucose-APTES to -46 mV, suggesting OH- in the surface. Therefore we are proposing the binding of α-glucose-APTES to the MBGNs-silica through electrostatic forces and hydroxyl groups bonds.

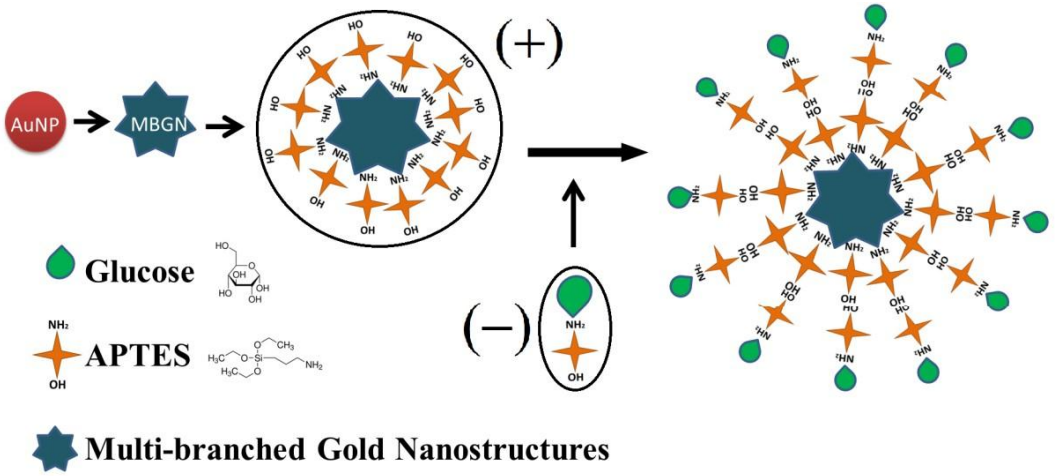

Figure 4.17 Schematic diagram showing hypothetical addition of α-glucose to MBGNs. APTES solution was added to the MBGNs, and α-glucose/APTES solution was prepared and subsequently both solutions were mixed. This facilitated the α-glucose incorporation through the bonds of hydroxyl groups and electrostatic forces.

4.5 Discussion

To interpret the Raman signal enhancement properties of MBGNs, it is necessary to analyze the structural changes and optical properties of these nanostructures. The Figure 4.2(a, b) shows the spherical gold nanoparticles (AuNPs) with an overall size of ~20 nm prepared by following the Turkevich method [253]. Such particles were used as seeds that in combination with HCl, silver nitrate, and ascorbic acid promote the anisotropic growth of Au branches on certain crystallographic facets on multi-twinned citrate gold seeds resulting on a multibranched nanoparticle (MBGNs) obtained in the absence of surfactant, see Figure 4.8(c). As has been reported the presence of Ag^{+} ions, and the Cl^{-} produced during the Au reduction of $HAuCl_4$, precipitate with the Ag^{+} ions forming AgCl on the surface of the growing AuNPs. The growth process and the morphology of the final Au product are affected inevitably, so that the AuNPs could not isotropically expand to large gold spheres but form the MBGNs [254]. Figure 4.9(d) shows the MBGNs aggregation enveloped by a gray coating of SiO_2, induced by small amount of the addition of APTES.

The SPR of AuNPs situated in 522 nm, was consistent with the particle size and the color of AuNPs solution obtained with the Turkevich method. In the case of MBGNs and MBGNs-silica the SPR is shifted to 850 nm, which is indicative of the MBGNs nature [247]. It is in accordance with the results reported in the literature where the red-shift was produced from the deviations from spherical geometry [255]. This is related with the interaction of electric field of the incoming radiation and the nanoparticle, in which it induces the formation of a dipole in the nanoparticle, and there is a restoring force that tries to compensate it, so that a unique resonance frequency matches this electron oscillation within the nanoparticle. For non-spherical particles, such as rods or branches, the resonance wavelength depends on the orientation of the electric field relative to the particle [256]. The optical properties of non-spherical particles are highly affected due to size variations of anisotropic shapes and this is because the quite differences in frequencies associated with the various resonance modes. These resonances has been modeled *via* Mie for small spheres [257] and their modification by Gans for ellipsoids [258]. As seen in Figure 4.9(b) and in Figure 4.9(c), it is observed that the silica coating expand the width in the green region of SPR peak [240, 259]. This is most likely due to the polydispersity of ~22% of MBGNs-silica agglomerates and is consistent with the results collected from the TEM images in Figure 4.8 and with the color changes in figure 4.10.

As can be seen in figure 4.11 it was difficult to obtain the characteristic Raman signal of RB adsorbed on AuNPs and AuNP-silica, suggesting that the enhancement factor is weak as has been reported for a spherical nanoparticle, but an small peak is observed at 850 cm^{-1} for AuNP-silica, corresponding to Si–OH stretching and bending as has been reported [260]. However, when MBGNs and MBGNs-silica were used, the characteristic Raman signal of RB was clearly observed, see Figure 4.11(B). Such enhancement of the Raman signal is the result of the electromagnetic field improvement probably produced by the anisotropic structures increasing the density and number of hot spots, especially at the tip of the branches as a result of the nano antenna effect [261]. The three times improvement of the Raman signal observed with the introduction of silica coating is probably due to the proximity of the MBGNs, inducing the formation of hot spots with greatly enhanced localized electromagnetic field [262, 263]. It has been reported that the carboxylic group of RB is conjugated with APTES through a condensation reaction, and yields a silanized RB which was covalently incorporated into silanol groups present on surface modified of multibrached gold nanostructures by Si-O-Si bonds [264]. The assembly of

MBGNs with silica coating as a reproducible method has been widely applied to SERS studies. Furthermore, improvement of the Raman signal by silica coating is also result of the augmentation of the bandwidth by which resonance with pumping signal is stronger. It is observed that band positions are blue-shifted with the presence of the silica coating in addition to the concomitant increases in the Raman signal. The increment of individual Raman signal peaks (628, 1284 and 1516 cm^{-1}) as a function of RB concentration follow a linear relationship with slopes of 0.5, 2 and 3 for MBGNs respectively and 1, 3 and 5 for MBGNs-silica, respectively, see Figure 4.13. This mean, MBGNs-silica coated is almost twice sensitive than uncoated nanoparticles making possible the detection of analyte concentration as lower as 10^{-10} M of RB, not detected with uncoated nanoparticles. Such result shows the relevance of the coating of MBGNs improving the interaction with analyte and increasing the hot spot.

As in the case of RB, the detection of α-glucose in water (20 mM) by using colloidal AuNPs and AuNP-silica was unsuccessful as displayed in Figure 4.12 and the 850 cm^{-1} peak is due to the presence of Si-OH stretching and bending [260]. However, α-glucose was measured with colloidal MBGNs for concentration as lower as 5 mM. As expected according to results described before on RB, the Raman signal was improved when silica coated MBGNs were used, see Figure 4.14(B). The agglomeration induced by APTES served to increase SERS signals due to the higher density of SERS hot spots [265]. As shown in figure 4.16, there is a linear relationship between the individual Raman signal peaks (512, 1033 and 1114 cm^{-1}) and α-glucose concentration. The slopes of the linear relationship for uncoated MBGNs is 6, 10 and 10 respectively, and 8, 30 and 20 respectively for silica coated MBGNs. Notice the small blue-shift due to the bonding between the hydroxyl groups of α-glucose-APTES and the free hydroxyl groups of MBGNs-silica particles [266] and through unions by electrostatic forces, as is proposed in Figure 4.17. Therefore, the functionalization proposed here is an effective way to improve interaction between MBGNs and glucose molecule, resulting on a strong enhancement of the Raman signal. These results confirm that colloidal MBGNs is an effective tool for measuring clinical concentration of α-glucose, and it is three times more sensitive when such particles are silica coated. The methodology proposed here for α-glucose measurement is simple, very reliable and cheaper because does not require special instrumentation other than Raman spectrometer.

4.6 Conclusion

In this work, we have demonstrated that MBGNs are highly SERS-active for quantitative RB and α-glucose detection in low concentrations in aqueous media. We compared the Raman enhancement when using MBGNs and MBGNs-silica and the signal is increased by ~250% and ~350%, respectively. Such enhancement is attributed to the increase of hot spot because of the morphology and the strong interaction between the analyte (RB and α-glucose) and MBGNs-silica. The functionalization process performed to both glucose molecules and MBGNs improved such interaction and make possible the measurement of concentration as lower as 5 mM (90 mg/dL). This is very important since α-glucose has been notoriously difficult to detect by SERS due to its small Raman cross-section and weak interaction with bare metal surfaces. We believe this crucial adsorption problem has been overcome due to the chemical interplay between hydroxyls on the silica surface and the α-glucose structure which facilitates the chemical adsorption. The measurement of α-glucose in water is important because mimics well the chemical environment of the human body. Future endeavors will center on the detection of glucose in body fluids like blood, urine or tears.

4.7 References

1. Choi, J.H., et al., *Localized Surface Plasmon Resonance-Based Label-Free Biosensor for Highly Sensitive Detection of Dopamine.* Journal of Nanoscience and Nanotechnology, 2014. **14**(8): p. 5658-5661.
2. Felton, C., et al., *Magnetic nanoparticles as contrast agents in biomedical imaging: recent advances in iron- and manganese-based magnetic nanoparticles.* Drug Metabolism Reviews, 2014. **46**(2): p. 142-154.
3. Srikar, R., A. Upendran, and R. Kannan, *Polymeric nanoparticles for molecular imaging.* Wiley Interdisciplinary Reviews-Nanomedicine and Nanobiotechnology, 2014. **6**(3): p. 245-267.
4. Xia, X.H. and Y.N. Xia, *Gold nanocages as multifunctional materials for nanomedicine.* Frontiers of Physics, 2014. **9**(3): p. 378-384.
5. Kneipp, K., et al., *Single molecule detection using surface-enhanced Raman scattering (SERS).* Physical Review Letters, 1997. **78**(9): p. 1667-1670.
6. Nie, S.M. and S.R. Emery, *Probing single molecules and single nanoparticles by surface-enhanced Raman scattering.* Science, 1997. **275**(5303): p. 1102-1106.
7. Vlckova, B., et al., *Single molecule SERS: Perspectives of analytical applications.* Journal of Molecular Structure, 2007. **834**: p. 42-47.
8. Li, J.-F., et al., *Extraordinary Enhancement of Raman Scattering from Pyridine on Single Crystal Au and Pt Electrodes by Shell-Isolated Au Nanoparticles.* Journal of the American Chemical Society, 2011. **133**(40): p. 15922-15925.
9. Michaels, A.M., M. Nirmal, and L.E. Brus, *Surface enhanced Raman spectroscopy of individual rhodamine 6G molecules on large Ag nanocrystals.* Journal of the American Chemical Society, 1999. **121**(43): p. 9932-9939.
10. Tian, Z.-Q., et al., *Expanding generality of surface-enhanced Raman spectroscopy with borrowing SERS activity strategy.* Chemical Communications, 2007(34): p. 3514-3534.
11. Aoki, P.H.B., et al., *Surface-enhanced Raman scattering (SERS) applied to cancer diagnosis and detection of pesticides, explosives, and drugs.* Reviews in Analytical Chemistry, 2013. **32**(1): p. 55-76.
12. Domenici, F., A.R. Bizzarri, and S. Cannistraro, *Surface-enhanced Raman scattering detection of wild-type and mutant p53 proteins at very low concentration in human serum.* Analytical Biochemistry, 2012. **421**(1): p. 9-15.
13. Grubisha, D.S., et al., *Femtomolar detection of prostate-specific antigen: An immunoassay based on surface-enhanced Raman scattering and immunogold labels.* Analytical Chemistry, 2003. **75**(21): p. 5936-5943.
14. Li, X., T. Yang, and J. Lin, *Spectral analysis of human saliva for detection of lung cancer using surface-enhanced Raman spectroscopy.* Journal of Biomedical Optics, 2012. **17**(3).
15. Mohs, A.M., et al., *Hand-held Spectroscopic Device for In Vivo and Intraoperative Tumor Detection: Contrast Enhancement, Detection Sensitivity, and Tissue Penetration.* Analytical Chemistry, 2010. **82**(21): p. 9058-9065.
16. Sha, M.Y., et al., *Surface-Enhanced Raman Scattering Tags for Rapid and Homogeneous Detection of Circulating Tumor Cells in the Presence of Human Whole Blood.* Journal of the American Chemical Society, 2008. **130**(51): p. 17214-+.
17. Beier, H.T., et al., *Application of surface-enhanced Raman spectroscopy for detection of beta amyloid using nanoshells.* Plasmonics, 2007. **2**(2): p. 55-64.
18. Choi, I., Y.S. Huh, and D. Erickson, *Ultra-sensitive, label-free probing of the conformational characteristics of amyloid beta aggregates with a SERS active nanofluidic device.* Microfluidics and Nanofluidics, 2012. **12**(1-4): p. 663-669.

19. Yao, C.K., et al., *Spatially reinforced nano-cavity array as the SERS-active substrate for detecting hepatitis virus core antigen at low concentrations.* Sensors and Actuators B-Chemical, 2012. **174**: p. 478-484.
20. An, J.-H., et al., *Surface-Enhanced Raman Scattering of Dopamine on Self-Assembled Gold Nanoparticles.* Journal of Nanoscience and Nanotechnology, 2011. **11**(5): p. 4424-4429.
21. Shi, C., et al., *Low concentration Biomolecular detection using liquid core photonic crystal fiber (LCPCF) SERS sensor - art. no. 685204*, in *Optical Fibers and Sensors for Medical Diagnostics and Treatment Applications Viii*, I. Gannot, Editor. 2008. p. 85204-85204.
22. Stiles, P.L., et al., *Surface-Enhanced Raman Spectroscopy*, in *Annual Review of Analytical Chemistry*. 2008. p. 601-626.
23. Jensen, L., C.M. Aikens, and G.C. Schatz, *Electronic structure methods for studying surface-enhanced Raman scattering.* Chemical Society Reviews, 2008. **37**(5): p. 1061-1073.
24. Atwater, A.B.a.H.A., *Low-Loss Plasmonic Metamaterials* Science, 2011. **21**: p. 290-291.
25. Kosuda, K.B., JM; Wustholz, KL; Van Duyne, RP., *Nanostructures and Surface-Enhanced Raman Spectroscopy*, in *Comprehensive Nanoscience and Technology*, S. Andrews DL, GD and Wiederrecht GP Editor. 2011 Oxford: Academic Press. p. 263-301
26. Van Duyne, R.P., J.C. Hulteen, and D.A. Treichel, *Atomic-Force Microscopy and Surface-Enhanced Raman-Spectroscopy Ag Island Films and Ag Film Over Polymer Nanosphere Surfaces Supported on Glass.* Journal of Chemical Physics, 1993. **99**(3): p. 2101-2115.
27. Perassi, E.M., et al., *Using Highly Accurate 3D Nanometrology to Model the Optical Properties of Highly Irregular Nanoparticles: A Powerful Tool for Rational Design of Plasmonic Devices.* Nano Letters, 2010. **10**(6): p. 2097-2104.
28. Sharma, Y. and A. Dhawan, *Hybrid nanoparticle-nanoline plasmonic cavities as SERS substrates with gap-controlled enhancements and resonances.* Nanotechnology, 2014. **25**(8).
29. Preciado-Flores, S., et al., *Highly reproducible synthesis of hollow gold nanospheres with near infrared surface plasmon absorption using PVP as stabilizing agent.* Journal of Materials Chemistry, 2011. **21**(7): p. 2344-2350.
30. Schwartzberg, A.M., et al., *Synthesis, characterization, and tunable optical properties of hollow gold nanospheres.* Journal of Physical Chemistry B, 2006. **110**(40): p. 19935-19944.
31. Wheeler, D.A., et al., *Optical Properties and Persistent Spectral Hole Burning of Near Infrared-Absorbing Hollow Gold Nanospheres.* Journal of Physical Chemistry C, 2010. **114**(42): p. 18126-18133.
32. Xu, S., S. Hartvickson, and J.X. Zhao, *Engineering of SiO(2)-Au-SiO(2) sandwich nanoaggregates using a building block: Single, double, and triple cores for enhancement of near infrared fluorescence.* Langmuir, 2008. **24**(14): p. 7492-7499.
33. Atkinson, R.L., et al., *Thermal Enhancement with Optically Activated Gold Nanoshells Sensitizes Breast Cancer Stem Cells to Radiation Therapy.* Science Translational Medicine, 2010. **2**(55).
34. Barbosa, S., et al., *Tuning Size and Sensing Properties in Colloidal Gold Nanostars.* Langmuir, 2010. **26**(18): p. 14943-14950.
35. Huang, X., S. Neretina, and M.A. El-Sayed, *Gold Nanorods: From Synthesis and Properties to Biological and Biomedical Applications.* Advanced Materials, 2009. **21**(48): p. 4880-4910.
36. Trigari, S., et al., *Synthesis and modelling of gold nanostars with tunable morphology and extinction spectrum.* Journal of Materials Chemistry, 2011. **21**(18): p. 6531-6540.
37. Xia, Y., et al., *Gold Nanocages: From Synthesis to Theranostic Applications.* Accounts of Chemical Research, 2011. **44**(10): p. 914-924.
38. Zhang, J.Z., *Biomedical Applications of Shape-Controlled Plasmonic Nanostructures: A Case Study of Hollow Gold Nanospheres for Photothermal Ablation Therapy of Cancer.* Journal of Physical Chemistry Letters, 2010. **1**(4): p. 686-695.
39. Jain, P.K., et al., *Calculated Absorption and Scattering Properties of Gold Nanoparticles of Different Size, Shape, and Composition: Applications in Biological Imaging and Biomedicine.* Physical Chemistry, 2006. **- 110**(- 14): p. - 7248.

40. Chen, Q., et al., *Protein modified upconversion nanoparticles for imaging-guided combined photothermal and photodynamic therapy.* Biomaterials, 2014. **35**(9): p. 2915-2923.
41. Strong, L.E., S.N. Dahotre, and J.L. West, *Hydrogel-nanoparticle composites for optically modulated cancer therapeutic delivery.* Journal of Controlled Release, 2014. **178**: p. 63-68.
42. Wang, X., et al., *alpha-NaYF4:Nd3+ Nanocrystal with Near-Infrared to Near-Infrared Luminescence for Bioimaging Applications.* Journal of Nanoscience and Nanotechnology, 2014. **14**(5): p. 3910-3913.
43. Burda, C., et al., *Chemistry and properties of nanocrystals of different shapes.* Chemical Reviews, 2005. **105**(4): p. 1025-1102.
44. Lal, S., S. Link, and N.J. Halas, *Nano-optics from sensing to waveguiding.* Nature Photonics, 2007. **1**(11): p. 641-648.
45. Sau, T.K., et al., *Properties and Applications of Colloidal Nonspherical Noble Metal Nanoparticles.* Advanced Materials, 2010. **22**(16): p. 1805-1825.
46. Vo-Dinh, T., et al., *Plasmonic Nanoparticles and Nanowires: Design, Fabrication and Application in Sensing.* Journal of Physical Chemistry C, 2010. **114**(16): p. 7480-7488.
47. Handley, D.A., *Colloidal Gold: Principles, Methods and Applications*. 1989, Academic Press: San Diego, CA.
48. Henglein, A., *Radiolytic preparation of ultrafine colloidal gold particles in aqueous solution: Optical spectrum, controlled growth, and some chemical reactions.* Langmuir, 1999. **15**(20): p. 6738-6744.
49. Turkevich, J., G. Garton, and P.C. Stevenson, *The color of colloidal gold.* Journal of Colloid Science, 1954. **- 9, Supplement 1**(- 0): p. - 35.
50. Brust, M., et al., *SYNTHESIS OF THIOL-DERIVATIZED GOLD NANOPARTICLES IN A 2-PHASE LIQUID-LIQUID SYSTEM.* Journal of the Chemical Society-Chemical Communications, 1994(7): p. 801-802.
51. Selvakannan, P.R., et al., *One-step synthesis of hydrophobized gold nanoparticles of controllable size by the reduction of aqueous chloroaurate ions by hexadecylaniline at the liquid-liquid interface.* Chemical Communications, 2002(13): p. 1334-1335.
52. Tian, Y., et al., *Silica-Coated CaF2:Eu3+ Nanoparticles Functionalized with Oxalic Acid for Bio-conjugation to BSA Proteins.* Chinese Journal of Chemistry, 2010. **28**(6): p. 921-927.
53. Wolcott, A., et al., *Silica-coated CdTe quantum dots functionalized with thiols for bioconjugation to IgG proteins.* Journal of Physical Chemistry B, 2006. **110**(11): p. 5779-5789.
54. Parakhonskiy, B.V., et al., *Size controlled hydroxyapatite and calcium carbonate particles: Synthesis and their application as templates for SERS platform.* Colloids and Surfaces B-Biointerfaces, 2014. **118**: p. 243-248.
55. Jung, G.B., et al., *Nanoplasmonic Au nanodot arrays as an SERS substrate for biomedical applications.* Applied Surface Science, 2013. **282**: p. 161-164.
56. Kong, K.V., et al., *Sensitive SERS glucose sensing in biological media using alkyne functionalized boronic acid on planar substrates.* Biosensors & Bioelectronics, 2014. **56**: p. 186-191.
57. Kong, K.V., et al., *A Transition Metal Carbonyl Probe for Use in a Highly Specific and Sensitive SERS-Based Assay for Glucose.* Journal of the American Chemical Society, 2013. **135**(48): p. 18028-18031.
58. Sun, F., et al., *Sensitive and Fast Detection of Fructose in Complex Media via Symmetry Breaking and Signal Amplification Using Surface-Enhanced Raman Spectroscopy.* Analytical Chemistry, 2014. **86**(5): p. 2387-2394.
59. Tran Thi Bich, Q., et al., *Au@SiO2 core/shell nanoparticle assemblage used for highly sensitive SERS-based determination of glucose and uric acid.* Journal of Raman Spectroscopy, 2013. **44**(12): p. 1671-1677.
60. Camden, J.P., et al., *Controlled Plasmonic Nanostructures for Surface-Enhanced Spectroscopy and Sensing.* Accounts of Chemical Research, 2008. **41**(12): p. 1653-1661.

61. Yuen, J.M., et al., *Transcutaneous Glucose Sensing by Surface-Enhanced Spatially Offset Raman Spectroscopy in a Rat Model.* Analytical Chemistry, 2010. **82**(20): p. 8382-8385.
62. Zhang, X., N.C. Shah, and R.P. Van Duyne, *Sensitive and selective chem/biosensing based on surface-enhanced Raman spectroscopy (SERS).* Vibrational Spectroscopy, 2006. **42**(1): p. 2-8.
63. Yang, X., et al., *Direct molecule-specific glucose detection by Raman spectroscopy based on photonic crystal fiber.* Analytical and Bioanalytical Chemistry, 2012. **402**(2): p. 687-691.
64. Dinish, U.S., et al., *Development of highly reproducible nanogap SERS substrates: Comparative performance analysis and its application for glucose sensing.* Biosensors & Bioelectronics, 2011. **26**(5): p. 1987-1992.
65. Al-Ogaidi, I., et al., *A gold@silica core-shell nanoparticle-based surface-enhanced Raman scattering biosensor for label-free glucose detection.* Analytica Chimica Acta, 2014. **811**: p. 76-80.
66. Yuan, H., et al., *Gold nanostars: surfactant-free synthesis, 3D modelling, and two-photon photoluminescence imaging.* Nanotechnology, 2012. **23**(7).
67. Ahmed, W., et al., *Controlling the morphology of multi-branched gold nanoparticles.* Nanotechnology, 2010. **21**(12).
68. Kawamura, G., et al., *Shape control synthesis of multi-branched gold nanoparticles.* Materials Chemistry and Physics, 2009. **115**(1): p. 229-234.
69. Liu, M.Z. and P. Guyot-Sionnest, *Mechanism of silver(I)-assisted growth of gold nanorods and bipyramids.* Journal of Physical Chemistry B, 2005. **109**(47): p. 22192-22200.
70. Orendorff, C.J. and C.J. Murphy, *Quantitation of metal content in the silver-assisted growth of gold nanorods.* Journal of Physical Chemistry B, 2006. **110**(9): p. 3990-3994.
71. N. C. Shah, J.M.Y., O. Lyandres, M. R. Glucksberg, J. T. Walsh and R.P. Van Duyne, *Surface-Enhanced Raman Spectroscopy for Glucose Sensing*, in *In Vivo Glucose Sensing*, J.A. Stenken, Cunningham, D. E., Eds., Editor. 2010, John Wiley & Sons, Inc. p. 421-443
72. Kimling, J., et al., *Turkevich Method for Gold Nanoparticle Synthesis Revisited.* 2006. **- 110**(- 32): p. - 15707.
73. Yuan, H., et al., *Shape and SPR evolution of thorny gold nanoparticles promoted by silver ions.* Chemistry of Materials, 2007. **19**(7): p. 1592-1600.
74. Liz-Marzan, L.M., *Tailoring surface plasmons through the morphology and assembly of metal nanoparticles.* Langmuir, 2006. **22**(1): p. 32-41.
75. Perez-Juste, J., et al., *Gold nanorods: Synthesis, characterization and applications.* Coordination Chemistry Reviews, 2005. **249**(17-18): p. 1870-1901.
76. Mie, G., *Articles on the Optical Characteristics of Turbid Tubes, Especially Colloidal Metal Solutions.* ANNALEN DER PHYSIK, 1908. **25** (3): p. 377-445.
77. Gans, R., *The Shape of Ultra Microscopic Gold Particles.* ANNALEN DER PHYSIK, 1912. **37**(5): p. 881-900.
78. Kobayashi, Y., M.A. Correa-Duarte, and L.M. Liz-Marzan, *Sol-gel processing of silica-coated gold nanoparticles.* Langmuir, 2001. **17**(20): p. 6375-6379.
79. Hunt, J.D., et al., *Polymerization of aqueous silica in H(2)o-K2O solutions at 25-200 degrees C and 1 bar to 20 kbar.* Chemical Geology, 2011. **283**(3-4): p. 161-170.
80. Kumar, P.S., et al., *High-yield synthesis and optical response of gold nanostars.* Nanotechnology, 2008. **19**(1): p. 6.
81. Jiang, J., et al., *Single molecule Raman spectroscopy at the junctions of large Ag nanocrystals.* Journal of Physical Chemistry B, 2003. **107**(37): p. 9964-9972.
82. Kelly, K.L., et al., *The optical properties of metal nanoparticles: The influence of size, shape, and dielectric environment.* Journal of Physical Chemistry B, 2003. **107**(3): p. 668-677.
83. Gao, X.Q., et al., *Synthesis and characterization of functionalized rhodamine B-doped silica nanoparticles.* Optical Materials, 2009. **31**(11): p. 1715-1719.
84. Wheeler, D.A., et al., *Magnetic Fe3O4-Au core-shell nanostructures for surface enhanced Raman scattering.* Annalen Der Physik, 2012. **524**(11): p. 670-679.

85. López-Luke, T., et al., *Synthesis, characterization and surface enhanced Raman scattering of hollow gold–silica double shell nanostructures.* Biomedical Spectroscopy and Imaging 2012. **01**: p. 275-291.

CHAPTER 5

GENERAL CONCLUSION

General Conclusion

In this work the synthesis of metallic and ceramic nanoparticles was achieved by controlling different variables that are implied during the reaction processes. For the case of gold nanoparticles, the Turkevich method was the most adequate process for obtain well dispersed gold nanospheres presenting an average size of ~15±3 nm, that have an SPR centered in 520 nm, this nanoparticles were prepared by using reactant ratios of 1:35 mol of $HAuCl_4$:Sodium Citrate, which result in the best concentration for our application, being stables at long term storage under no-light exposure. The process is very suitable for highly reproducible results, the reaction media is water and no-surfactant was used which favor the biocompatibility. However, for having SERS phenomena we know that it was necessary to change nanoparticle shapes, this is because when differences in size and shape the electromagnetic field is enhanced by the generation of hot-spots.

Reviewing different works we found that by adding different quantities of gold chloride hydrate, hydrochloric acid, silver nitrate and ascorbic acid to gold nanospheres, the anisotropic growth was promoted obtaining different size and shape nanostructures, which were helpful for SERS processes. Different quantities of reactants were proven, until optimized the best ones, which resulting in a well-defined nanostructure by using 2:1 molar ratios of $HAuCl_4$:$Ag(NO_3)_3$, that present an SPR of around ~850 nm, which is in the near infrared region. However when these gold nanostructures were synthetized, they were not stable enough, and one of our principal goals was to obtain well stable nanostructures with non-surfactant synthesis, this issue was solved by adding a silica capping, using APTES, hydrochloric acid and sodium silicate as reactants, in which the amounts of reactants were optimized, and a well-defined silica shell was incorporated.

Having obtained well dispersed and stable, highly reproducible gold nanospheres and multibranched gold nanostructures, they were used for evaluate its properties in Raman spectroscopy, as it has being reported, gold nanostructures served as raman signal enhancers, however the necessity of having different ways that gives faster results by detecting different analytes of interest, especially ones that could represent great importance for biomedical applications, such as proteins or glucose levels. For having a representative results this single and silica-coated gold nanostructures were analyzed by mixing them with Rhodamine B, a well-known molecule, but this was doing in liquid media, having result that our detection limits were until $0.5x10^{-10}$ M, enhancing the signal by around ~250 % and ~350 % respectively, this was due to the

interactions between Rhodamine B and amino groups present in APTES, which was important because for detections at low concentration in most of the cases an specific substrate has to be prepared, increasing time and costs of this technique. We prove these same gold nanostructures with α-glucose, and the detection limits that this method is as low as 5 mM or in other words 90 mg dL^{-1}, which is an important result because if we review the limits of glucose in blood are between 75 and 110 mg dL^{-1}, besides glucose in water is very difficult to determine by SERS due to its small Raman cross-section and weak interaction with metal surfaces.

On the other hand, having functionalized nanoparticles gives us the opportunity of labeling cells such as HeLa cells, gold and zirconium oxide nanoparticles were functionalized to observe their interaction with biological samples. For the case of gold nanoparticles it was necessary to add special functional groups such as molecules with thiol groups, then with and amino-Polyethileneglycol and finally with folic acid to promote the internalization to the HeLa cells, at the end we observe that there was a better internalization with those nanospheres that were not funtionalized, should be noted that this was a part of a short stay at Charlotte University in North Carolina, and the time was not enough to make more probes. In the case of ZrO_2:Yb^{3+}-Er^{3+} nanoparticles were functionalized by using biotin Biotin-Anti-rabbit (mouse IgG) and rabbit antibody-AntiKi-67 biomolecules and confirming the conjugation by FTIR, zeta potential and DLS. These nanoparticles present strong red luminescence by being excited at 970 nm in a two-photon confocal microscope and this was due to the up-conversion effect, confirmed by the photoluminescence spectra which indicates that UPC red emission of Er^{3+} ions is affected by the molecules located on the nanoparticles surface. As we observed there is an increment of red emission when AntiKi-67 was present in the nanoparticles this is probably caused by an important reduction of impurities compared to the rest of the samples. Our results indicate that the method of conjugation depicted in this work can be a promising alternative to afford stable colloidal dispersions of nanoparticles in water and efficiently label cancer cells.

As we seen previously, gold nanoparticles were well candidates as marker in biological samples, the importance of evaluate malignant diseases in human tissues in crucial for early treatments, the opportunity of have materials that give the possibility of apply several techniques of detection is an advantage. Nowadays new equipment in which different analysis procedures are implied such as confocal microscopy and raman spectroscopy are developed, the use of gold

nanoparticles for stain cervical tissue, gave us the opportunity of evaluate two different damages in cervical tissue, one with the presence of Human Papilloma Virus and one with malignant carcinoma. The properties of gold nanoparticles like high cross-section and contrast, two photon luminescence and biocompatibility were presented by analyzing these tissues by confocal and multi-photonic microscopy, 543 nm and 900 nm respectively, which is important because at the NIR region the tissue auto-fluorescence is avoided, there was no damage only until certain wavelengths and power, and as we checked solely in the tissues that were gold stained. Furthermore we could observed that the cell structures in presence of gold nanoparticles were well defined which in important because the cell damage is firstly analyzed by evaluating sizes of nucleus and cytoplasm, and as we observed by SEM images gold nanoparticles were situated primarily on the nucleus. Finally the presence of gold nanoparticles in the tissue enhance the Raman signal of certain functional groups; we could observe the differences between the two tissue spectra, basically in the peaks that are related with the DNA, having principal chances between a non-damaged and damaged tissues.

With this work we could have the opportunity of offer new analysis techniques, as in the case of Raman spectroscopy in liquid media by using gold nanostructures that helps to enhance the signal, besides other materials as biological markers.

Future work

The possibility of continuing with these gold nanostructures for detects low concentration of different analytes, such as cancer proteins. Use metallic and ceramic nanoparticles, possibly combined with chromophores for enhance the luminescence response for imaging in biological samples. Analyze and validate the Raman enhancement of nucleus cells with gold nanoparticles.

Publications

- **Andrea Ceja-Fdez**, Tzarara López-Luke*, Alejandro Torres-Castro, Damon. A. Wheeler, Jin Z. Zhang and Elder De la Rosa*. **Glucose Detection Using SERS with Multi-branched Gold Nanostructures in Aqueous Medium.** RSC Advances (2014) 4, 59233. DOI: 10.1039/c4ra11055b.
- **Andrea Ceja-Fdez,** Tzarara López-Luke*, Jorge Oliva, Juan Vivero-Escoto, Ana Lilia Gonzalez-Yebra, Ruben A. Rodriguez Rojas, Andrea Martínez-Pérez, and Elder De la Rosa*. **Labeling of HeLa cells using ZrO_2:Yb^{3+}-Er^{3+} nanoparticles with upconversion emission.** Journal of Biomedical Optics (2015) 20(4), 046006. DOI:10.1117/1.JBO.20.4.046006.
- Isaac Zarazúa, Diego Esparza, Tzarara López-Luke, **Andrea Ceja-Fdez**, J. Reyes-Gomez, Ivan Mora-Seró, Elder De la Rosa. **Effect of the electrophoretic deposition of Au NPs in the performance CdS QDs sensitized solar Cells.** Electrochimica Acta (2016) 188, 710–717. DOI: 10.1016/j.electacta.2015.11.127.
- Elisa Cepeda-Pérez, Tzarara López-Luke, Germán Plascencia-Villa, Leonardo Perez-Mayen, **Andrea Ceja-Fdez**, Arturo Ponce, Juan Vivero-Escoto, Elder De la Rosa. **SERS and integrative imaging upon internalization of quantum dots into human oral epithelial cells.** J. Biophotonics (2016) 1–11. DOI 10.1002/jbio.201600034.
- **Andrea Ceja-Fdez**, Tzarara López-Luke*, Ramon Carriles, Juan Vivero-Escoto, Ana Lilia Gonzalez-Yebra and Elder De la Rosa*. **Two-Photon Luminescence Imaging of Cervical Tissue stained with Gold Nanospheres. (In Process)**